Atomic scale light-matter interaction: From ultrafast physics to photoexcitation phenomena

DISSERTATION ZUR ERLANGUNG DES DOKTORGRADES
DER NATURWISSENSCHAFTEN (DR. RER. NAT.)
DER FAKULTÄT FÜR PHYSIK

DER UNIVERSITÄT REGENSBURG

vorgelegt von
Thomas Buchner
aus Landshut

Im Jahr 2023

Das Promotionsgesuch wurde am 17. Januar 2023 eingereicht.
Die Arbeit wurde angeleitet von Prof. Dr. Jascha Repp.

Prüfungsausschuss:
Vorsitzender: PD Dr. Jan Vogelsang
1. Gutachter: Prof. Dr. Jascha Repp
2. Gutachter: Prof. Dr. Andrea Donarini
Weiterer Prüfer: Prof. Dr. Rupert Huber

Contents

1 Introduction

The interaction of light with matter is at the heart of numerous processes in nature and is the central effect governing phenomena such as photosynthesis [1], photochemical reactions [2] or photovoltaic devices [3]. The recent development of ultrafast laser sources has opened the door for light-matter interactions to also play an instrumental role in fields such as lightwave electronics [4] or quantum information processing [5], which is why an understanding of these interactions at the fundamental level is of utmost importance for the development of novel technologies.

The advent of scanning tunneling microscopy (STM) [6] and atomic force microscopy (AFM) [7] has paved the way for the study of material surfaces down to the atomic scale. These probe-based techniques have seen a rapid progress in the last four decades with more and more intricate measurement techniques being established.

AFM has been utilized to probe a series of astonishing phenomena with unprecedented precision, such as the direct imaging of the Si(111)-(7 $\times$ 7) reconstruction [8] or resolving the chemical bonds inside a single molecule [9]. While AFM allows access to the geometry of a surface down to the atomic scale, STM is used to probe the electronic states of a conductive substrate. Since the first atomic scale images in 1982 [10], STM has been employed for a variety of tasks like the positioning of individual atoms [11], the mapping of the frontier orbitals of a single molecule [12] or the controlled movement of a molecular motor [13].

The atomic scale precision of STM and AFM provides a way to study the interaction of light with single molecules or atoms. The potential of the combination of a laser source with an STM was already identified in 1991, when first endeavors were undertaken to equip an STM with the time resolution provided by ultrafast laser pulses [14]. This prospect sparked the development of numerous laser-assisted STM and AFM techniques, such as tip-enhanced Raman spectroscopy [15], ultrafast lightwave-driven STM [16], near-field scanning optical microscopy [17] or direct photoexcitation techniques [18]. These cutting-edge technologies enabled observing the effects of interactions between light and molecule down to sub-Ångström resolution, such as resolving intra-molecular vibrations [19], tracking the ultrafast motion of a single molecule [20] or inducing bond-selected photodissociation [21].

This thesis shall contribute to this field by exploring light-matter interaction down to the atomic scales for novel systems and with newly developed measurement techniques. Each project outlined in this thesis explores a different aspect of atomic scale light matter interaction.

In chapter 5 STM experiments on individual molecules situated on an ultrathin NaCl layer grown on a metal substrate with combined sub-picosecond temporal and sub-Ångström spatial resolution are discussed. Using THz laser pulses we were able to switch the molecules between two stable geometries via single electron injection. Furthermore, we demonstrate that the probability to toggle the molecule can be influenced by exerting an ultrafast force to select atoms within the molecule, which is mediated by the electric field of a THz pulse.

In chapter 6 a novel approach for the study of photoexcitation phenomena at the atomic scale is presented. By combining a pulsed optical laser with an AFM and synchronizing the excitation of the junction with the cantilever oscillation we were able to attain an in-depth look into the effects of photoexcitation of a single molecule situated on a thin NaCl film deposited onto a metal substrate. The direct excitation of the molecule by the laser causes it to toggle between two stable adsorption geometries, which is attributed to an intermediate charging of the molecule. Exciting the molecule when the AFM tip is in close proximity to the molecule drastically increases the switching rate between its stable configurations, which is attributed to an exchange of photoexcited charge carriers with the tip. Furthermore, spatially resolved maps of the switching rate indicate an involvement of a transiently charged state in the observed photoinduced toggling motion.

In chapter 7 we investigate the effects of photoexcitation on a molecule deposited onto a bulk-like insulating NaCl film grown on a metal substrate. Due to the decoupling from the metallic substrate, the charged states of the individual molecules are stabilized in this environment. We utilize the laser pulses to excite the molecule and remove or add electrons from or to the excited state orbitals, which leaves the molecule in a stable charged state. This can be detected by the AFM due to the change in electrostatic interaction. We mapped these photocurrents across the molecule in an attempt to directly image the excited state orbitals. Additionally, we employed a voltage pulse scheme to controllably charge and discharge the molecule within a single cantilever oscillation.

In chapter 8 the construction of a novel lightwave-driven scanning tunneling microscope is described. The novel design is tailored to fit to the specific needs for the coupling of mid-infrared radiation to the STM. Here, the design and the assembly of the scan unit and the most important supporting ultra-high vacuum equipment is outlined. An Au(111) sample was prepared and analyzed using this novel equipment, where we were able to obtain images of a clean surface with atomic resolution, establishing the proper functionality of this newly designed apparatus.

2 Scanning Tunneling Microscopy

In this chapter, the basic concepts of scanning tunneling microscopy (STM) relevant for the experiments shown later in this thesis will be discussed. These include the theoretical background of the technique and recent research on more specific topics, namely imaging of molecular orbitals, laser-assisted and lightwave-driven STM.

2.1 Theoretical Background

With its inception in 1982 by Binnig *et al.*, where they demonstrated tunneling current through a controllable vacuum gap by bringing a sharp tip close to a conductive sample [6], a powerful tool to study surfaces down to the atomic scale was established. Soon afterwards, they also showed the imaging capabilities of STM, where they were able to resolve a conductive surface with atomic resolution [10]. The basic concept of STM will be outlined in the following.

The quantum mechanical tunneling of an electron through a vacuum barrier is shown in figure 2.1a. In this one-dimensional picture, the tip as well was the sample are considered as two metal electrodes separated by a vacuum barrier with height Φ, and a width of d. Here, the work functions for tip and sample are assumed to be equal for reasons of simplicity. Applying a bias voltage between tip and sample shifts the Fermi energies of the electrodes with respect to each other. This way, unoccupied states in the sample or tip become available into which electrons from the occupied states of the other electrode can tunnel to. For the following derivation, the potential barrier height Φ is assumed to be constant for $0 < z < d$, which is a good approximation for small bias voltages. In the quantum mechanical picture, the electron is described by a wave function $\psi(x,t)$, and the probability density is given by $|\psi(x,t)|^2$ [23].

The following derivation follows ref. [23]. The transmission probability of the electron through the barrier can be computed by solving the stationary, one-dimensional Schrödinger equation separately for tip, sample and barrier. It is given by

$$\left(-\frac{\hbar^2}{2m}\frac{\partial^2}{\partial x^2} + V(x)\right)\psi(x,t) = E\psi(x,t) \quad \text{with} \quad V(x) = \begin{cases} 0 & \text{for} \;\; z < 0,\; d < z \\ \Phi & \text{for} \;\; 0 < z < d \end{cases} \tag{2.1}$$

Outside of the vacuum gap the electron can freely propagate and can be solved with

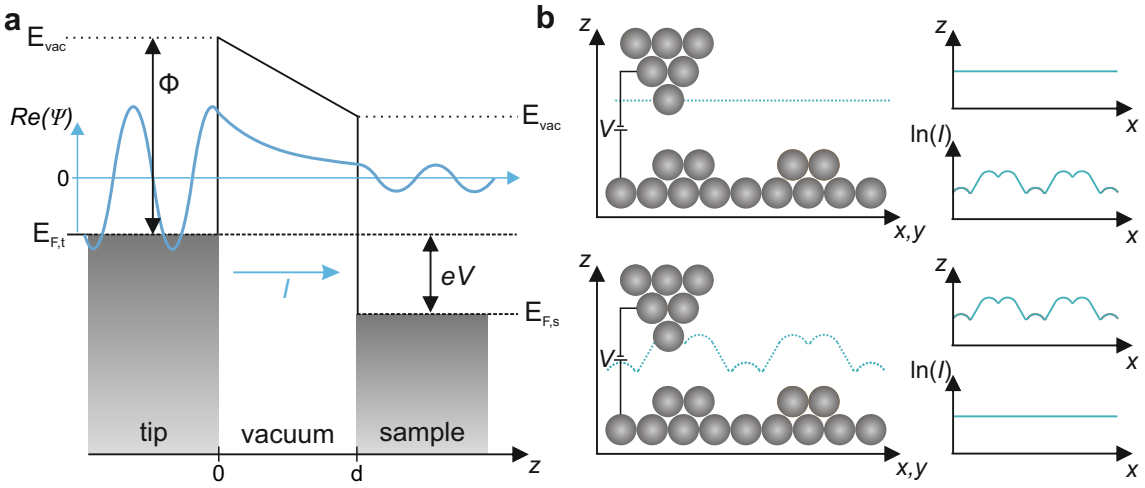

Figure 2.1: Tunneling barrier and STM operating modes. **a** Scheme of a quantum mechanical tunneling barrier. By applying a bias voltage V between tip and sample, electrons can tunnel from occupied states in the tip to unoccupied states in the sample (and vice versa). **b**, Operating modes of an STM. In constant height mode (top) the tip is kept at a defined z-position and the measured current gives information about the surface. In constant current mode (bottom) a feedback loop keeps the current at a defined value by adjusting the tip position. The real part of a wave function with $E < \Phi$ propagating in $+z$-direction is indicated. After [22].

the following plane wave ansatz:

$$\psi(z) = Ae^{ikz} + Be^{-ikz} \quad \text{for} \quad z < 0 \tag{2.2}$$

$$\psi(z) = Fe^{ikz} + Ge^{-ikz} \quad \text{for} \quad d < z \tag{2.3}$$

Here, the wave number is given by $k = \sqrt{2mE}/\hbar$. Inside the potential barrier the Schrödinger equation is solved by

$$\psi(z) = Ce^{-\kappa z} + De^{\kappa z} \quad \text{for} \quad 0 < z < d \tag{2.4}$$

where $\kappa = \sqrt{2m(\Phi - E)}/\hbar$. The remaining constants can be determined using the boundary conditions at the metal/vacuum interfaces. The transmission probability is then given by $|T(E)|^2 = |F|^2/|A|^2$, which can be approximated by

$$|T(E)|^2 \cong \exp\left(-\frac{2\sqrt{2m(\Phi - E)}}{\hbar}d\right) = \exp\left(-2\kappa d\right) \tag{2.5}$$

This derivation shows that the tunneling current depends exponentially on the barrier width d, i.e. the distance between tip and sample. Furthermore, the decay constant can be approximated as $\kappa \approx \sqrt{2m\Phi}/\hbar$ for $E \ll \Phi$. Since the work functions of metals are typically around $\Phi \approx 5\,\text{eV}$, the decay constant can be further approximated to

$\kappa \approx 11.4\,\mathrm{nm}^{-1}$, which implies that the tunneling current is reduced by approximately one order of magnitude when the tip is moved 1 Å further away from the sample [22]. This strong exponential dependence of the tunneling probability, and hence the resulting tunneling current, is the quintessential feature enabling imaging atomic scale structures with the STM.

The two different, most commonly used STM operating modes are shown in figure 2.1b, namely constant height (top in fig. 2.1b) and constant current mode (bottom in fig. 2.1b). Here, an atomically sharp tip is brought into close proximity of the conductive surface, so that electrons can tunnel between tip and sample as described above. By raster-scanning the tip across the sample, the surface can be probed. In constant height mode, the tip is kept at a fixed height while the tunneling current is recorded. While this does not require any feedback mechanism which might interfere with the measurement, the tip can hit protrusions during scanning what will eventually damage the sample and the tip. Constant current mode avoids this issue by implementing a feedback, which retracts or approaches the tip to keep the tunneling current at a constant, preset value. This way the tip follows the corrugation of the sample and tip crashes can be avoided when scanning large areas.

While the derivation above yields an instructive approach to the underlying tunneling processes in STM, more refined methods have already been developed. Specifically, the description of tunneling between two electrodes, as proposed by Bardeen [24] and transferred to STM by Tersoff and Hamann for the case of a tip s-wave, have found widespread application [25, 26]. From this assumption it was derived that the tunneling current in an STM is proportional to the local density of states (LDOS), and thus the topographic images obtained with STM describe a contour of the LDOS of the sample. For the assumptions of a spherically symmetric tip, small temperature and a constant tip density of states from E_F to $E_\mathrm{F} + eV$, the tunneling current can be expressed as [22]

$$I \propto \int_0^{eV} \rho_\mathrm{S}(E_\mathrm{F} + \epsilon, \vec{r_0}) d\epsilon, \tag{2.6}$$

where ρ_S is the LDOS of the sample and $\vec{r_0}$ is the position of the tip.

From equation 2.6 the following relation can be derived [22]:

$$\frac{dI}{dV}(V) \propto \rho_\mathrm{S}(E_\mathrm{F} + eV, \vec{r_0}). \tag{2.7}$$

This implies, that the differential conductance is proportional to the LDOS of the sample, which can be obtained experimentally by either calculating a numerical derivative of an $I(V)$ curve or via lock-in detection. This technique is called scanning tunneling spectroscopy (STS).

Another approximation for the wave function inside the tunneling barrier is the Wentzel–Kramers–Brillouin (WKB) approximation, which is used in a simulation to support the experimental data shown in chapter 7. The semiclassical approach to the solution of the Schrödinger equation arrives at the following wave function [27]:

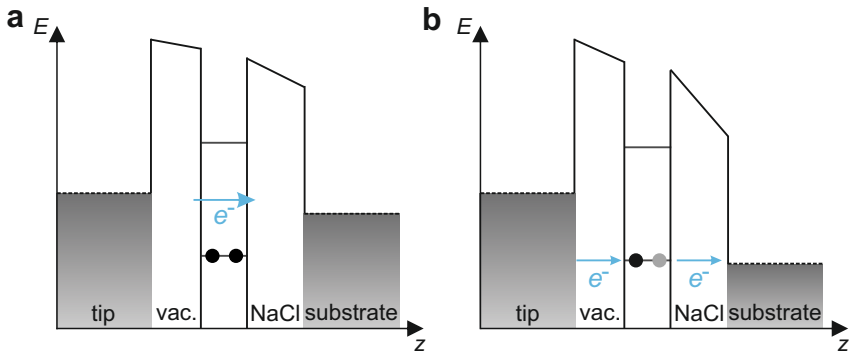

Figure 2.2: Double barrier tunneling junction for a molecule situated on a thin NaCl layer. a, Double barrier junction with a small applied bias voltage. In this situation electrons tunnel directly between the two metal electrodes. **b**, Double barrier junction at resonant bias voltage. If the bias voltage is tuned to be in resonance with one of the molecular orbitals, sequential tunneling through a molecular orbital can occur.

$$\psi(z) \approx \frac{A \exp\left(\frac{\sqrt{2m(\Phi-E)}}{\hbar} z\right) + B \exp\left(-\frac{\sqrt{2m(\Phi-E)}}{\hbar} z\right)}{\hbar^{-1/2} \sqrt[4]{2m(\Phi - E)}}, \tag{2.8}$$

where the prefactors A and B can again be determined via the boundary conditions of the problem.

2.2 Double Barrier Tunneling Junction

As was shown in the previous section, the STM is capable of probing the local density of states of a conductive sample. This was extended to the electronic structure of molecules in 2005 by Repp *et al.* [12], which they achieved by implementing a thin insulating layer of sodium chloride (NaCl) between the conductive metal substrate and the molecule. This prevented the hybridization of the molecular frontier orbitals with the states of the metallic substrate and allowed imaging of the unperturbed molecular orbitals. However, these molecular states exhibit an energy broadening due to the coupling to phonon modes of the underlying NaCl layer [28].

This situation leads to the energetic landscape shown in figure 2.2. For small bias voltages (see fig. 2.2a), electrons tunnel directly between the two metal electrodes, since there are no additional states available in the tunneling gap, resulting in a small tunneling current, which is referred to as in-gap current. Increasing the bias voltage such that the Fermi energy of one of the electrodes energetically aligns with one of the molecular orbitals allows sequential tunneling to occur. In the situation shown in figure 2.2b, a large negative bias voltage is applied. Here, the highest occupied molecular orbital (HOMO) is depopulated by tunneling an electron to the substrate

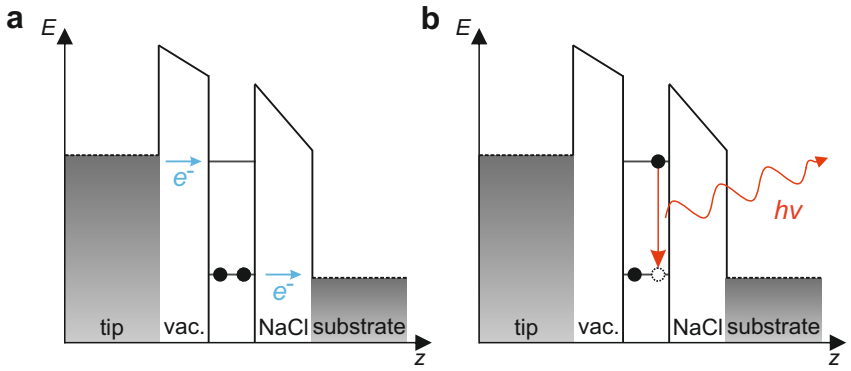

Figure 2.3: Mechanism for STM-induced luminescence. **a**, Sequential tunneling process for STM luminescence. The HOMO is depopulated while the LUMO is filled, leaving the molecule in an excited state. **b**, Radiative decay of the excited molecular state by emission of a photon.

and sequentially refilled by an electron from the tip. This resonant tunneling leads to an increase in the observed current due to the intermediate state located in the gap.

A similar process occurs for large positive bias voltages. There, sequential tunneling takes place through the lowest unoccupied molecular orbital (LUMO), which again leads to an increase of the tunneling current.

2.3 STM-Induced Luminescence

As was demonstrated in the previous section, STM constitutes a method to examine conductive samples with atomic scale precision. In 1988 Gimzewski *et al.* observed, that photons can be generated via inelastic electron tunneling, where the excess energy of a tunneling electron is emitted in the form of electromagnetic radiation [29]. It was also found shortly after, that the emission of photons from an STM tunneling junction can be significantly enhanced by plasmonic effects [30]. By positioning a single molecule on a thin dielectric layer grown on top of the supporting metal, which is necessary to decouple the molecule from the metallic substrate [31], Qiu *et al.* were able to show luminescence spectra with sub-molecular resolution [32].

This development comprises a first step towards the study of light-matter interaction and the investigation of excited states in STM, which has seen increasing attention in recent years [33]. While this technique is applicable for the examination of systems like layered organic semiconductors [34–36] or transition metal dichalcogenides (TMDCs) [37], we will focus on the efforts made to study single molecules [38–54].

A mechanism for STM-induced luminescence is shown in figure 2.3. Here, a sequential tunneling process creates an excited state in the molecule. As shown in figure 2.3a, the HOMO of the molecule is emptied and the LUMO is filled. This results

in an excited state of the molecule, where both LUMO and HOMO are occupied by one electron. The excited state then decays by emitting a photon from the junction (figure 2.3b), which is collected and analyzed.

While this excitation mechanism has been established to result in luminescence [53, 55], the interaction of the molecule in the junction with a nanocavity plasmon [39, 42, 43, 50, 56] also plays a relevant role in the excitation of the molecule. STM-induced luminescence can be employed to study a myriad of processes, for example resonant energy transfer between molecules [49], intermolecular dipole-dipole coupling [53] or plasmon-induced molecular motion [42]. In chapters 6 and 7 the effects of direct photoexcitation of single molecules will be explored, which rely on the adsorption of photons rather than the emission, and thus constitute a complementary approach to the study of molecular excited states.

2.4 Laser-Assisted Scanning Tunneling Microscopy

Another approach to studying light-matter interactions at the atomic scale was taken in 1991, when Völker *et al.* coupled lasers to the STM tunneling junction [14], a concept which has been built upon ever since [57–59]. This combination does not only allow performing time-resolved measurements (see e.g. refs. [16, 20, 60] and section 2.5) down to sub-femtosecond timescales, but also the direct excitation of single molecules at the atomic scale [61], which we will focus on here. At its inception, laser-assisted STM suffered from the thermal instabilities induced by the laser pulses [61, 62], which has seen significant improvements in recent years by introducing low-power laser sources [16, 63, 64]. Here, two techniques regarding the direct excitation of molecules will be highlighted.

Tip-enhanced Raman spectroscopy (TERS) was established in 2000 by Stöckle *et al.* [15], who studied C_{60} molecules situated on a thin glass support. This technique is based on the implementation of an optical laser to the STM setup, where the light scattered from the junction is analyzed. Due to the drastic electromagnetic enhancement in the tip-sample junction [65–67], Raman signals can be observed originating from single molecules located directly under the tip. TERS has since seen major improvements in the study of single molecules [19, 68–72], where it can be used to map vibrational modes with sub-molecular resolution [19] or study effects of resonant molecular excitation [72].

The second technique presented here is the laser-induced excitation of molecules on the surface, where, in contrast to TERS, the effects of the incident radiation are analyzed directly with the STM. This approach is aimed towards the study of photochemical processes down to the atomic scale [18], which has seen significant success in recent years. The applications of this technique range from triggering molecular motion [73] and dissociation of chemical bonds [21] to resonant photo-assisted electron tunneling [74]. One very recent development to be highlighted in this regard is the implementation of low-power tunable laser sources, which allow

the direct photoexcitation of single molecules in the junction [75, 76]. This enables the selective excitation [75] and subsequent photocurrent generation from the excited molecules [76]. In this approach, a single molecule situated in the tip-sample junction is directly photoexcited and electrons can tunnel between the STM electrodes and the excited state frontier orbitals of the molecule, which results in a photocurrent as a consequence of direct photoexcitation. This provides an immediate means to study molecular excited states and constitutes a related approach to the techniques presented in chapter 7 of this thesis.

2.5 Lightwave-Driven Scanning Tunneling Microscopy

The implementation of laser-assisted STM was originally intended to enable time-resolved experiments down to the picosecond scale [57, 58]. As mentioned before, this approach suffered from thermal instabilities introduced to the tunneling junction by the laser, which was overcome recently by implementing low-energy laser pulses [61].

During this development, lightwave-driven STM was established as a complementary technique to study light-matter interactions at their intrinsic length and time scales, which was first reported by Cocker *et al.* in 2013. In contrast to the techniques shown before, which rely on the direct photoexcitation of the junction, ultrashort THz laser pulses are used to modulate the bias voltage between tip and sample at the sub-picosecond time scale. Cocker *et al.* demonstrated the capabilities of this approach by directly measuring the decay of electron capturing of an InAs nanodot after photoexcitation [16]. These experiments were performed in ambient conditions, where also the coherent manipulation of electrons was shown [64]. The next breakthrough was the use of ultrafast THz pulses to analyze single molecules, which was achieved by Cocker *et al.* in 2016, where the vibrational motion of a single molecule was measured via femtosecond orbital imaging [20].

This sparked the recent progress towards imaging nanoscale processes in real time at the atomic scale using lightwave-driven scanning tunneling microscopy [77–83]. From the study of coherent acoustic phonons [79] to the investigation of ultrafast electric near field waveforms [81, 84, 85], this technique provides an access to previously unexplored nanoscale phenomena. In the scope of this thesis, lightwave-driven STM will be used in chapter 5 to exert atomic scale forces on a single molecule. Furthermore, it will be expanded upon in chapter 8, where the construction of a novel STM design specifically aimed at performing experiments with sub-femtosecond time resolution is described.

3 Atomic Force Microscopy

In this chapter the basic principles of atomic force microscopy will be discussed. These include the theoretical background of the technique as well as more advanced concepts relevant for the experiments discussed later in this thesis, which include Kelvin probe force spectroscopy, dissipative forces, experiments on thick insulating films and alternate-charging scanning tunneling microscopy.

3.1 Theoretical Background

The concept of atomic force microscopy (AFM) was first introduced by Binnig *et al.* in 1986 [7], which similarly to STM entails scanning a surface by use of a sharp tip. In contrast to STM, which monitors the tunneling current between tip and sample, AFM is based on the measurement of miniscule forces between tip and surface. These forces are detected by a cantilever to which the tip is mounted, which is deflected by the aforementioned forces between tip and sample. Measuring this deflection allows determining the forces between tip and surface. Due to their similar nature, STM and AFM are commonly summarized under the term scanning probe microscopy (SPM).

The force between tip and sample can be detected directly by the static deflection of the cantilever, which has been shown to yield atomic resolution [86]. However, this operating mode of the AFM is subject to the problem of a so-called jump-to-contact, where the tip snaps to the surface due to the attractive interactions between tip and sample [87].

In order to avoid this issue while still maintaining the atomic spatial resolution of AFM, it can also be operated in dynamic mode, where the cantilever is driven at its resonance frequency. During this, the forces acting between tip and sample cause the resonance frequency of the cantilever to change. This can lead to a variation of the oscillation amplitude, which yields information about the forces between tip and sample. This operating mode is called amplitude-modulation (AM). In frequency-modulation (FM) AFM, the excitation frequency of the cantilever is adjusted to the changed resonance, which allows the frequency shift to be monitored as a measure for the forces between tip and sample. This approach was first proposed by Albrecht *et al.* [88] and constitutes the main operating mode used for AFM experiments presented later in this thesis. To this end, it will be discussed in more detail in the following.

Figure 3.1a shows the operation of an AFM in FM mode, where the cantilever is driven at its resonance frequency f_0. Upon approaching the tip to the surface, the forces between tip and sample cause a frequency shift Δf. The stable operation in

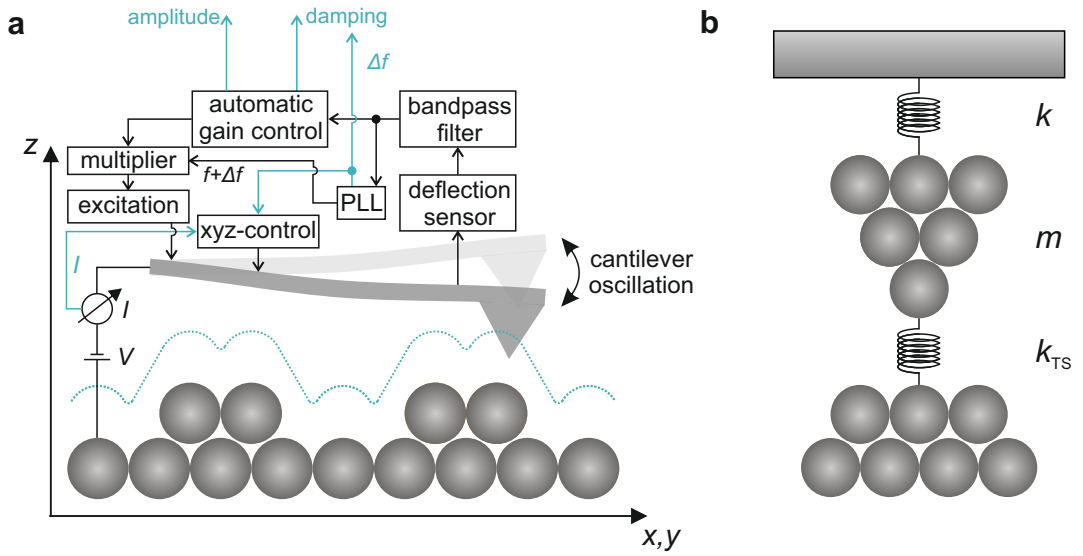

Figure 3.1: Working principle of an AFM. a, Sketch of the working principle of FM-AFM. **b**, Mass and spring model of an AFM. The cantilever with a spring constant k, tip-sample forces with an approximate spring constant k_{TS} and the mass m are indicated. After [89].

this mode requires the additional circuitry shown in figure 3.1a. First, the oscillation of the cantilever is measured, amplified and filtered via a band pass. The frequency shift Δf is subsequently detected by a phase-locked loop (PLL). In parallel, the cantilever is kept at a constant oscillation amplitude by an automatic gain control, which is achieved by applying a multiplication of $f + \Delta f$ and the output of the automatic gain control to the excitation of the cantilever [88, 89]. In the end, the AFM amplitude, the damping of the cantilever (in the form of the excitation required to keep the cantilever at constant amplitude) and the frequency shift Δf are output as observable quantities.

The AFM can also be operated in different feedback modes to adjust the tip sample distance. For example, the tip can be kept at a fixed height (constant height mode) while the change in Δf is recorded. Alternatively, a feedback loop can be employed to adjust the tip-sample distance such that the frequency shift Δf is kept constant (constant Δf mode). In combined STM/AFM systems, the current can also be used to adjust the tip height while the AFM is in operation.

Following the derivation shown in reference [89], the oscillating cantilever can be assumed as a mass m attached to a spring with an effective spring constant k, as shown in 3.1b. Its resonance frequency is then given by

$$f_0 = \frac{1}{2\pi}\sqrt{\frac{k}{m}}. \tag{3.1}$$

The force between tip and sample is approximated as an additional spring attached

between tip and sample with an effective stiffness of k_{TS}. For small cantilever oscillations, the force can thus be approximated by

$$F_{\mathrm{TS}} = -k_{\mathrm{TS}} \cdot z, \tag{3.2}$$

where z is the tip sample distance. Using this, the resonance frequency of the cantilever in contact with the sample is given by

$$f = \frac{1}{2\pi}\sqrt{\frac{k + k_{\mathrm{TS}}}{m}}. \tag{3.3}$$

In the case of a stiff cantilever, it can further be assumed that $k >> k_{\mathrm{TS}}$, from which follows:

$$f \approx f_0 \left(1 + \frac{k_{\mathrm{TS}}}{2k}\right) \tag{3.4}$$

Thus, the frequency shift can be expressed as

$$\Delta f = f - f_0 \approx f_0 \frac{k_{\mathrm{TS}}}{2k} = -\frac{f_0}{2k}\frac{\partial F_{\mathrm{TS}}}{\partial z}, \tag{3.5}$$

where $k_{\mathrm{TS}} = -\partial F_{\mathrm{TS}}/\partial z$ resulting from eq. 3.2 was used. Hence it was shown, that under these conditions the frequency shift in FM-AFM is proportional to the gradient of the force acting between tip and sample.

While there are several different forces acting between tip and sample [89], the experiments presented in chapter 7 predominantly measure electrostatic interactions between tip and sample, which will be discussed in detail in the following sections.

3.2 Kelvin Probe Force Spectroscopy

Kelvin probe force microscopy was first introduced by Nonnenmacher *et al.* in 1991 [90] and comprises a method to measure the (local) contact potential difference ((L)CPD) between an AFM tip and the sample. The CPD is defined as [91]

$$V_{\mathrm{CPD}} = \frac{\Phi_{\mathrm{T}} - \Phi_{\mathrm{S}}}{-e}, \tag{3.6}$$

where Φ_{T} and Φ_{S} are the work functions of the tip and the sample and e is the electronic charge.

The effects leading to this potential difference are illustrated in the energy level diagrams shown in figure 3.2. When the two electrodes are separated and not electronically connected, the energy landscape corresponds to the situation shown in figure 3.2a. Here, the tip and sample work functions are different, which leads to different Fermi energies for the two electrodes. Electrically connecting tip and sample causes a flow of electrons between tip and sample until both Fermi energies are equilibrated as

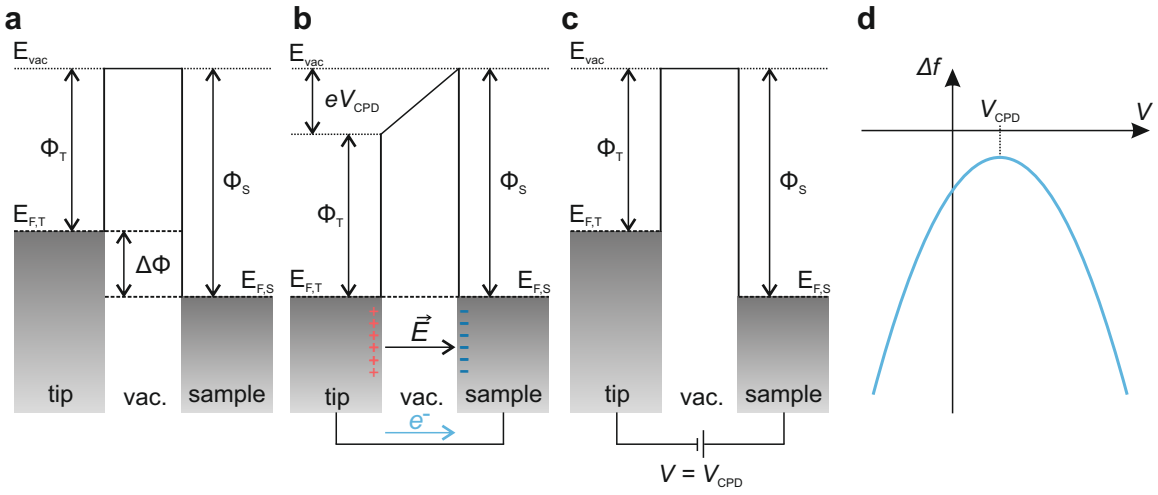

Figure 3.2: Kelvin probe force spectroscopy. **a**, Isolated tip and sample. **b**, Tip and sample in electrical contact. The difference in work functions cause a current to flow between the two electrodes, leading to an accumulation of surface charges and the alignment of the Fermi levels of the electrodes. **c**, Applying $V = V_{\mathrm{CPD}}$ to the junction minimizes the electrostatic force between the electrodes. **d**, Sketch of a $\Delta f(V)$ curve, showing the quadratic dependence of Δf on V. After [91]

shown in figure 3.2b. This current results in surface charges in tip and sample, which in turn leads to an apparent voltage (V_{CPD}) shifting the energy levels of tip and sample relative to each other. Furthermore, an electrostatic force between tip and sample is caused by the accumulation of surface charges. This force can be counteracted by applying an external bias voltage of $V = V_{\mathrm{CPD}}$ between the electrodes, which removes the surface charges and thus nullifies the electrostatic interaction, which is shown in 3.2c [91].

In the following, a brief derivation outlining the dependence of the frequency shift (and thus the electrostatic force) is shown, which follows ref. [92]. Neglecting the curvature of the AFM tip, one can assume that tip and sample can be described as a plate capacitor. The energy stored in this capacitor is then given by

$$U_{\mathrm{el}} = \frac{1}{2} C(z)(V - V_{\mathrm{CPD}})^2, \tag{3.7}$$

where z is the tip-sample distance, $C(z)$ is the capacitance as a function of z and V is the applied bias voltage. Similarly to the derivation shown in the previous section, the frequency shift caused by these electrostatic forces is given by

$$\Delta f_{\mathrm{el}} \propto \frac{\partial F_{\mathrm{el}}}{\partial z} \propto \frac{\partial^2 U_{\mathrm{el}}}{\partial z^2} \propto \frac{1}{2}\frac{\partial^2 C(z)}{\partial z^2}(V - V_{\mathrm{CPD}})^2 \tag{3.8}$$

Here it becomes apparent that the frequency shift has a quadratic dependence on

the bias voltage, which is also shown in figure 3.2d. Furthermore, the contribution of the electrostatic forces is minimal for $V = V_{\mathrm{CPD}}$. While this technique was initially proposed as a method to detect local work function differences while recording topographic images [90], the analysis of the frequency shift Δf as a function of the applied bias voltage, called Kelvin probe force spectroscopy (KPFS), found much more versatile applications. Due to the ability to detect variations in the electrostatic interactions, KPFS can be utilized to discriminate different charge states of atoms and molecules [93–95] or to map the charge distributions of individual molecules [96, 97]. This technique will also be applied in chapter 7 of this thesis.

3.3 Dissipative Forces

As a damped, driven harmonic oscillator, the AFM cantilever is subject to dissipation (i.e. energy loss) during its oscillation. The energy loss per oscillation cycle is given by [98]

$$\Delta E = 2\pi \frac{E}{Q} \quad \text{with} \quad E = k\frac{A^2}{2}, \tag{3.9}$$

where Q is the quality factor of the cantilever, E is the energy stored in the cantilever oscillation, k is the stiffness of the cantilever and A is the oscillation amplitude. Whilst the majority of forces between cantilever and sample studied in FM-AFM are conservative forces, which cause a shift of the resonance frequency of the cantilever as discussed above, non-conservative forces can lead to an additional damping of the cantilever. The energy dissipated per cycle by such a force is given by [87]

$$\Delta E_{\mathrm{TS}} = \oint F_{\mathrm{TS}}(z+q)dq, \tag{3.10}$$

where the tip-sample force F_{TS} is integrated along the pathway of a full cycle of the cantilever oscillation.

A scheme of a non-conservative force is shown in figure 3.3. A rapid change in the force between sample and cantilever, for example due to charging a molecule located below the tip, leads to an abrupt shift of the force curve (figure 3.3a) due to the additional electrostatic force. As will be discussed later, the discharging of the molecule can occur at a different cantilever position, which results in a non-constant force during a single cantilever oscillation and thus in an additional energy loss (or gain, depending on the direction of the forces) of the cantilever. This is further illustrated in figure 3.3b. Here, the cantilever position and the forces between tip and sample are shown. Due to the additional forces appearing and disappearing at different cantilever positions, the integral in equation 3.10 will be non-zero and consequently lead to an additional damping of the cantilever.

Dissipative forces were analyzed in AFM experiments in, for example, the study of molecular hydrogen [100] or excited states of quantum dots [101]. Very recently, also phenomena relating to charge transfer between molecules [102] and the shuttling

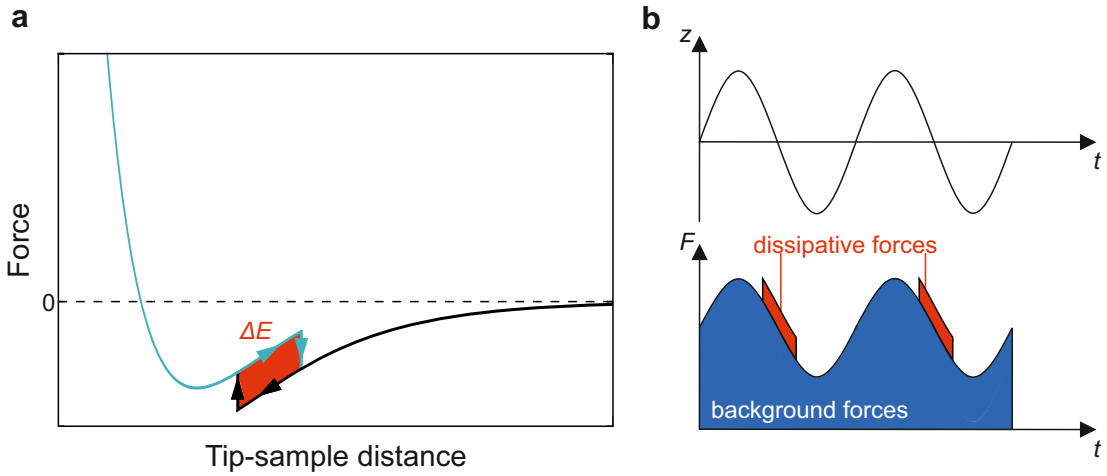

Figure 3.3: Dissipative forces in FM-AFM. a, Schematic of two different force curves leading to a dissipative force. The dissipated energy is given by the area marked in red. **b**, Position of the cantilever (top) and forces acting on the cantilever (bottom). The additional dissipative forces are indicated in red. After [99].

of electrons between the AFM tip and single molecules [99, 103, 104] made use of the dissipation arising in these experiments. It has also been shown that sequential tunneling of electrons can also lead to a dissipative force on the cantilever [105].

In chapter 7 of this thesis, we will also analyze dissipative forces due to changes in the electrostatic interactions between tip and sample during a single cantilever oscillation. Since the dissipated energy is directly proportional to the excitation required to keep the AFM amplitude constant, we use this damping signal as a measure for the dissipated energy, which is directly output by the AFM electronics (see also figure 3.1a).

3.4 AFM on Thick Insulating Films

Since AFM does not require a conductive substrate, experiments can also be performed on insulators. In recent years, methods to examine molecules and atoms on thick insulating layers have been developed. This approach entails that molecules and atoms situated on these films exhibit charge stability since the charges can not escape via tunneling to the metallic substrate. While this charge state control has also been demonstrated for atoms and molecules on thin insulating films [106–109], the stability of charged adsorbates on thin films delicately depends on the energy alignment with the substrate.

By depositing molecules on a bulk-like insulator grown on a metallic substrate, charge state control can be extended to a wider selection of systems as reported by Steurer *et al.* in 2015 [94]. Here, the charge stability and high sensitivity of the AFM

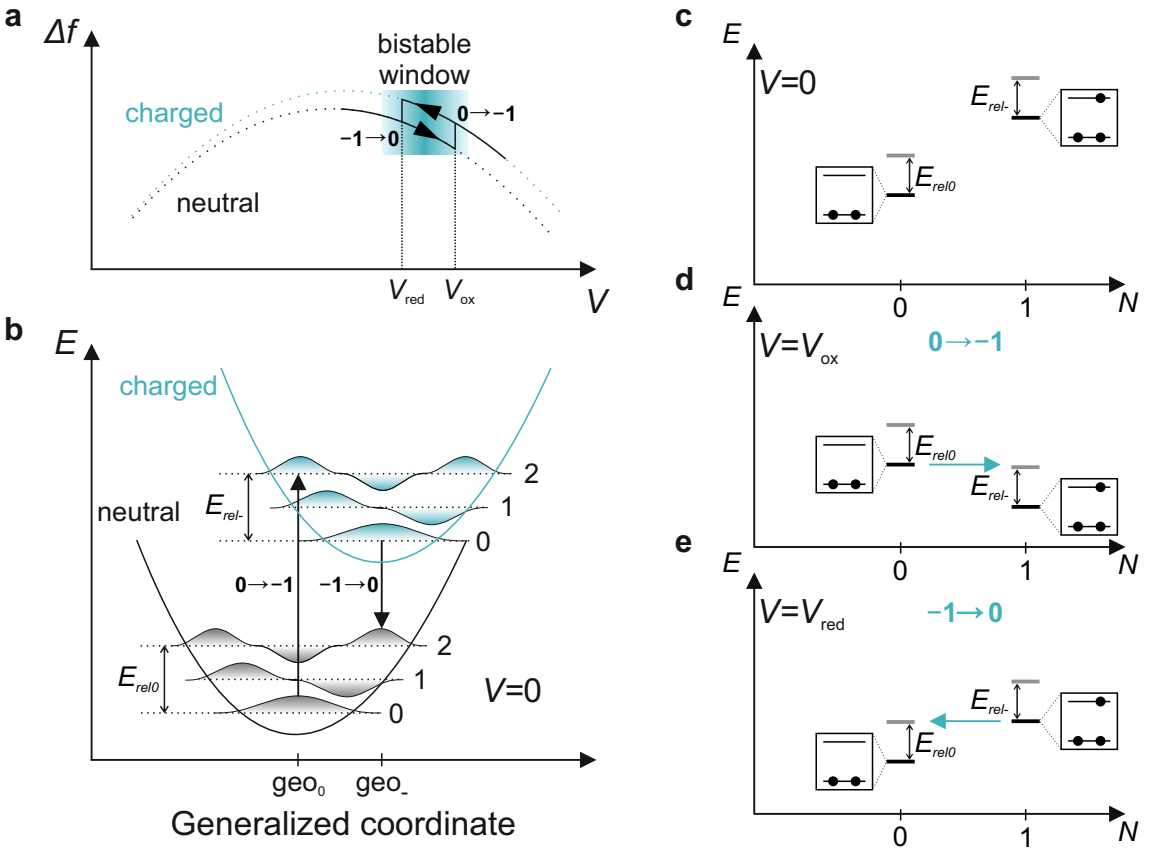

Figure 3.4: Schematic charging processes and many-body energy diagrams for a molecule on thick NaCl. **a**, Sketch of a typical $\Delta f(V)$ curve obtained on a single molecule. Due to the charging and discharging of the molecule, the $\Delta f(V)$ curve abruptly jumps between the two parabolas of the respective charge states (dashed lines). **b**, Frank-Condon picture showing neutral and anionic states with the respective vibrational modes. Vertical arrows indicate transitions between neutral and charged states. **c-e** Many-body energy diagrams for different applied bias voltages V. The blue arrows indicate the transition from neutral to charged state and vice versa.

was used to laterally transfer electrons between individual pentacene molecules. This environment allows the study of a multitude of effects, such as the fragmentation of a molecule via doubly charged states [110], bond-order changes in a single molecule upon charging [93], probing molecular excited states [111] or single molecule triplet quenching [112].

As the experiments in chapter 7 are performed in this environment, some important effects arising from the charging of molecules on bulk-like NaCl are shown in the following.

A schematic $\Delta f(V)$ curve obtained above a single molecule situated on thick NaCl is shown in figure 3.4a, the parabolic shape for which was discussed in section 3.2. The

charging of the adsorbate under the tip causes an abrupt change in the electrostatic interaction, which is manifested in a jump to a different parabola for the charged state (dashed lines). This behavior has been reported in experiments on molecules [94] as well as single atoms [95] exhibiting charge stability. It has been found that charging and discharging takes place at different bias voltages, leading to a hysteretic behavior and a voltage window in which both charge states are stable. It should be noted that charging and discharging are caused by electron tunneling to or from the tip, which implies that the exact voltages are subject to the probabilistic nature of tunneling and thus can change for each individual $\Delta f(V)$ curve.

The cause for the hysteretic behavior is the relaxation of the adsorbate and the substrate due to the effects of the additional charge localized at the surface, usually referred to as reorganisation [113]. This behavior can be explained via the Franck-Condon picture as shown in figure 3.4b, which is usually used to describe spectroscopic effects [114], but can also be employed for charge transitions [113, 115]. When the adsorbate is caused to transition from the neutral to the charged state, the probability for this transition is dependent on the spatial overlap of the vibrational wave functions of the initial and the final state. This overlap is usually larger when transitioning from the neutral (charged) vibrational ground state to one of the vibrationally exited states of the charged (neutral) configuration. After this excitation, the adsorbate will relax into the vibrational ground state, the energy gain of which is called relaxation energy (E_{rel0} and E_{rel-} in figure 3.4b). The total reorganization energy is given by $E_{reorg} = E_{rel0} + E_{rel-}$ [113] and is referred to as Marcus reorganisation energy [116].

Since this behavior is important for charging processes of molecules on thick insulating films, it is necessary to incorporate this effect when analyzing the tunneling processes involved in these experiments. However, this effect is difficult to include in a single-particle picture as shown for example in figure 2.2. To this end a many-body energy diagram [111, 117, 118] is proposed as shown in figures 3.4c-e. Here, the free energy E of the respective states is given as a function of the number of additional electrons N. The relaxation energies of the respective states are also indicated. Applying a bias voltage shifts the free energies of the states with respect to each other (see fig. 3.4d). Once the voltage is sufficiently large, the molecule can transition from the vibrational ground state of the neutral molecule to the vibrationally exited state of the charged molecule (blue arrow in 3.4d). Decreasing the voltage again can only cause the discharging of the molecule if the overlap between the states involved in the transition is large enough (see fig. 3.4e).

3.5 Alternate-Charging Scanning Tunneling Microscopy

As discussed in the previous section, AFM can be used to inject or remove single electrons from individual molecules deposited onto a thick insulating layer on a metal substrate. This approach, however, lacks the direct access to the electronic structure

of the investigated molecules provided by STM, which requires a conductive substrate (see also section 2.2). Patera *et al.* overcame this restriction in 2019 with an approach called alternate-charging scanning tunneling microscopy (AC-STM) [99].

This technique is based on the implementation of voltage pulses with alternating polarity which are synchronized with the cantilever oscillation. Using a small oscillation amplitude of 1 Å, they set the direct current (DC) voltage to be in the center of the bistable window of the charging hysteresis (figure 3.4a). The voltage pulses are used to charge the molecule at the top turning point of the cantilever oscillation (i.e. when tip is far away from the molecule; set pulse) and discharge it at the bottom turning point (i.e. small tip molecule distance; reset pulse). This way, the electrostatic interaction between tip and molecule is different when the tip is moving inward compared to moving outward, leading to a dissipative force acting on the cantilever (see also section 3.3). The height difference between set and reset pulse also implies, that resetting the molecule is significantly more efficient, as the tunneling yields for the reset pulse is roughly a factor of 100 larger than the yield for the set pulse. This entails, that the spatial signature of the signal is predominantly governed by the set pulses, since the pulses at the bottom turning points of the oscillation always reset the redox state.

This novel imaging has thus far been used to study the Jahn-Teller effect in CuPc [99], the stabilization of a bistable molecular switch [103] and the charge localization effects in single molecules [104]. In this thesis, this technique is also used in chapter 7 in order to characterize the orbital structure of the molecules under investigation. Furthermore, a similar voltage pulse scheme is employed to facilitate resetting the charge state of the molecule in a similar manner.

4 Experimental Setup & Methods

In this chapter, the experimental setup will be described. Furthermore, the techniques used for sample preparation will be discussed.

4.1 Experimental Setup

The experiments shown in chapters 6 and 7 were performed on a home-built, combined STM/AFM setup, which is depicted in figure 4.1. The data shown in chapter 5 was acquired using a different apparatus, which employs the same chamber and cryostat design, but is only capable of performing STM experiments. Furthermore the scan unit of this apparatus was modified to include optical elements in order to perform lightwave-driven STM experiments [20] (see also sections 5.2 and 8.2).

The entire ultra-high-vacuum (UHV) system can be divided into three separate chambers, namely the load-lock, the preparation chamber and the SPM chamber. When bringing equipment such as samples into the vacuum, they are inserted into the load lock, which is pumped by a diaphragm pump and a turbomolecular pump, which allow pressures down to the 10^{-9} mbar regime. The preparation chamber can reach lower pressures below 10^{-10} mbar due to the connected ion getter pump and the titanium sublimation pump. This chamber is equipped with the necessary tools for sample preparation, such as a sputter gun, a leak valve for gas dosing and salt evaporators. Furthermore, a manipulator located at this chamber allows moving equipment in the UHV chamber and transferring samples to the SPM. The scan head is mounted to the bottom of a bath cryostat, which is positioned in the SPM vacuum chamber and allows experiments at temperatures below 10 K.

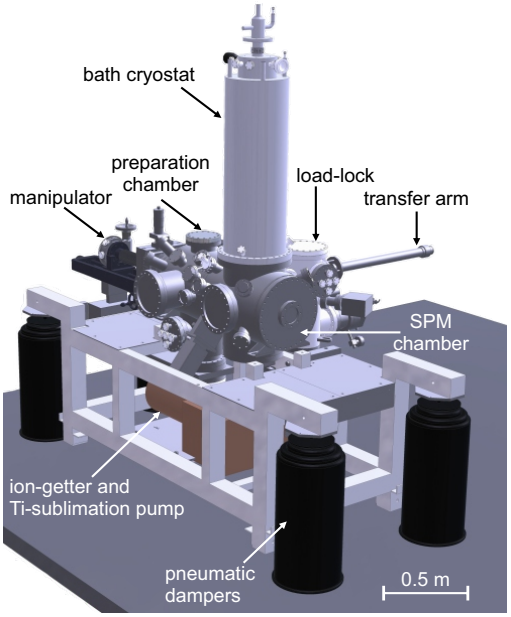

Figure 4.1: Overview of the combined STM/AFM apparatus. Rendered image of the low-temperature, ultra-high-vacuum combined STM/AFM system. Image from [119].

A cross-section of the cryostat is shown in

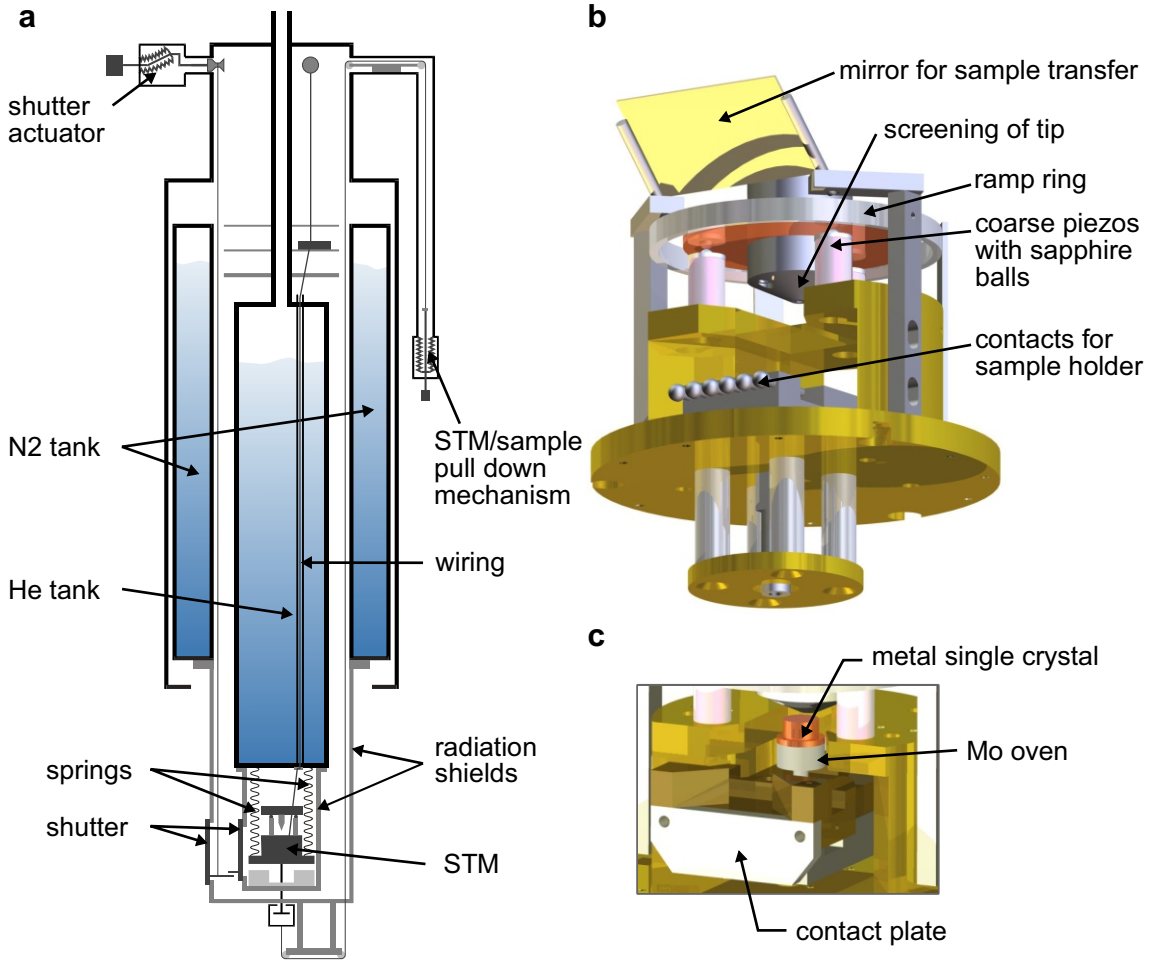

Figure 4.2: Drawings of the cryostat and the SPM scan head. **a**, Cross-section of the cryostat, which is comprised of a helium and nitrogen tank separated by vacuum. **b**, Rendered image of the SPM scan unit. **c**, Detailed view of the scan head with an inserted sample. Image from [120].

figure 4.2a, which consists of two main tanks, where the inner one is filled with liquid helium and the outer one with liquid nitrogen. The two tanks are decoupled from the environment and each other via vacuum insulation. At the bottom of the cryostat, the scan unit (see fig. 4.2b) is mounted using springs. It is manufactured in a Besocke design [121], where the sensor unit is mounted to the bottom of a ramp ring, which consists of three sloped surfaces. This is positioned on a set of three piezo tubes which allows the movement of the tip in all three spatial directions, either microscopically by applying a constant voltage to the tubes or macroscopically by performing slip-stick motions. A low-temperature preamplifier is mounted close to the scan head (not shown in figure 4.2). The sample holder is inserted into the scan unit with the manipulator (figure 4.2c), where the electrical contacts are used to supply a bias voltage to the sample, while the tip is kept at virtual ground.

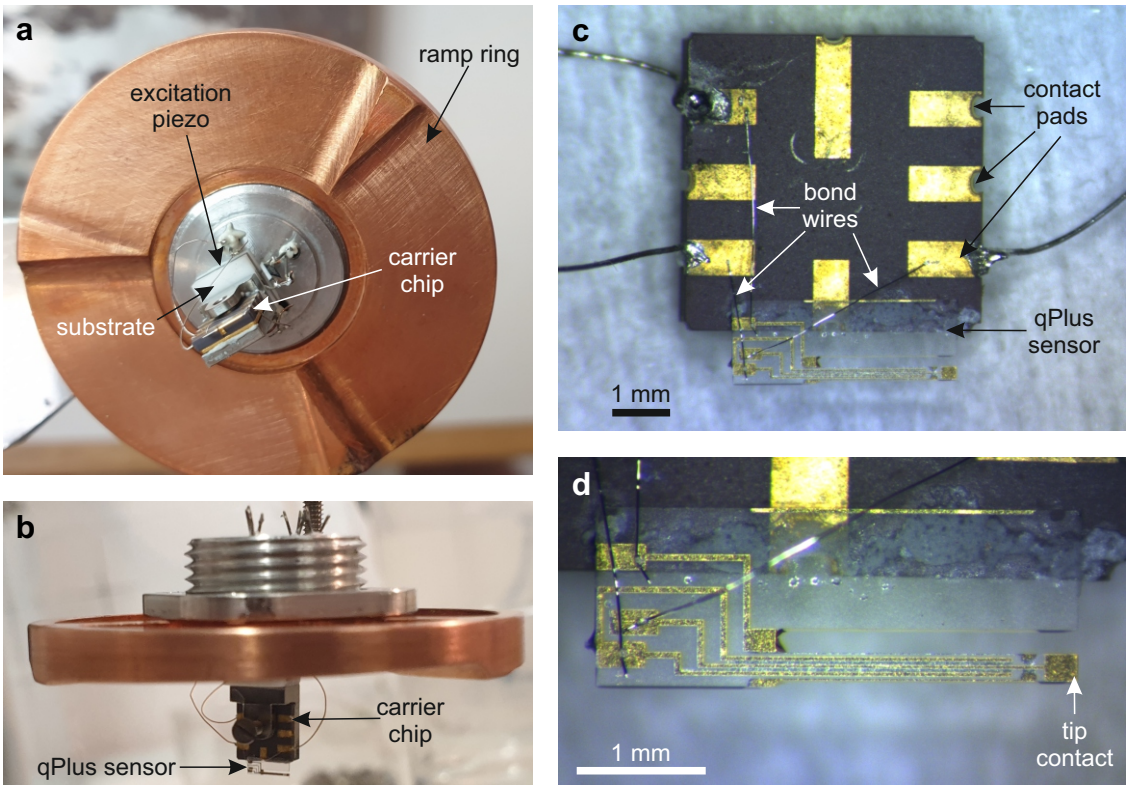

Figure 4.3: Ramp ring and qPlus sensor design. **a**, Bottom view of the ramp ring with the sensor unit attached. The cantilever can be excited by a piezo element positioned between the substrate and the ramp ring. **b**, Side view of the ramp ring with the sensor unit attached. **c**, qPlus sensor attached to the carrier chip. **d**, Detailed view of the qPlus sensor. The position where the tip will be attached is indicated.

The ramp ring and sensor design are shown in detail in figure 4.3. Figure 4.3a depicts the ramp ring from a bottom view, where the inclined ramps positioned on the piezo tubes are visible. In the center of the ramp ring a substrate with a holder for a carrier chip is located. The qPlus sensor used for the combined STM/AFM measurements is attached to this chip, as is shown in figure 4.3b. The gold-plated electrodes on the sensor are connected to the contact pads on the chip via wire bonding (figure 4.3c), to which wires are soldered guiding the signals through the ramp ring and out of the apparatus. A cut Pt/Ir tip is mounted to the front contact pads of the cantilever, allowing simultaneous STM/AFM experiments (figure 4.3d. Here, the tip is not yet mounted, but its final position is indicated.).

The qPlus sensor used in this apparatus was introduced by Giessibl in 1998 [122] and has since become one of the most versatile and widely used sensors for high-resolution AFM [87] due to its high stiffness, its ability to be operated at amplitudes at the sub-nanometer scale and its detection based on the piezoelectric effect [87, 123].

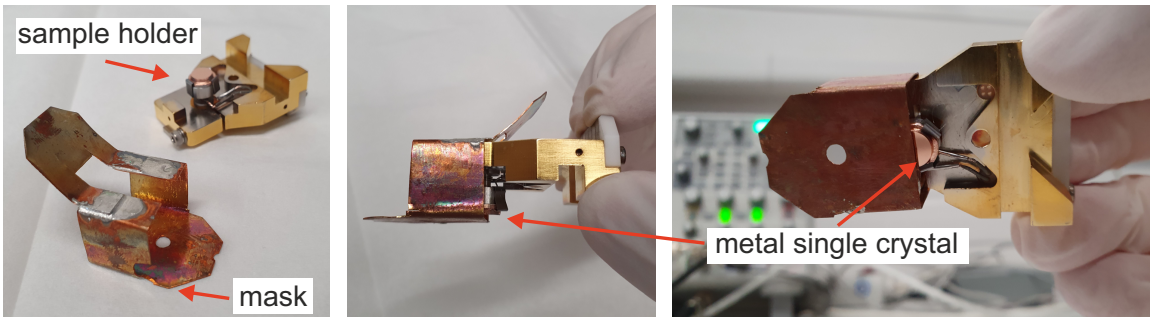

Figure 4.4: Preparation of thick NaCl layers using a mask. Images of a sample holder and the mask used to screen half of the sample from NaCl evaporation. The side (middle image) and top (right image) views reveal, that only half of the metallic substrate are exposed to NaCl deposition. Image from [124].

4.2 Sample Preparation

Throughout chapters 5 to 7 of this thesis, Cu(111) was used as a metal substrate. In order to achieve a flat and clean surface to perform experiments on, the sample was prepared via repeated cycles of sputtering and annealing. For the sputtering process, neon gas was dosed through a leak valve into the preparation chamber up to a pressure of $p \approx 5 \cdot 10^{-5}$ mbar, which is ionized and accelerated towards the sample. The sputter gun used was operated at emission currents of $12-20$ mA and the acceleration voltage was set to 1 kV. After sputtering the sample with these parameters for $20-30$ minutes, the copper sample was heated to 550 °C, using a small oven onto which the sample is mounted (see also figure 4.2c). The annealing temperature was reduced to 500 °C for the last annealing cycle.

After these steps, NaCl was thermally evaporated onto the sample from a tantalum crucible. The amount of NaCl evaporated is monitored by a quartz microbalance. The growth of the NaCl on the metallic substrate is dependent on both the temperature of the sample during deposition and the amount of NaCl evaporated and has to be adjusted to suit the planned experiment. Thus, the sample temperature during NaCl deposition is given in the methods sections of chapters 5 to 7.

For the experiments shown in chapter 7, it was required to deposit thick NaCl films of > 20 monolayers (ML). Since the tip is usually prepared at the atomic scale via controlled indentation into the metallic substrate, such a large coverage would prevent this technique and cause contamination of the metallic tip upon crashing into the NaCl. To this end, a mask was designed which can be slipped onto the sample holder (figure 4.4) [124], such that only half of the sample will be covered by NaCl, while the other half remains clear metal on which the tip can be prepared.

After these steps, the sample and manipulator were cooled to ≈ 80 K by LN_2 and transferred into the cold (< 10 K) STM/AFM. Molecules were deposited onto the cold sample via flash evaporation from a silicon wafer.

5 Coherent Control of a Single-Molecule Switch via Sub-Cycle Atomic-Scale Forces

The results presented in this chapter have been obtained and interpreted in collaboration with Dominik Peller, Lukas Kastner, Carmen Roelke, Florian Albrecht, Nikolaj Moll, Rupert Huber and Jascha Repp, and were published in Nature [80] . Nikolaj Moll performed the density functional theory (DFT) calculations. The presentation of the results closely follows the publication, where parts of the text and figures are adopted identically.

In this chapter, THz-STM experiments on the coherent control of a single molecule switch are presented. We use a single magnesium phthalocynanine (MgPc) molecule adsorbed on a thin NaCl film as a model system for such a molecular switch, which can adsorb in a bistable geometry. Coupling a THz transient tuned in resonance with one of the molecular orbitals to the tunneling junction can cause charging of the molecule and subsequent switching between the two stable geometries. This behavior is monitored by employing a single shot detection scheme, which allows us to perform ultrafast action spectroscopy measurements.

We find that the probability to switch the molecule can be influenced by the electric field of an THz pulse, indicating that it acts as an ultrafast force transient on the molecule. Comparing the marked oscillation of the switching rate to simulations of the system, we find that applying the force transient to select atoms within the molecule causes a frustrated in-plane rotation of the molecular frame, leading to the aforementioned modulation of the switching rate. Maps of the switching rate across the molecule reveal the atomic scale nature of the applied forces.

5.1 Introduction

Since their inception, scanning probe techniques have been used to manipulate individual nanoscale objects and assemble them into novel quantum structures. One of the first major breakthroughs in this field was achieved by D.M. Eigler *et al.*, who demonstrated that individual atoms can be manipulated using the STM tip [11]. This concept was further expanded on by M. Crommie *et al.*, who showed that individual atoms can be used to build quantum corrals on a metal surface [125]. Building on these results, it has been shown very recently by F. Stilp *et al.* that these artificial atoms can also form a bond to the front metal atom of an AFM tip [126].

However, this control of individual adsorbates even extends to single molecules. These manipulation techniques have been successfully used to fabricate molecular cascades [127], which can be arranged into the form of logic gates, or to drive molecular motors [128], which are essential for biological processes [129]. The precision of scanning probe techniques also allows inducing chemical reactions with sub-molecular accuracy [130–133].

One way to build these novel structures is the exertion of a local force down to the atomic scale. This holds true for both structures built from atoms [134], as well as causing chemical reactions in molecules [132, 133]. The access to these processes could be further enhanced by exploiting the local dynamics, which would allow for coherent control of the relevant reaction processes at the atomic scale [135–139].

In parallel to these developments in the fabrication and control of quantum structures at surfaces, the inception of new ultrafast techniques paved the way for studying molecular movement down to the intrinsic timescales of their dynamics. With these techniques, chemical reactions [140–142] and conformational changes [143] have been examined. While these studies provide astonishing insights into the temporal evolution of molecular systems, monitoring them with atomic scale spatial resolution would present a pathway to probing sub-molecular dynamics.

This was achieved by the combination of scanning probe and laser based techniques. Here, either femtosecond laser pulses are coupled to the tip-sample-junction [135, 138, 144], causing several processes to be triggered and examined, or a tip-enhanced Raman-scattering signal is analyzed, which also provides information of the local dynamics [136, 137, 139]. While these techniques allowed studying local dynamics at sub-molecular length scales, a direct way to exert forces on individual atoms within a molecule and thus coherently control molecular motion has so far remained elusive.

The results presented in this chapter will show a way to coherently control a single molecule switch down to the sub-molecular level. By employing a novel combination of lightwave-driven scanning tunneling microscopy [16, 20, 64, 82] with ultrafast action spectroscopy [73, 135], we trigger and control the ultrafast dynamics of a bistable molecular switch directly via femtosecond atomic-scale forces. To this end we employ a terahertz wave confined to an atomically sharp tip, whose near field exerts a localized, ultrafast force and selectively induces a frustrated rotation of the molecular

frame. We find that these dynamics can modulate the switching probability between the two stable states of the molecule upon abrupt charging by up to 39 %. Furthermore, we resolve the molecules response to the ultrafast terahertz transient in space and time, which confirms and underlines the atomic and sub-optical-cycle nature of the resulting forces.

5.2 Sample Preparation & Methods

STM setup The setup used in this experiments is a modified version of the apparatus shown in chapter 4.1. While the cryostat and vacuum chamber follows the same design, the scan unit is only capable of performing STM experiments. Furthermore, the collimated THz laser enters the vacuum chamber through a sapphire viewport and is focused onto the tip-sample junction by a parabolic mirror fixed to the STM scan unit (see also section 8.2).

Sample preparation The Cu(111) metal substrate was cleaned via multiple cycles of neon sputtering and thermal annealing to 550 °C. Sodium chloride was evaporated thermally onto the clean metal at $\approx$ 275 K to form bi- and trilayers. Magnesium phthalocyanine molecules are deposited onto the cold substrate ($T < 15$ K) inside the STM scanner via flash evaporation from a silicon wafer.

THz optical setup Intense, phase-locked THz pulses with a centre frequency of 1.1 THz are generated by tilted-pulse-front optical rectification of femtosecond near-infrared pulses (centre wavelength, 1028 nm; full width half maximum pulse duration, 250 fs) from a regenerative ytterbium-doped potassium gadolinium tungstate (Yb:KGW) laser amplifier (repetition rate tuneable from 0.61 MHz down to single shot) in lithium niobate. Pairs of mutually delayed THz transients are prepared by transmitting the THz pulses through a Michelson interferometer, in which the computer-controlled position of one end mirror sets the delay time τ. Using crossed wire grid polarizers, the THz field amplitude is continuously controlled, for both pulses individually, without changing the waveform. Their field directions can be reversed separately.

5.3 Magnesium Phthalocyanine as a Single Molecule Switch

The molecule investigated is magnesium phthalocyanine (MgPc), a metal phthalocyanine complex which has been studied in various STM experiments [38, 145, 146]. These molecules are adsorbed onto a thin layer of sodium chloride (NaCl) on a supporting Cu(111) substrate in order to electronically decouple them from the underlying metal. On this insulating film, these molecules can adsorb with the metallic

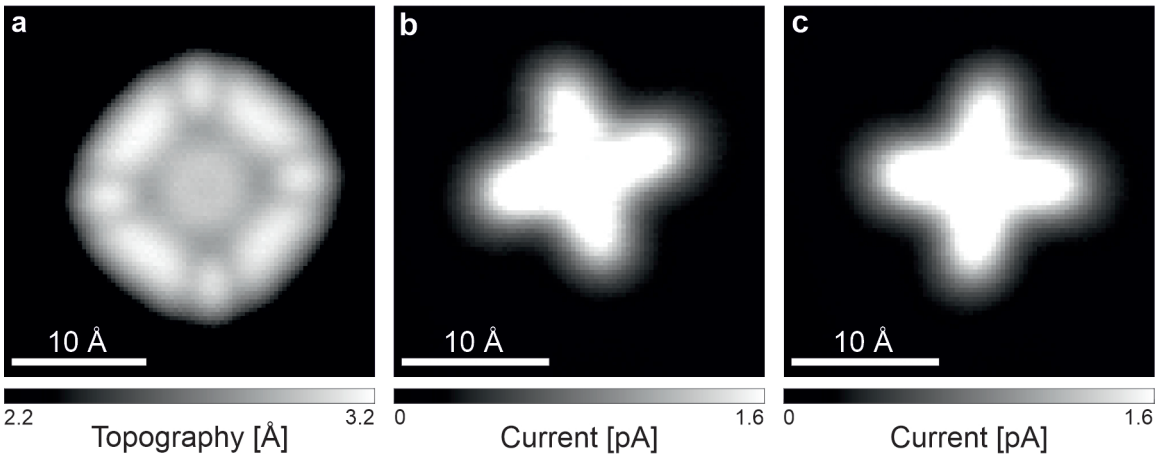

Figure 5.1: DC-STM investigation of MgPc on NaCl/Cu(111) a, Constant current image of the LUMO of MgPc. The repeated charging of the molecule while scanning causes it to repeatedly switch between two stable adsorption geometries; Setpoint: 1.1 V, 2 pA **b**, Constant height images of the left-oriented geometry ($|l\rangle$) of the same molecule as shown in **a**. Bias voltage: 6 mV **c**, Right-oriented geometry ($|r\rangle$) of the molecule. Bias voltage: 6 mV.

center either centered on a sodium or chlorine site, where in this study we focus on the latter.

The metallic center adsorbing on a chlorine site leads to a distinctive configuration of the molecule, which is depicted in figure 5.1. Imaging the lowest unoccupied molecular orbital (LUMO) of a molecule in this geometry shows a very distinctive contrast (figure 5.1a). This is due to a rapid toggling of the molecule between two stable adsorption geometries (figures 5.1b and c), which results in the image showing a superposition of the LUMOs of the molecule in these stable geometries. The exact mechanism for this behavior will be discussed below. The axes of the neutral molecule, however, are rotated by an azimuthal angle of either $\phi_l = +10°$ or $\phi_r = -10°$ with respect to the high symmetry direction of the underlying NaCl layer. Since this allows for the precise manipulation of the molecule, MgPc constitutes a single molecule switch.

Such a molecular switch represents a model system to study the control of its switching behavior in the most direct and non-invasive way possible. This is realized by exerting a atomic scale force on the molecular frame, which leaves the system in its electronic ground state. While static forces, available with scanning probe microscopy, could induce a static excursion, a time-dependent ultrafast force pulse, $F(t)$ may prepare a coherent frustrated rotation of the molecule around one of its neutral ground state geometries. It will be discussed below that such an atomically sharp ultrafast force can indeed be provided by the oscillating carrier wave of a strong terahertz (THz) pulse coupled to the metallic tip of a scanning tunneling microscope (STM). The force-induced all-structural wavepacket dynamics can be strong enough

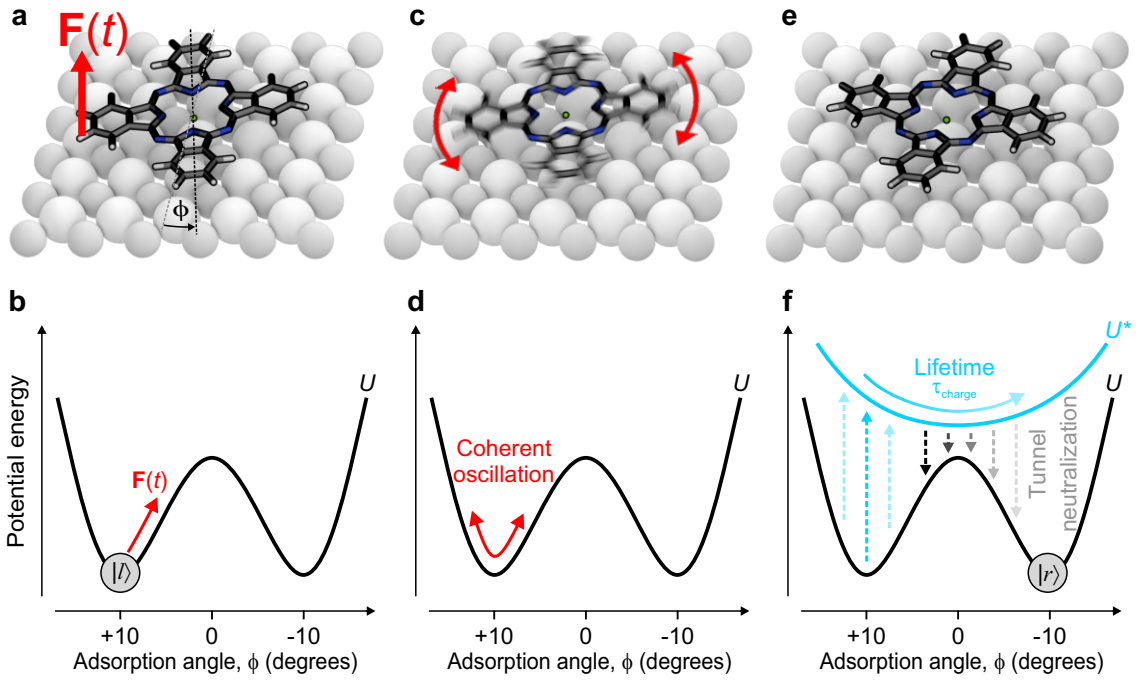

Figure 5.2: Coherent control of structural dynamics of a single-molecule switch by a local ultrafast force stimulus. a, MgPc molecule adsorbed in the left rotated geometry $|l\rangle$. An applied force transient to the molecular frame is indicated by a red arrow. **b**, Associated potential energy landscape of the neutral molecule. It features two minima, where the applied force transient causes an acceleration of the molecular frame. **c**, **d**, Coherent in-plane oscillation of the molecule resulting from the force transient, which could be exploited to control the switching dynamics to state $|r\rangle$ (**e**). **f**, Charging the molecule causes it to be subject to a different potential, leading to a rotation towards $\phi = 0°$. After the stochastic tunnel neutralization, it can switch to the other adsorption geometry.

even to influence the probability of the molecule to switch between its stable states.

In order to thoroughly assess the involved processes, they are discussed step by step (figure 5.2). The neutral adsorption geometry of the molecule is subject to a double well potential $U(\phi)$ with two degenerate minima at $\phi_l = +10°$ and $\phi_r = -10°$. This means, that in equilibrium, the neutral MgPc molecule adsorbs in either of two degenerate, mirror symmetric ground states $|l\rangle$ (figures 5.2a and b) or $|r\rangle$. When a local, ultrafast force pulse is applied to the molecule in one of these two stable positions, the time-dependent force transient will cause an acceleration of the molecule. This acceleration will trigger a coherent oscillation of the molecule around the local potential minimum (figures 5.2c and d).

This coherent oscillation will later be probed via charging the molecule. As has been shown before in figure 5.1a, the molecule can be switched between the two stable geometries upon charging, which has also been demonstrated in other experiments

[103], while the neutral molecule remains stable in one of the two orientations. Since the charged molecule is subject to a different potential $U^*(\phi)$, whose minimum lies around $\phi = 0$, charging will cause an in-plane rotation of the molecule towards $\phi = 0$ [103, 146]. This motion is strongly influenced by the previously induced dynamics. After a short lifetime τ_{charge}, tunneling neutralization of the molecule will occur. As this process occurs stochastically at different instants in time, the outcome of every individual switching process is governed by quantum probability.

The idea is now to specifically trigger the molecular switch with an ultrafast time-delayed electron injection event, as has recently become available with femtosecond lightwave-driven STM [16, 20, 64, 73, 82, 135]. In summary, a coherent, frustrated in-plane rotation of the molecule is triggered by an ultrafast, local force pulse. After a defined time delay, the molecule is then charged via an ultrafast THz pulse and can thus be switched to the other stable adsorption geometry with a certain probability. This probability will in the end be influenced by the coherent oscillation caused by the applied force pulse.

5.4 Ultrafast Action Spectroscopy

In order to assess the impact of an ultrafast atomic scale force acting on the single-molecule switch, it is important to first understand the switching behavior triggered by lightwave-induced resonant electron injection, in the absence of a force pulse $F(t)$. In contrast to the recent demonstration of lightwave-driven STM [16, 20] (see also chapter 2.5), the THz-induced tunneling current is not monitored here. For this, a large amount of electrons has to be driven through the molecular orbitals to achieve a measurable current. This, however, would cause the molecule to shuttle rapidly between the sites, similar to the steady-state STM experiments shown in figure 5.1a. To this end, detecting the structural change of the single molecule switch is being focused on here. Since the system does not relax into the same initial state after every laser shot, but rather toggles between the two stable states, the outcome of every laser shot needs to be evaluated, one by one. This concept, called single-molecule action spectroscopy [144], has recently reached combined sub-Å spatial and femtosecond temporal precision [73, 135].

This concept is further extended to time scales shorter than even a single cycle of light. The THz laser source inducing ultrafast electron injection is operated in single-shot mode to toggle the single molecule switch with a certain probability. Steady-state imaging at low bias voltages monitors the adsorption geometries $|l\rangle$ and $|r\rangle$ without switching between them (figures 5.3a and b).

In order to resolve every single switching event [147, 148] of the molecule, a detection mechanism that allows us to continuously monitor the molecule's adsorption geometry is utilized, extending previously reported implementations of action spectroscopy in STM [144, 149–151]. To this end, the tip is first positioned above the bare NaCl substrate close to the molecule which will be examined. The tip height

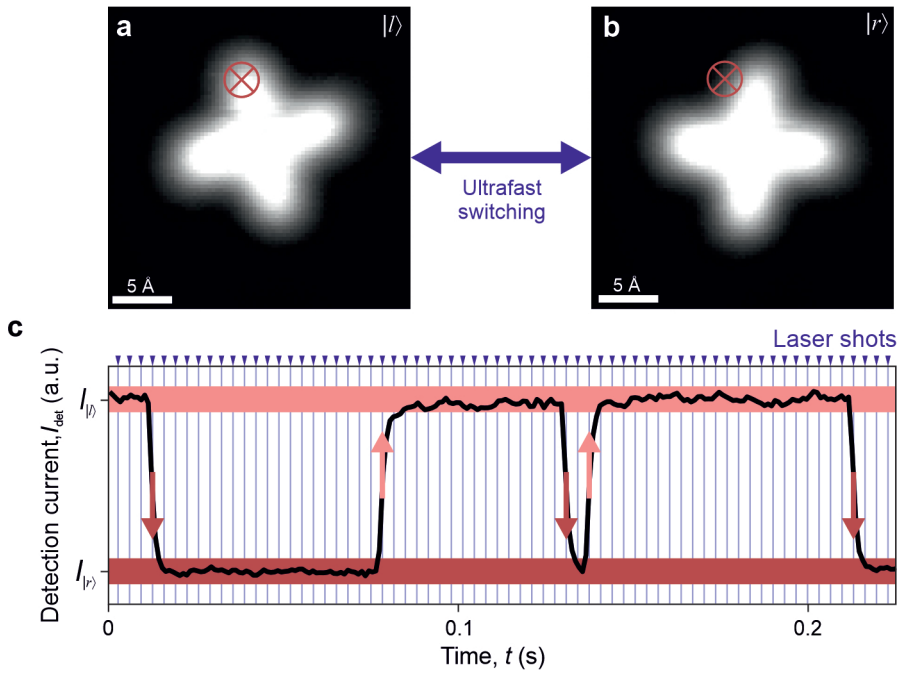

Figure 5.3: Ultrafast action spectroscopy of a single molecule switch. a,**b**, Constant height images of the states $|l\rangle$ (**a**) and $|r\rangle$ (**b**) (bias voltage, 6 mV; linear grey scale, 0 – 1.6 pA). **c**, Characteristic time trace of the non-resonant detection current, I_{det}, while the tip is placed at the position of the crosshair in **a** & **b**. The vertical blue lines mark the instants in time, where an ultrafast THz pulse is applied to the STM junction.

is determined by the feedback loop operating at a current setpoint of 2 pA at a bias voltage of 20 mV (bilayer NaCl, data shown in figures 5.3 and 5.4) or 220 mV (trilayer NaCl, all other shown data), respectively. While qualitative differences for the data acquired on bilayer and trilayer NaCl were not observed, for consistency, all time-resolved data have been recorded on a trilayer of NaCl only. After switching off the feedback loop, the tip is moved laterally at constant height to the desired measurement position above the molecule, where it remains throughout the measurement. Applying a constant bias voltage with typical values around 15 mV (bilayer NaCl) or 150 mV (trilayer NaCl) well below any of the molecular resonances drives a detection current I_{det} of a few pA. As this current is not accompanied by a transient charging of the molecule it does not result in switching events, yet it differs for both adsorption states.

Simultaneously, THz pulses or pairs of pulses with individually tuneable field strengths are coupled into the STM. As a first step, the field strength of the THz pulse is chosen such that the voltage transient can access the LUMO resonance of the molecule. This results in a time window of ∼100 fs for the tunneling of a single electron [20]. In the presented experiments, all lightwave-induced tunneling rates remained below 0.4 electrons per pulse. With certain probability, tunneling injection leads to

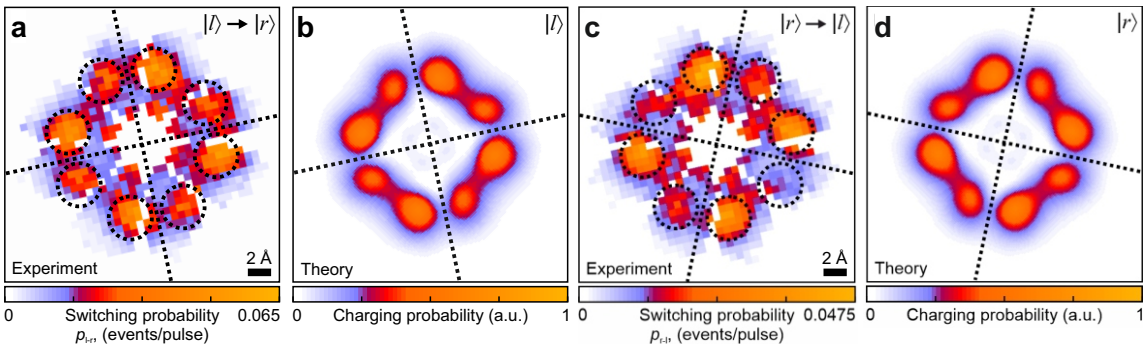

Figure 5.4: Path-selective map of the single-pulse switching probability. Spatial maps of the switching probabilities for both directions, p_{l-r} from $|l\rangle$ to $|r\rangle$ (**a**) and p_{r-l} from $|r\rangle$ to $|l\rangle$ (**c**). Pixels where switching cannot be detected are depicted in white. Eight areas of enhanced switching probability stand out (dashed circles), four of which are more prominent. The axes of the molecule in the initial state are indicated by dashed lines. Simulated charging probabilities by tunneling into a LUMO in state $|l\rangle$ (**b**) and in state $|r\rangle$ (**d**) closely match the experimental switching maps.

a switching event between the two adsorption geometries resulting in a persistent change of the detection current. A characteristic current trace acquired over 0.23 s while repeatedly applying THz pulses is depicted in figure 5.3c. It becomes apparent, that not only each switching event manifests as an abrupt change of the detection current I_{det}, but also that the direction of each switching event can be distinguished (indicated by up and down arrows). When the tip is positioned above the molecule in such a way that the tunneling current differs for $|l\rangle$ and $|r\rangle$ (cross hairs in figures 5.3a & b), we can associate every change in the detection current to the switching from $|l\rangle$ to $|r\rangle$ or vice versa. This allows analyzing the switching behavior for each direction separately.

The finite bandwidth of the STM current preamplifier, however, results in a finite rise time in the observed changes of I_{det}. In order to ensure the detection of every individual switching event, the repetition rate of the laser pulse trains must therefore be adapted to the bandwidth of the STM current preamplifier. Furthermore, since the outcome of every laser shot is governed by quantum probability, resolving the switching statistics with high precision requires the experiments to be repeated numerous times.

This approach allows analyzing every attempt at triggering a switching event, from which the probability per THz pulse $p_{\mathrm{l\text{-}r}}$ to switch from $|l\rangle$ to $|r\rangle$ as well as the probability $p_{\mathrm{r\text{-}l}}$ for the reverse direction can be deduced. These probabilities depend on the precise lateral STM tip position (x, y) where electron injection into the molecule occurs. Recording numerous switching time traces similar to figure 5.3c across the whole molecule, maps of local probabilities $p_{\mathrm{l\text{-}r}}(x, y)$ and $p_{\mathrm{r\text{-}l}}(x, y)$ were obtained, which are shown in figures 5.4a and c. These reveal sub-molecular features

and a distinct direction dependence, and both match to the respective calculated efficiency of local electron injection into the LUMO density of the initial-state configurations, $|l\rangle$ for $p_{\text{l-r}}$ (figure 5.4b) and $|r\rangle$ for $p_{\text{r-l}}$ (figure 5.4d). Both maps feature eight outer lobes and nodal planes along the isoindole units (dashed lines), which reflect the in-plane orientation of the molecule. Moreover, four of the eight lobes are more prominent, which stems from an internal torsion of the molecule as revealed by density functional theory (DFT) calculations. The agreement between the calculated LUMO density map and the measured switching probability map indicates that the switching probability scales linearly with the electron injection efficiency; in other words, the probability that an injected electron triggers a switching event is position-independent. By relating the lightwave-induced current to the switching rate, this probability is estimated to be $21 \pm 3\,\%$. If the amplitude of the THz pulse is lowered by e.g. $25\,\%$, such that the pulse cannot induce tunnelling into the LUMO, the switching probability drops to zero.

5.5 Force-Driven Motion of the Molecular Switch

It can now be demonstrated that the switching probability of the single MgPc molecule can be strongly influenced by an ultrafast force pulse, which induces a coherent, predominantly rotational motion of the molecular frame. To this end, a pump-probe experiment is performed, in which the pump acts as an ultrafast force pulse, whereas a time delayed probe injects an electron into the LUMO to induce single-molecule switching (figure 5.5a). By evaluating the action of every laser shot, the switching probability, $p(\tau)$ as a function of the pump-probe delay time τ was retrieved. The probe pulse is adjusted such that it can trigger the molecule to switch via tunneling an electron into the LUMO, as shown above. The pump pulse, however, is deliberately tuned such that the amplitude of this pulse is below the voltage required for electron injection into the molecule. This is in contrast to the recently reported measurement of single-molecule vertical vibration, which was triggered by deliberately charging the molecule [20]. This underlines, that any structural dynamics observed in this experiment are the result of effects unrelated to charging.

This is demonstrated in figure 5.5b, which shows a typical result from such a pump-probe experiment. The resulting switching probability, p_τ, exhibits a marked oscillation at a frequency of 0.3 THz. This frequency is consistent with that calculated by DFT for the frustrated in-plane-rotation. Given that the switching trajectory is predominantly such a rotation of the molecule, this agreement in frequency suggests that the pump pulse triggers this rotation. As will be corroborated below, this interaction is purely mediated by the electric near field acting as an atomically localized force transient.

A first hint towards this behavior is also demonstrated in figure 5.5, which shows two curves for experiments with opposite pump pulse polarity. It becomes apparent, that reversing the polarity of the pump pulse leads to a phase shift of 180° of the

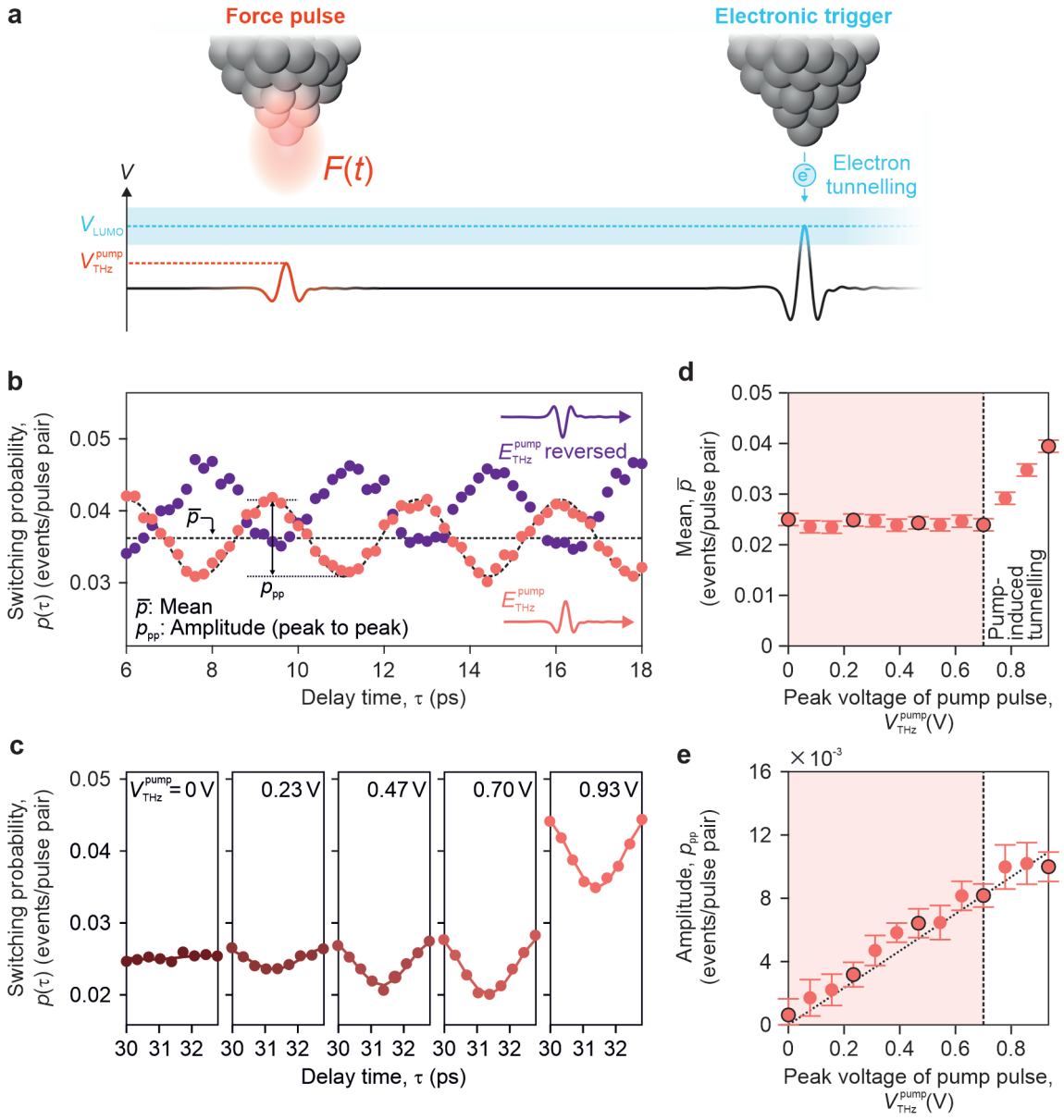

Figure 5.5: Ultrafast force stimuli coherently control the single-molecule switching probability. **a**, Pump-probe scheme with THz pulses with variable delay time τ. The pump pulses (red) are tuned below the threshold of electron tunnelling, whereas the probe pulses serve to inject single electrons and interrogate molecular dynamics via time-delayed switching events. **b**, Switching probability as a function of delay time exhibits a marked oscillation at a frequency of 0.3 THz (red data points, $V_{\mathrm{THz}}^{\mathrm{pump}} = 0.7\,\mathrm{V}$). A reversal of the polarity of the pump pulse coherently inverts the phase of the oscillatory signal (violet data points). **c**, Switching probability over one oscillation period for different pump peak voltages. **d**, Mean $\bar{p}$ and amplitude of the modulation p_{pp}(**e**) of the switching probability for varying pump peak voltages.

observed oscillation. This is attributed to an acceleration of the molecule in the opposite direction, resulting in the observed phase shift of the oscillation of the switching probability, which hints towards the electric field of the pulse indeed acting as a force transient.

To verify this hypothesis, the pump field strength and hence the transient voltage applied across the tunneling junction, $V_{\mathrm{THz}}^{\mathrm{pump}}$, is varied from below to above the threshold for electron injection into the LUMO while keeping the amplitude of the probe pulse constant. Five typical p_τ-traces are shown in figure 5.5c, recording the switching probability over one oscillation period. Starting from the absence of a pump pulse ($V_{\mathrm{THz}}^{\mathrm{pump}} = 0\,\mathrm{V}$), which displays only a constant, flat switching probability stemming from the switching events triggered by the probe pulse, a more marked oscillation begins to manifest when increasing the pump pulse voltage. For high enough pump fields, i.e. $0.93\,\mathrm{V}$, the pump pulse can also induce charging of the molecule, and, subsequently, trigger a switching event. This however, only causes an offset of $p(\tau)$, which is independent of the delay between pump and probe pulse.

So in summary, the pump pulse has two distinct effects on the switching dynamics: (i) It induces a marked modulation of p_τ and (ii) adds a delay-independent positive offset. These two components scale quite differently as a function of $V_{\mathrm{THz}}^{\mathrm{pump}}$ (figures 5.5d and e). The mean, $\bar{p}$, (figure 5.5d) remains flat for weak pump fields but increases steeply once $V_{\mathrm{THz}}^{\mathrm{pump}}$ exceeds the voltage required to induce electron tunneling into the LUMO. This agrees with the aforementioned observations made for figure 5.5c, where the switching probability rises independent of the delay time τ. Thus, the steep increase of $\bar{p}$ can be unequivocally attributed to switching events triggered by electron tunnelling induced by the pump pulse. Conversely, for weak pump fields only the probe pulse triggers electron tunneling, which leads to the constant mean of $\bar{p} \approx 0.025$. In sharp contrast, the amplitude (figure 5.5e) of the coherent modulation in the switching probability, p_{pp}, increases linearly with the pump field, starting from zero, over the entire field range. Even pump pulses that are too weak to induce electron tunneling into the LUMO strongly influence the switching probability of the probe pulse.

From this behavior it is concluded, that the electric field of the pump pulse causes a coherent oscillation of the system, which in turn results in the experimentally observed linear dependence of the modulation p_{pp}, on the voltage of the pump pulse $V_{\mathrm{THz}}^{\mathrm{pump}}$. These results show, that pump pulses below the tunneling threshold can induce a coherent motion of the system, which is caused solely by the electric-field of an ultrafast THz pulse, which in turn influences the probability to switch the molecule after electron injection. This means, that the electric field of the pump pulse directly exerts a force, either on atoms carrying a net charge, or via a polarization of each atom due to the inhomogeneity of the field. Either way, the electric field of the pulse leads to an ultrafast force transient acting locally.

In order to test how local these forces are exactly, pump-probe experiments at varying tip positions across the whole molecule were performed. For these experiments, the pump fields were kept below the tunneling threshold. These datasets

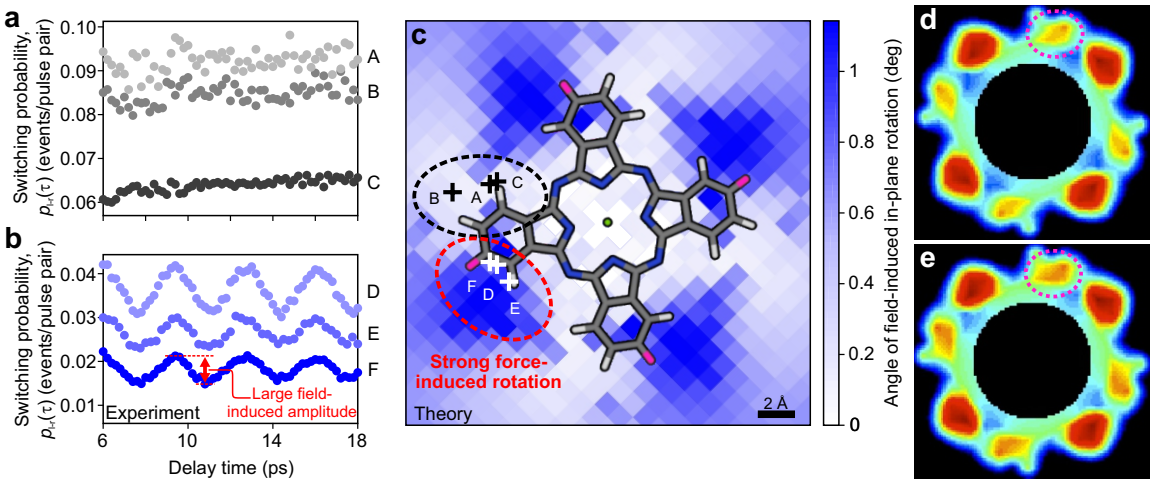

Figure 5.6: Atomic spatial selectivity of the femtosecond force stimulus. a, **b**, Time-resolved switching probability at different tip positions (indicated by labeled crosses in **c**). **c**, Color map illustrating how a local out-of-plane electric field centred at different locations (pixel coordinates) acts as an atomic-scale force and induces an in-plane rotation of the MgPc molecule of different amplitude (colour bar), as computed by DFT calculations. A top view of the calculated geometry of the molecule without applied field is overlaid with select hydrogen atoms highlighted in pink. **d**, **e**, Experimental switching probability maps for delay times, where the modulation of p_{pp} is minimal (**d**) or maximal (**e**). The dashed pink circle highlights an area where large modulation is observed.

reveal the local force applied to the molecule, which is shown in figures 5.6a and b. It becomes apparent, that not only the mean switching rate, $\bar{p}$, and the modulation amplitude, p_{pp}, do critically depend on the position of the tip, but also that there are regions of distinctively different behavior. We find local regions where – less than 5 Å apart – the force-induced modulation, p_{pp}, is either absent (figure 5.6a) or maximized (figure 5.6b). This strong dependence of p_{pp} on the exact position, where the force is applied, confirms that the force transient indeed acts locally, confined to the Ångström scale. Conversely, $\bar{p}$ is determined by the mean efficiency of the probe pulse to trigger a switching event, following the LUMO tunnelling probability similar to figure 5.4. Regions where $\bar{p}$ is large but p_{pp} is absent (figure 5.6a) were observed, and others where $\bar{p}$ is moderate but p_{pp} is maximized (figure 5.6b), confirming that the local force acts independently of electronic excitation.

These observations are further confirmed by recording the switching probability across the molecule for different delay times τ. Maps of the switching probability for two specific delay times are shown in figure 5.6, specifically where the modulation is minimal (figure 5.6d) and where it is maximal (figure 5.6e). At first glance, these maps indeed appear similar to the ones shown in figure 5.4, confirming that, overall, the switching probability is still governed by the LUMO tunnelling efficiency. Comparing the two maps, however, one finds specific areas, where the switching probability is

modulated by the applied force pulse (dashed circles in figures 5.6d and e). This fact further underlines the local action of the ultrafast force transient on the molecule.

The electric THz near field in the STM junction is expected to be oriented predominantly perpendicular to the surface, as the metal substrate efficiently screens any in-plane component. This fact, however, does not match with the expectation, that the modulation of the switching probability is predominantly caused by an in-plane frustrated rotation of the molecular frame. To this end, density functional theory (DFT) calculations were performed, in which the geometry of the combined system of molecule and NaCl layer is relaxed. Figure 5.6c shows a top view of the molecule in state $|l\rangle$ with no field applied. Including a local, out-of-plane electric field in the calculations to simulate the effect of the pump pulse onto the molecule reveals, that the molecule can undergo small azimuthal excursions, which depend on the exact position of the applied field. This is realized in the DFT calculations by including a pair of point charges, which are located above and below the molecule in order to simulate a locally applied field. The results of these calculations are shown in the color-coded background image of figure 5.6c and show areas of qualitatively different behavior on a sub-molecular scale. The areas, where also a large modulation of p_{pp} was found experimentally, coincide with the areas where DFT predicts a large azimuthal excursion of the molecule when applying a perpendicular electric field (figure 5.6b). The calculations also suggest, that this behavior might be due to the specific arrangement of substrate and atomic positions within the molecule. The relaxed geometry of the molecule hints towards the azimuthal energetics being dominated by the interaction of specific hydrogen atoms (marked in pink in figure 5.6c) with the underlying chlorine and sodium atoms of the substrate, which gives rise to the double-well energy landscape.

Figure 5.6c strikingly illustrates that, according to the calculation, local fields applied at these atoms induce an appreciable rotation, whereas fields applied elsewhere hardly do. These rotations are too small to directly induce switching of the orientation consistent with the experimental observation that without electron injection no switching is observed. However, ultrafast electric fields could be utilized as a trigger for an in-plane frustrated rotation. This provides a tool to selectively modulate the switching probability of a later probe pulse and thus allow for coherent control of the molecular switch. The calculated pattern of the local efficiency of a rotational excitation agrees very well with the experimentally observed variations of the modulation amplitude of p_τ (figures 5.6a and b).

5.6 Summary & Outlook

In this chapter we have demonstrated that we can use the electric field of a THz laser pulse to directly exert ultrafast forces on select atoms within a molecular switch. These forces allowed us to directly influence the probability of triggering the switch, thus establishing coherent control over the movement of the molecule. In particular,

the following was demonstrated:

- As a first step, we reproduced the behavior of magnesium phthalocyanine (MgPc) found in previous studies, specifically that it adsorbs in a bistable geometry when deposited onto ultrathin NaCl on Cu(111) [103]. In this configuration, MgPc can be switched between the two stable geometries by charging and thus acts as a single molecule switch.
- We then showed that it is possible to cause switching events of the molecule via charging through the implementation of ultrafast THz laser pulses. In order to characterize the switching behavior caused by these pulses, we utilized ultrafast action spectroscopy, which allowed us to monitor every individual switching event of the molecule. By applying a small, in-gap bias voltage, we can monitor the adsorption geometry in a non-invasive manner, which allows us to directly assess the effects of the THz laser pulses.
- Analyzing the switching behavior triggered by electron injection into the LUMO via THz pulses, we find that the observed map of the switching probability matches the calculated map for the electron injection probability into LUMO. This corroborates, that charging is the dominant process responsible for switching the molecule.
- In a set of pump probe experiments, we found that the switching probability can be influenced by first exerting a force on the molecule. This force is solely caused by the electric field of a THz pulse, which is adjusted such that no electron injection into the LUMO is possible. The switching probability is modulated by a coherent oscillation of approximately 0.3 THz, which corresponds to the frequency of the frustrated, in-plane rotational motion of the molecule. In order to unambiguously prove that this behavior is caused by an ultrafast force transient, we analyzed the switching probability for different pump voltages as well as different polarities of the pump pulse.
- In a final step, we analyzed the spatial extent of these forces. Experimentally, we found, that in spatially and temporally resolved maps of the switching probabilities, distinct areas can be identified, where the force transient causes a modulation of the switching probability, and where it is not changed by the application of an initial force. This observation is corroborated by DFT calculations, which show, that the application of a electric field leads to an azimuthal excursion of the molecule, causing an in-plane frustrated rotation. These calculations also suggest, that the adsorption geometry of the molecule is dominated by the interactions of a few select atoms of the molecule with the underlying NaCl substrate. The positions of these correspond to the areas where the largest influence of the force on the switching probability is observed experimentally.

The ultrafast coherent atomic manipulation demonstrated here lays the groundwork for a multitude of future applications. Being able to trace reactions of various kinds in space and time simultaneously and also influence and control them at the same time opens new approaches for a plethora of systems. For example, combining

this technique with recently developed methods for probing ultrafast forces [152, 153] may pave the way to lightwave force microscopy with sub-molecular resolution.

Applying the presented techniques to different molecular systems might reveal new approaches in the study of chemical reactions. Ultrafast force transients could in this case be used steer and manipulate the dynamics of reactions like bond breaking and formation, while also resolving these processes in real time and on the intrinsic length scales of single molecules.

We also envisage extending these techniques to other systems and processes, for example phase transitions in strongly correlated materials [154] or the quantum properties of bio-molecular systems [155].

But not only can one imagine the technique developed in this chapter be applied to other systems, one can also use the present system to study the effects of the laser in the tunneling junction. Since the molecular switch provides a well-defined resonance, it can be utilized as a voltage standard in order to gauge the near field of the THz pulse in the tunnelling junction. These experiments were already performed and published in *Nature Photonics* [81], but will not be discussed in the scope of this thesis.

6 Photoinduced Toggling Motion of a Single Molecule

The results presented in this chapter have been obtained and interpreted in collaboration with Tzu-Chao Hung, Andreas Rank and Jascha Repp. The results presented in this chapter provide a preliminary interpretation of the experimental observations.

In this chapter, results on the photoinduced switching of a single molecule are presented. We found that upon optical excitation a single magnesium phthalocynanine (MgPc) molecule can be switched between two stable adsorption geometries on ultrathin film NaCl on Cu(111). This excitation is facilitated by coupling a laser to the junction of a scanning probe microscope, where the excitation energy matches the optical gap of the single molecule.

In order to explore the exact mechanisms governing this process, we developed a novel technique, which enables the excitation of the molecule. By synchronizing a pulsed laser to the oscillation of an atomic force microscope (AFM), we can control at which instants in time the excitation occurs and thus explore a new approach to studying the photoinduced motion of single molecules.

We gauge these capabilities by resonantly exciting a single MgPc molecule, which is known to toggle between two stable adsorption geometries upon charging [103], deposited onto ultrathin NaCl on Cu(111). Synchronizing laser pulses to the AFM operating with a large oscillation amplitude, we can deliberately excite the molecule with or without the tip being in close proximity to the molecule to controllably tune the charging probability. This provides a novel access to classify the possible mechanism for this molecular motion for different tip-molecule displacements. The data presented in this chapter suggests, that the mechanical motion of the molecule is triggered by a transient charge state involved in the nonradiative relaxation of the molecule.

6.1 Introduction

A fundamental understanding and precise control of molecular movement at the nanoscale is of great importance in the fields of biology, chemistry and physics. To this end, the study of molecular motors has garnered increasing attention in recent years [156–158]. These nano machines can be specifically tailored to translate an external excitation into an internal motion of the molecule. With the help of state-of-the-art STM, molecular motors can be excited with sub-nanometer precision and their movement can be directly traced. In recent years, a wide array of molecular motors has been studied in this environment. The motion of these motors could, for example, be induced by the direct manipulation with the STM tip [159, 160], voltage pulses [161], thermal activation [162–164] or inelastic excitation [165].

With the rapid progress of optics-based STM techniques, a novel approach to the study of molecular motion was established. With tip-enhanced Raman spectroscopy (TERS; see section 2.4), for example, it was possible to resolve vibrations with sub-molecular resolution [19]. The motion of a single molecule could be traced in space and time using lightwave-driven STM [20]. Light-induced translations of molecules [166] or conformational transitions by selectively exciting molecular vibrations [73] were also achieved by optical excitation of an STM junction.

One specific molecular motion, which will be under further investigation in this chapter, is the switching of a molecule between two stable adsorption geometries, specifically magnesium phthalocyanine (MgPc) on ultrathin NaCl grown on Cu(111). The motion of this system can be caused by charging the molecule [103] and can be influenced by ultrafast forces mediated by an electric field transient [80] (see chapter 5). Furthermore, the motion of this molecular switch can also be induced via inelastic electron tunneling [167]. Very recently, it has been shown that this toggling motion can also be remotely excited via a nanocavity plasmon [42]. The exact mechanism, which leads to molecular motion in this case, has thus far remained unclear.

In this chapter, we want to investigate the toggling motion of a single MgPc molecule with a new approach. To this end, we developed a novel method which is based on the direct photoexcitation of the molecule. This is achieved by implementing a triggered nanosecond pulsed laser (NPL), which is synchronized with the oscillation of an atomic force microscope (AFM) cantilever. Due to the pulsed nature of the laser, the average power coupled to the junction is reduced compared to continuous wave (CW) operation. Simultaneously, the synchronization of the laser pulses with the cantilever oscillation enables new possibilities for the investigation of photoexcitation with versatile experimental options. After describing the implementation of this technique, an overview of the arising challenges is presented and discussed. Finally, this scheme is used to trigger and analyze the toggling motion of an MgPc molecule between its two stable adsorption geometries. Our data suggests, that the switching of this molecule between its two stable geometries is facilitated by photoexcitation, which causes a transient charging of the molecule in a nonradiative relaxation process.

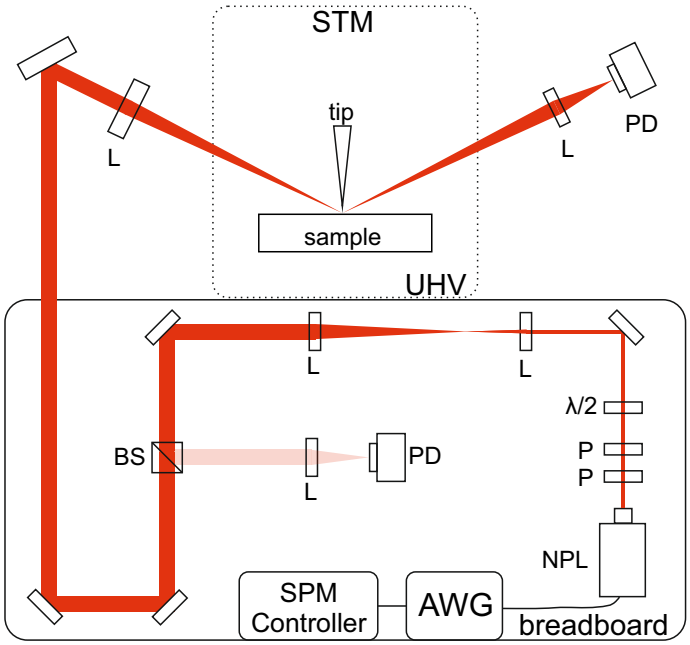

Figure 6.1: Sketch of the laser setup. The laser setup used in this experiment consists of two parts. One part is fixed on a breadboard, which is mounted to the frame of the microscope. The other part is rigidly connected to the UHV chamber of the system. Legend: AWG: arbitrary waveform generator; NPL: nanosecond pulsed laser; P: polarizer; $\lambda/2$: wave plate; L: lens; BS: beam splitter; PD: photodiode.

6.2 Laser Setup & Alignment

As a first step, the experimental implementation of the laser system is schematically shown in figure 6.1. The laser used in this case is a nanosecond pulsed laser (NPL; NPL64C, Thorlabs) with a center wavelength of 640 nm. The laser pulses are triggered externally via an arbitrary waveform generator (AWG), which is the main tool used to synchronize the laser pulses to the AFM cantilever oscillation (see later in this chapter). Following the laser source, two polarizers are implemented, where the first one is rotable. Since the output of the NPL is linearly polarized in the horizontal direction, the pair of polarizers can be used to adjust the power coupled to the SPM junction.

After these two polarizers, a $\lambda/2$ wave plate is positioned, which can be used to rotate the polarization of the laser. Since the field enhancement in the tip-sample junction is polarization dependent, adjusting the polarization to be parallel with the SPM tip is crucial for a sufficient field enhancement in the junction [168], which will in the end lead to an enhanced signal observed in the experiment. Following the wave plate, the laser beam is widened and recollimated using a set of two lenses. The resulting beam diameter of approximately 15 mm leads to a higher numerical aperture when focusing the laser to the tip, which will in turn lead to a smaller focus

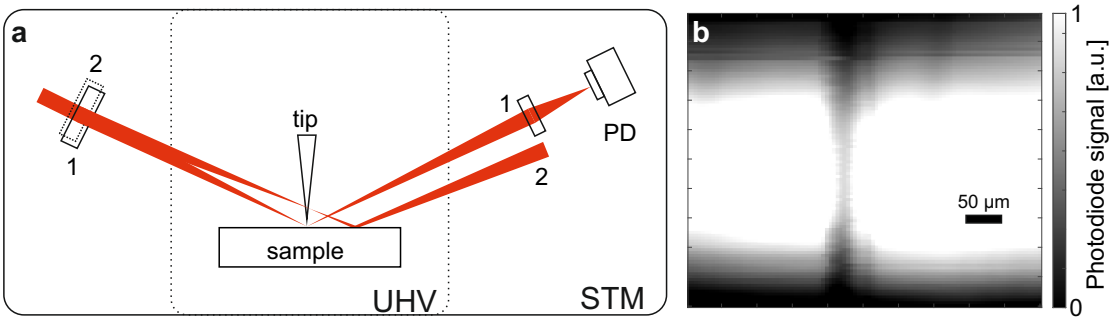

Figure 6.2: Laser alignment. **a**, Sketch of the laser alignment, where two different configurations of the lens are shown. **b**, Typical measured photodiode signal, where an image of the tip and its reflection is visible. The scale bar indicates 50 μm displacement of the focusing lens.

spot and thus sufficient laser power in the junction.

A 90:10 beam splitter is introduced to the beam path, where 90 % of the power is guided to the STM chamber, while 10 % of the power is diverted to a photodiode located on the breadboard. This diode is used to monitor the the timing of the laser pulses. Since the phase not only between the AFM oscillation and the laser pulses is essential, but also the periodicity of the pulse train, this photodiode is crucial for later operation.

Finally, the beam path leaves the breadboard and is guided to the STM chamber. There, the mirror used to deflect the beam towards the tip-sample junction as well as the lens used for focusing are rigidly mounted to the UHV chamber. This is done to prevent any motion of the focusing optics with respect to the tip and sample. Since already minuscule vibrations can cause significant power fluctuations and thus thermal drifts, the fixation of these optical elements to the UHV chamber is necessary.

The final lens used to focus the laser onto the tip sample junction is mounted to a motorized 3-axis stage. This can be used to precisely move the lens and thus adjust the beam to be properly focused onto the tip-sample junction. This method of laser alignment has already been proven successful in other research (see ref. [169]). After entering the UHV chamber through a view port, the laser beam is reflected from the metallic sample and escapes the UHV chamber. Here, the beam is focused onto another photodiode, which is used for laser alignment and monitoring of the overall laser power.

The alignment of the laser to the tip-sample junction is depicted in figure 6.2. Figure 6.2a shows a sketch of the alignment process, where two different positions of the focusing lens are indicated. In this case, lens position 1 shows a proper alignment to the junction. This will result in a large signal at the photodiode, since the laser is fully hitting the sensor. However, if the laser properly hits the tip, the shadowing will reduce the power arriving at the photodiode. For position 2, most of the laser will in the end not hit the photodiode, which means that the signal in this case is

significantly reduced.

Since the lens used for alignment is mounted to a motorized 3-axis stage, it can be utilized to optimize the position of the laser focus with respect to the tip-sample junction. To this end, the lens is scanned in the two dimensions perpendicular to the beam path, while the signal at the photodiode is recorded. An image of the resulting photodiode signal is depicted in figure 6.2b. While the top and bottom appear dark due to the laser not properly hitting the diode, a contour of the tip shadow can be clearly seen in the center of the image. This contour is mirror symmetric, since both the actual tip as well as its reflection in the metallic sample are visible. The photodiode signal, however, is not the only quantity, which can be used for laser alignment. Another possibility is to utilize the STM topography, which also changes when the laser is properly focused onto the tip. Since the laser is introducing heat into the system, the STM tip expands thermally. While operating the STM in constant current mode, the feedback will compensate this thermal expansion and retract the tip. This change of tip height can similarly be monitored while moving the lens and also yield information about the proper alignment of the laser.

With these methods it is ensured, that the laser properly hits the junction and thus a molecule located directly under the tip can be excited with sufficient efficiency. In order to ensure the stability of the experiments, the photodiode signal is recorded during all measurements. This way, any change in the incident laser power can be detected and proper conditions for the experiments can be maintained.

6.3 Laser Pulse Synchronization with the Cantilever Oscillation

One of the major advantages of the technique presented in this chapter is the employment of laser pulses on the nanosecond timescale. Due to this modulation of the laser intensity, the aforementioned heating problems usually arising in laser-assisted SPM can be significantly reduced compared to CW operation. In the experiments presented later, two laser pulses with a duration of $\approx 150\,\mathrm{ns}$ are coupled to the SPM junction per cantilever oscillation. Since the resonance frequency of the cantilever used in this experiment is 28.54 kHz, the period of the cantilever is approximately $35\,\mu\mathrm{s}$, which results in an on-off ratio of $\approx 1 : 117$ for the laser. Due to this low ratio, the power during the pulse can be comparatively high, while still maintaining a rather low average laser power and thus reduced heating of the tip-sample junction.

Experimentally, this synchronization is achieved via the arbitrary waveform generator (AWG) controlling the laser. While this provides the electronic trigger pulses for the NPL, defining at which times laser pulses are emitted, it is itself triggered by the AFM feedback electronics. With the AWG one can now control the delay (or, equivalently, phase) between the AFM trigger pulse supplied to the AWG and the laser trigger pulses controlling the emission of the NPL. This way, the synchronization

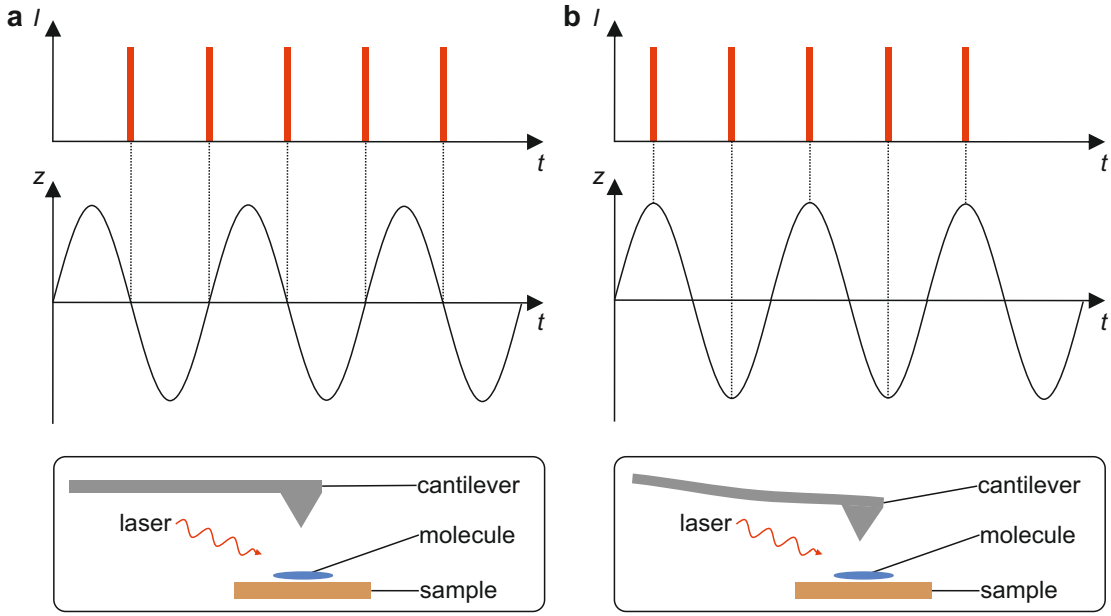

Figure 6.3: Synchronizing laser pulses to the AFM oscillation. Schematics of the coupling of laser pulses to the AFM oscillation. Two extreme cases are shown here, namely where the laser pulses occur at the zero crossing of the AFM oscillation (tip far away from the molecule; **a**) and at the turnaround points of the oscillation (tip close to the molecule; **b**).

of AFM oscillation and laser pulses can be experimentally realized.

Before going into details on which impact the exact phase between cantilever oscillation and laser pulses has, the feedback mechanisms have to be discussed. Since these experiments are performed in a combined STM/AFM setup (see chapter 4.1), the cantilever oscillation can be operated via the AFM controller, while the tip height can be controlled by the constant-current STM feedback loop (see also section 3.1). Due to the exponential decrease of the tunneling current with an increasing gap size, the current detected predominantly stems from electrons tunneling at the bottom turning point of the cantilever oscillation when its amplitude is sufficiently large [170]. This modulation of the current is not visible due to the finite bandwidth of the current preamplifier.

Since the laser pulses only have a short duration of 150 ns, the timing of these pulses is of utmost importance. The main novelty of the technique presented here lies in the synchronization of these pulses with the AFM cantilever motion. For example, one possible configuration is to couple the laser pulses to the junction, when the cantilever is crossing through its resting position (zero crossing; ZC; figure 6.3a). For experiments on single molecules this implies, that the laser pulses occur at instants in time, where the tip is far away from the molecule, where no electron tunneling occurs from the tip to the sample. Similarly, the laser pulses can be adjusted to be coupled to the junction, when the cantilever is at the turning points of the oscillation

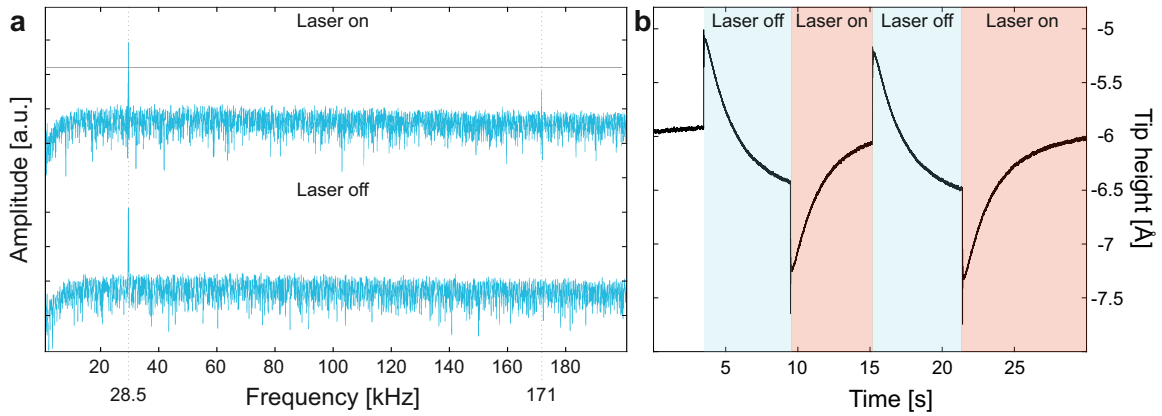

Figure 6.4: Excitation of the second flexural mode of the cantilever. **a**, Spectrum of the AFM oscillation signal with laser off and laser on. During full power laser illumination, a peak appears at 171 kHz due to the excitation of the flexural mode of the cantilever. **b**, Tip height changes during laser switching on (red areas) and off (blue areas). A sharp jump appears followed by a slower thermalization process. AFM amplitude: 10 Å; setpoint: 50 mV, 2 pA. Continuous wave (CW) laser power for both graphs: 8.5 mW.

cycle (figure 6.3b). This results in the excitation happening at times where the tip is in close proximity to the molecule. Since the laser can also be adjusted to every point in time between these two extreme cases, the change in phase between pulses and AFM oscillation can be directly connected to a change in tip-molecule distance, at which excitation occurs. This is in contrast to recent STM-based techniques, which rely on the tip being in tunneling contact, which is necessary to facilitate photocurrent measurement [56, 76]. However, since the tunneling current decreases exponentially with distance, only experiments where the tip is in very close proximity to the molecule can be performed with these techniques.

Another important point is to avoid the excitation of the cantilever simply by coupling laser pulses to the junction. This is achieved by employing two laser pulses per cantilever oscillation cycle, which results in an unperturbed fundamental oscillation of the cantilever. This behavior is similar to the effects in other experiments, as presented in ref. [99].

6.4 Cantilever Excitation & Heating Effects

Before benchmarking this technique for the investigation of single molecules, the effects of the laser pulses on the SPM operation itself are analyzed. This way it can be ensured, that the results obtained with this technique are indeed effects originating from the interaction between laser and molecule and are not due to artifacts in the measurement itself.

The first phenomenon to be discussed here is the excitation of the cantilever due to the laser. As stated earlier, the excitation of the fundamental oscillation of the cantilever is avoided by introducing two pulses per cycle to the tip-sample junction. This, however, does not rule out the excitation of higher order modes of the cantilever. To examine this, the spectrum of the AFM oscillation signal while it was operating in frequency modulation (FM) mode is recorded. This way, the amplitude of the fundamental mode is kept constant by the feedback electronics. As can be seen in figure 6.4a, the spectrum exhibits an additional peak at approximately 171 kHz while the laser is on. This peak reproducibly vanishes and reappears when the laser is switched on and off.

This peak is attributed to the excitation of the second flexural mode of the cantilever. This mode usually has a frequency of $\omega \approx 6\omega_0$, where ω_0 is the frequency of the first order cantilever oscillation. This was also found in different experiments, in which these higher order modes are used for AFM imaging [171, 172]. As can also be seen in figure 6.4a, the frequency of the additional peak closely matches six times the frequency of the fundamental oscillation at 28.5 kHz.

In order to assess the effects of this second flexural mode in an experimental setting, the behavior of the tip while switching the laser on and off is directly monitored. To achieve this, the AFM is operated in FM mode with a constant amplitude of 10 Å while the STM feedback was engaged (setpoint: 50 mV, 2 pA) and monitored the tip height. The results of this are shown in figure 6.4b. The data exhibits two distinct features. The first observation entails, that the tip height suddenly jumps when the laser is switched on or off. More specifically, the tip retracts when the laser is coupled to the junction (red areas) and moves closer to the sample when the laser is switched off (blue areas). These sharp changes in the tip height are attributed to the excitation of the second flexural mode.

Our current interpretation is that this additional mode excited by the laser affects the tip position at bottom turning point of the cantilever oscillation, which results in an overall smaller tip-sample distance. This in turn leads to higher tunneling currents to which the feedback electronics react, culminating in the observed retraction of the tip when the laser is switched on and the approach of the tip when no laser radiation is coupled to the tip. This interpretation is further supported by the fact, that the additional 171 kHz peak in the spectrum shown in figure 6.4a vanishes at the same timescale as the sharp jumps in tip height shown in figure 6.4b occur, suggesting that these two observations are indeed connected. While this second flexural mode might be a source of errors for later experiments, it can be avoided by decreasing the incident laser power (see also figure 6.5a, where no sudden jumps are present).

The second observation from figure 6.4b is the comparatively slow adjustment of the tip height following the initial sharp increase discussed above. This is attributed to the slow thermalization of the tip-sample junction which is caused by the laser heating the junction (red areas) or the junction cooling down after the laser was switched off (blue areas). This is also similar to the behavior recorded in other experiments, see for example ref. [76]. In the presented data it appears counterintuitive, that, for

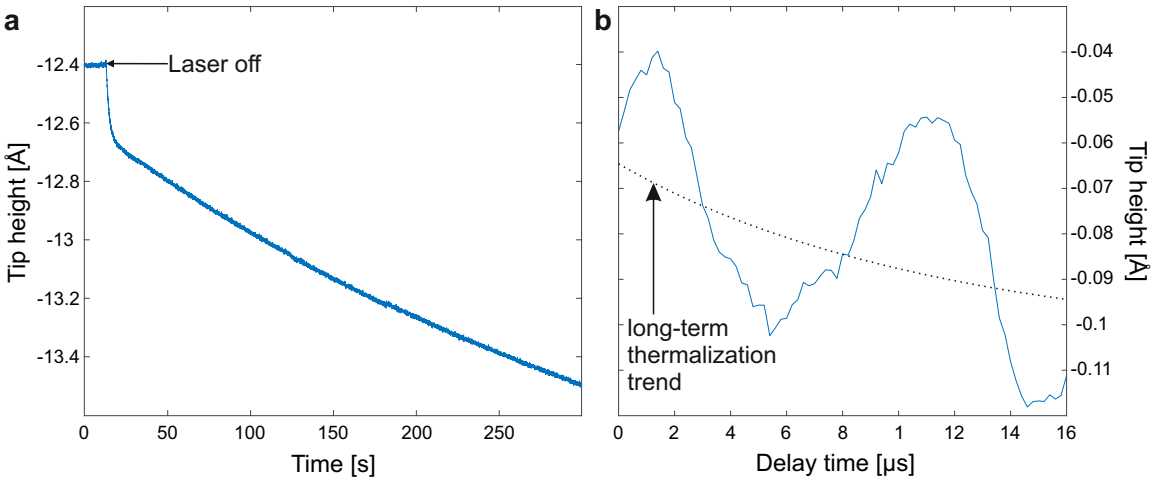

Figure 6.5: Thermalization effects upon laser irradiation. **a**, Long term tip thermalization effects. Thermal equilibrium is only reached after a long waiting period. Setpoint: 50 mV, 2 pA. **b**, Tip height changes while changing the phase between AFM oscillation and laser pulses. The tip height only exhibits small changes when the laser is hitting the tip at the bottom turning points compared to the zero crossing of the oscillation. Setpoint: 50 mV, 5.5 pA; Integration time per data point: 2 s; AFM amplitude: 5 Å. CW Laser power for both graphs: 2.43 mW.

example, the tip approaches the sample when the laser is switched on, while one would expect it to retract. Since the laser is expected to heat the tip, it would lead to a thermal expansion of the tip. This expansion would reduce the tip-sample distance and thus lead to larger tunneling currents and the feedback retracting the tip. It was found, however, that this is dependent on the exact alignment of the laser to the tip and also situations can be prepared, where the tip retracts when the laser is switched on (see figure 6.5b, where long term expansion is still visible). The dataset shown in figure 6.4b was chosen, since there the effects of second flexural mode excitation and heating are distinguished more easily.

This long term thermalization effect is also depicted in figure 6.5a. Here, a time trace of the tip height is shown which reveals, that the thermalization of the junction can take up to a few hours, depending on the incident laser powers. Comparing this graph to figure 6.4b, it becomes apparent, that the initial jump in tip height due to the second flexural mode excitation is not present in this dataset. This is due to the reduced incident laser power used here. Due to the long thermalization times, experiments shown in the later parts of this chapter were only performed after waiting a minimum of three hours in order to avoid artifacts in the observed data.

While the effects of the excitation of the second flexural mode and the long term thermalization of the junction can be avoided, there might also be another, short term heating effect, which could perturb later measurements. Since a pulsed laser is being used in this setup, the average power is comparatively low. However, one

could expect, that during the pulses the tip quickly expands and retracts again. Since the pulses only have a duration of 150 ns, the feedback electronics would be too slow to detect these tip height changes in a setting as described above. To exclude these short term heating effects, the capabilities of the pulse synchronization with the AFM oscillation are used. As discussed earlier, while operating the AFM in constant current mode, the tunneling of electrons predominantly takes place at the bottom turning point of the cantilever oscillation. This behavior can be used to determine if short term heating effects are present. If the laser pulses are set to occur at the bottom turning point, one would expect a significant change in the tunneling current due to short term heating effects, since the current predominantly arises from electrons tunneling at these times. If the AFM amplitude is large enough, however, setting the laser pulses to occur at the zero crossing of the oscillation, one would expect no change in the current due to heating effects.

To examine this behavior experimentally, the tip height is monitored with the STM feedback loop closed, while simultaneously changing the phase between AFM oscillation and laser pulses, the result of which is shown in figure 6.5b. Here, the tip height is shown as a function of the delay time of the laser trigger with respect to the AFM trigger from 0 to 16 μs. Since for every delay time two pulses are coupled to the junction, which are separated by 17 μs (i.e. half a period of the cantilever), changing the delay from 0 to 16 μs corresponds to a sweep of almost a full period of the cantilever oscillation. While there is a slight modulation of the tip height of approximately 0.05 Å, there is no evidence for a significant influence of short term heating effects. Furthermore, the tip is slightly retracting over the course of the measurement due to remaining long term thermalization effects after the laser is switched on. This is due to the different alignment of the laser compared to the figure 6.5b, which corroborates the statement above, that the direction of tip movement while thermalizing is dependent on the alignment of the laser.

In summary, this method of laser coupling to an SPM junction is subject to two major perturbing effects, namely the excitation of the second flexural mode of the cantilever and long term thermalization effect. However, both of these can be mitigated by a suitable choice of experimental parameters.

6.5 Sample Preparation & Methods

In order to perform experiments on single molecules, a Cu(111) single crystal with multiple layers of insulating NaCl evaporated on top of the metallic substrate was prepared. The metal substrate was cleaned via multiple cycles of neon ion sputtering and thermal annealing to 550 °C, where this temperature was reduced to 500 °C after the final sputtering cycle.

NaCl was evaporated from a crucible onto the sample. During this evaporation, the temperature of the sample was kept around 0 °C.

After transferring the sample into the STM, magnesium phthalocyanine molecules

were evaporated onto the cold sample ($T < 10\,\mathrm{K}$) via flash evaporation from a silicon wafer.

All of the experiments described in this chapter were performed using the combined STM/AFM setup shown in chapter 4.1.

6.6 Magnesium Phthalocyanine on NaCl/Cu(111): An Optically Triggered Single-Molecule Switch

Now that the stability of the experimental setup is ensured, the implementation of laser pulses synchronized with the oscillation of an AFM cantilever will be benchmarked using a well-studied molecule as a testing platform: magnesium phthalocyanine (MgPc). As already discussed in chapter 5, it has been studied in various STM experiments [38, 145, 146]. Phthalocyanine molecules in general are a very common choice for the study of excited states, especially in STML experiments [39, 41, 42, 46, 49–51, 53, 54]. Here, this novel technique is tested on these well-known molecules, which allows us to further investigate the processes governing the photoinduced toggling of the molecule.

Here, one property of these molecules is specifically focused on: MgPc can, when deposited onto thin films of NaCl on Cu(111), adsorb in a bistable configuration, which was discussed thoroughly in chapter 5. While the molecule can be switched between its two stable configurations via charging [80, 103], recent research also hints towards the excitation of this molecular motion via coupling to plasmons [42]. With this novel technique, the behavior of this system under resonant photoexcitation shall be examined. To this end, the photon energy of the laser (1.94 eV) used in this case roughly matches the MgPc optical gap (1.89 eV) [38]. Although the energy of the laser photons is slightly higher than the optical gap of MgPc, it should still be possible to excite the molecule via vibrational satellites [75].

In order to assess, if the laser can indeed excite molecular motion, a single MgPc molecule on two monolayers of NaCl is investigated, which has adsorbed in a bistable geometry. This is visible in figure 6.6, where DC-STM images are shown, in which the left-rotated (figure 6.6a) and right-rotated (figure 6.6b) geometries are visible while scanning with in-gap voltages. Upon changing the bias voltage to $-1.9\,\mathrm{V}$, the HOMO of the molecule becomes accessible and the characteristic orbital contrast is reflected in the image (figure 6.6c). Similar to figure 5.1a, a doubling of the nodal planes of the molecular orbital results from the rapid toggling between the two stable adsorption geometries. The most interesting observation is shown in figure 6.6d, which displays an image taken with the same experimental parameters as figures 6.6a and b under laser illumination. Here, telegraph noise becomes visible around the outer edges of the molecule, which is indicative of a switching of the molecule between the two stable adsorption geometries. By placing the tip over one of the arms of the molecule (green dot in figures 6.6a and b) and recording the tunneling

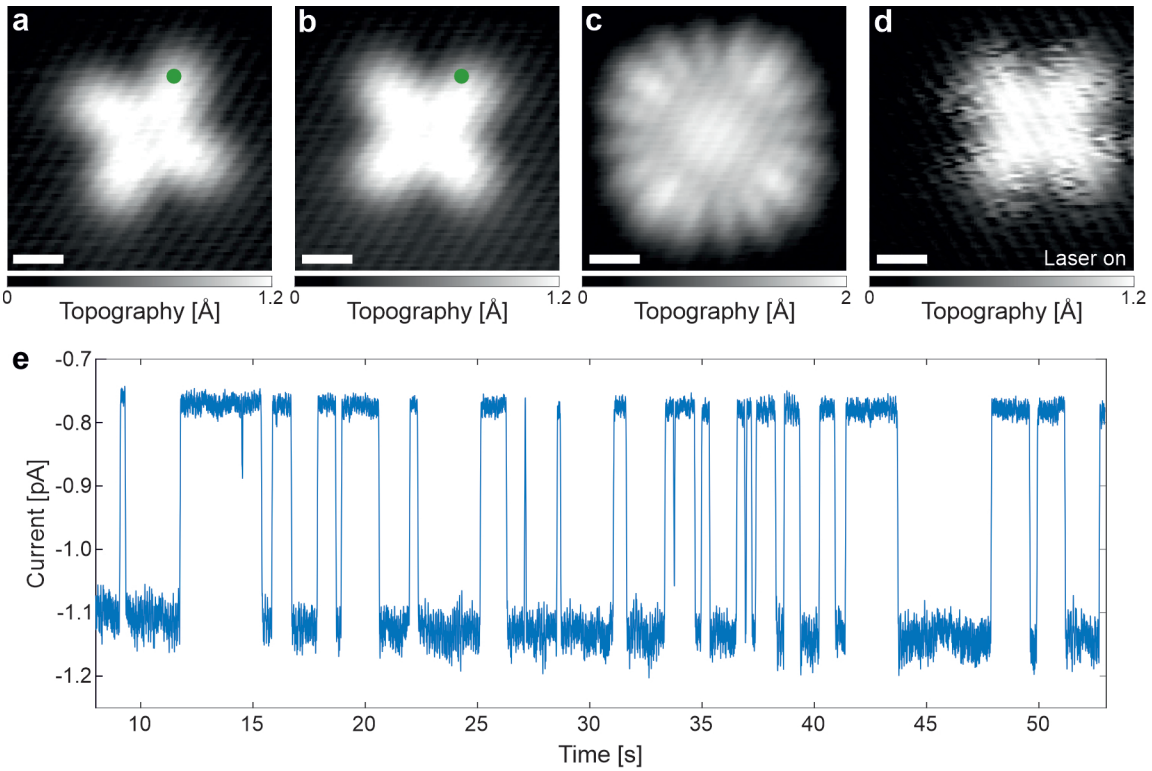

Figure 6.6: Photoinduced switching of a single MgPc molecule. **a**,**b**, DC-STM images of the left-rotated (**a**) and right-rotated (**b**) geometry. The scale bar corresponds to 5 Å and applies to all images. Setpoint: −300 mV, 2 pA. **c**, DC-STM image of the HOMO. The charge-induced rapid toggling between the two stable adsorption sites results in an incoherent superposition of the orbital in both geometries. Setpoint: −1.9 V, 2 pA. **d**, In-gap STM image while the laser is illuminating the junction. The telegraph noise at the edges of the molecule indicates a switching between the adsorption geometries. Setpoint: −300 mV, 2 pA. **e**, Typical current trace while the tip is positioned on one arm of the molecule, as indicated by the green dot in **a** and **b**. The rapid jumps in the current indicate a change in the molecular conformation. CW Laser power for **d** & **e**: 2.43 mW

current while laser pulses are coupled to the tip-sample junction, the resulting time trace exhibits the characteristic jumping between two levels (figure 6.6e). Here, a jump from low to high current corresponds to the molecule switching towards the tip (for the position indicated in figure 6.6a) and a jump from high to low current to the molecule switching away from the tip respectively.

This first dataset indicates, that the laser can indeed cause the molecule to switch between its two stable adsorption geometries. The exact process, however, which causes the excitation of the molecule to be translated into a motion of the molecular frame, is not apparent right away. To this end, the possible processes involved in the photoexcitation and subsequent relaxation of the molecule are discussed in the

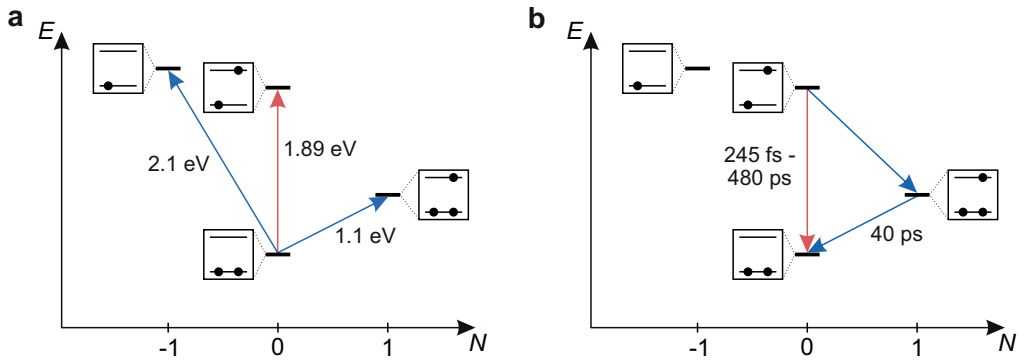

Figure 6.7: Many-body energy diagram of MgPc. a, Energy diagram for the optical excitation (red arrow) and the first charging transitions (blue arrows). The associated energies for the respective transitions are indicated next to the arrows. **b**, Lifetimes of the excited states for a molecule adsorbed on 3ML NaCl. Sources to the lifetimes are given in the main text.

following. A many-body energy diagram of the involved states and possible molecule excitations is shown in figure 6.7a, where the x-axis denotes the number of additional electrons in the system compared to the ground state and the y-axis describes the free energy of the system (see also chapter 3.4). The presented diagram depicts the situation at zero bias between tip and sample. Before any excitation takes place, the molecule is assumed to be in its ground state, where two electrons are populating the HOMO and the LUMO is unoccupied. From this point, there are three possible excitations, one of which involves a direct photoexcitation (red arrow) and two encompass electron tunneling and thus a change in the charge state (blue arrows). Since the former does not involve any electron tunneling, the transition is indicated vertically in the diagram and entails exciting an electron from the HOMO to the LUMO. The energy of this transition is around 1.89 eV [38]. The latter excitations correspond to the positive and negative ion resonances [12, 173], the energies of which equate to the bias voltage needed to access these resonances in an STM experiment and can thus be determined easily via STS [174]. In this depiction it becomes apparent, that the positive ion resonance (i.e. the state with $N = -1$ electrons compared to the ground state) has a higher energy than the optically excited state. This implies that the relaxation from the optically excited state can not take place via the positive ion resonance while no bias is applied to the junction. The negative ion resonance, however, is located energetically between the neutral ground state and the optically excited state. This means that a relaxation via an intermediate, negatively charged state is energetically possible, which involves charge transfer between molecule and one of the STM electrodes (i.e. metallic substrate or tip).

Thus, after photoexcitation, there are two possible relaxation pathways, namely the radiative decay of the excited state and the exchange of electrons with the STM electrodes through a transiently negatively charged molecular state, which is later referred to as nonradiative relaxation/decay. Which process is dominant is then

determined by the timescales of the respective pathways that are shown in 6.7b. The lifetimes for the radiative decay of the molecule can be derived from other experiments, which range from around 245 fs to 22.5 ps [175], 1.7 ps to 18.9 ps [176] (both of the aforementioned results obtained for MgPc thin films), to 480 ps (derived from photon correlation measurements) [177], obtained from STML experiments for a molecule adsorbed on 3 ML NaCl. The lifetime of the negatively charged state has also recently been experimentally determined to be approximately 40 ps for a molecule on 3 ML NaCl [173]. Importantly, the STML experiments show a reduced emission from molecules situated on 3 ML NaCl, which is attributed to the already large nonradiative decay rate via substrate tunneling [177]. This indicates, that the radiative and nonradiative decay rates are around the same magnitude, and both relaxation processes are competing for a molecule adsorbed on 3 ML NaCl.

Since the tunneling rate from molecule to substrate and vice versa is competing with the radiative decay rate of the excited state, our current hypothesis for the photoinduced motion of the molecule is the following: After the molecule is optically excited by the laser, the resulting hole in the HOMO is refilled by an electron from one of the STM electrodes, i.e. tip or substrate. This leaves the molecule in a charged state, which will align its conformation with the high symmetry directions of the NaCl substrate (see refs. [80, 103] or chapter 5). After a certain time, the transient charge state will be neutralized and thus the molecule will relax back to the neutral ground state. Following this, the configuration of the molecule will change back to one of the stable geometries, making a switching of the adsorption geometry possible. The rate of nonradiative decay can be enhanced by increasing the tunneling rate of electrons in the molecule to one of the STM electrodes, which will be realized by bringing the tip closer to the molecule. This way an increase of the photoinduced toggling rate is to be expected. On the other hand, relaxation via radiative decay does not cause a transiently charged state. Therefore, an unswitched configuration is expected. However, vibration-induced molecular toggling motion can not be fully excluded in this case [42].

6.7 Investigation of the Photoinduced Switching Mechanism

In order to test the aforementioned hypothesis, the photoinduced switching of the molecule will be examined with the new capabilities enabled by the synchronization of the AFM oscillation with the laser pulses coupled to the SPM junction. By varying the phase of the pulses with respect to the cantilever oscillation, the molecule can be excited at different tip heights, which will allow us to verify that the switching of the molecule is indeed facilitated by a transient charging following a direct photoexcitation of the molecule.

To this end, it is indicative to evaluate the possible relaxation processes of the molecule. Figure 6.8 depicts those in a single particle picture for the case of zero

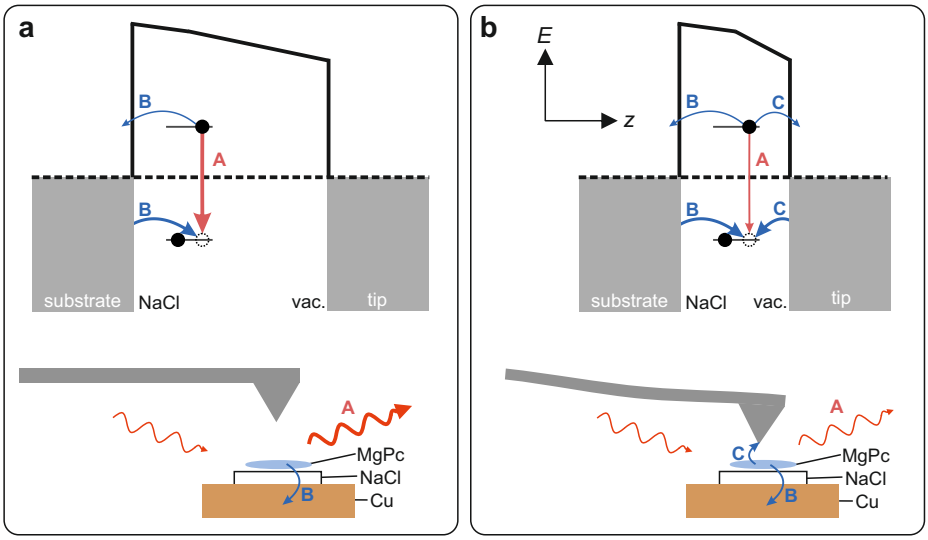

Figure 6.8: Tunneling scheme of the possible relaxation pathways. **a**, When the tip is far away from the molecule during photoexcitation, the only possible relaxation pathways are are radiative decay of the exciton (red arrow, A) or substrate tunneling (blue arrows, B). Due to the wide vacuum barrier, tunneling to the tip is significantly suppressed. **b**, Compared to the situation depicted in **a**, the molecule can also nonradiatively relax due to tunneling to and from the tip (blue arrows, C), if photoexcitation occurs while the tip is close to the molecule.

applied bias. It was already discussed in figure 6.7 that the relaxation process via a intermediate negatively charged state is energetically favored in this case. This depiction of the transitions shows with which electrodes charges can be exchanged and serves as a complementary approach to the many-body picture.

If photoexcitation occurs while the tip is far away from the molecule, there are only two possible relaxation processes for the molecule. As shown in figure 6.8a, only radiative decay and charge transfer to the metallic substrate can facilitate the relaxation of the photoexcited state back to the ground state. Since the tunneling barrier between molecular states and the tip is exceedingly wide, tunneling to the tip is severely suppressed. This situation changes significantly, when the molecule is excited by the laser while the tip is close to the molecule, as is shown in figure 6.8b. Due to the proximity of the tip to the molecule, exchanging charges between molecular states and tip is now possible. Since the tip-molecule distance in an experiment can be deliberately controlled, relaxation of the molecule via tip tunneling may in fact become the dominant process. As the nonradiative relaxation to the substrate is predominantly given by the thickness of the underlying insulating NaCl layer and the radiative decay rate is assumed to be constant for each given thickness of NaCl, adding the possibility for the molecule to relax via tunneling to the tip should quench the radiative decay rate (as indicated by different arrow thicknesses in figure 6.8) and increase the decay rates via an intermediate, transiently charged state.

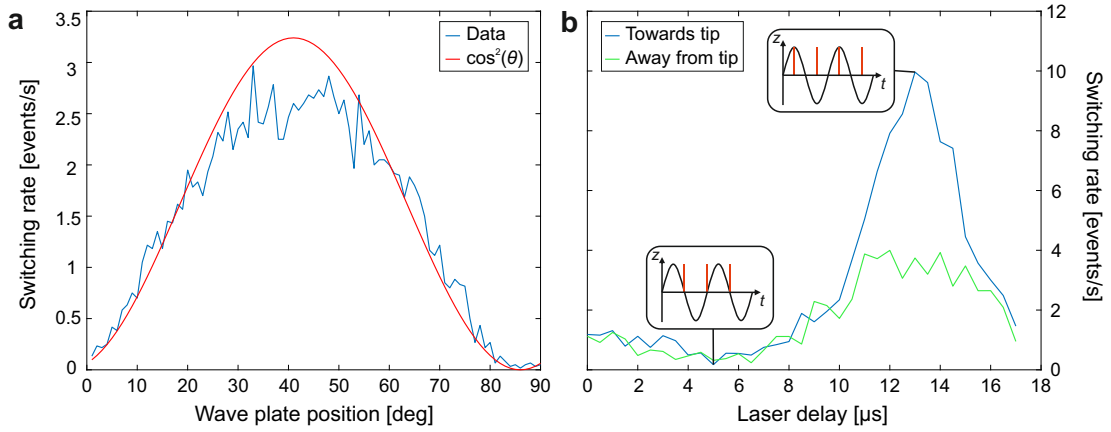

Figure 6.9: Polarization and laser delay dependence of the switching rate. **a**, Polarization dependence of the switching rate of a molecule on 2 ML NaCl. For each data point, the switching of the molecule was monitored for 60 s, while a CW laser power of 2 μW was coupled to the junction. AFM amplitude was set to 10 Å and the STM feedback was switched off at a setpoint of −300 mV, 1 pA on the NaCl. The red curve represents a shifted $\cos^2(\theta)$ function. **b**, Delay dependence of the switching rate of a molecule on 3 ML NaCl. For each data point, the switching of the molecule was monitored for 62.5 s, while a CW laser power of 2.4 mW was coupled to the junction. The AFM oscillation amplitude was set top 10 Å. The insets show, at which delays the laser pulses occur at the zero crossings or turning points of the oscillation. While recording the switching behavior, a bias voltage of −200 mV was applied to facilitate a non-resonant detection current.

Applying these considerations to the setup described earlier, the two situations depicted in figure 6.8 can be achieved via the synchronization of the laser pulses with the cantilever oscillation. By adjusting the phase between the pulses and the cantilever oscillation, the pulses can be tuned to occur at the zero crossing (i.e. far away from the molecule, see also figure 6.3a) or at the turning points of the oscillation (i.e. close to the molecule, see also figure 6.3b). Similar to the experiments described in chapter 5, a non-resonant detection current can be used in order to monitor the adsorption geometry of the molecule without directly triggering any switching events. This non-resonant detection predominantly arises from the bottom turning point of the cantilever oscillation [170].

A first check of the technique is shown in figure 6.9a, which depicts the behavior of the switching rate when the polarization of the incident laser is changed. Since a $\lambda/2$ wave plate is implemented in the laser setup, the polarization can be freely rotated while the STM is in operation without compromising the stability of the junction. Here, a maximum of the switching rate is observed when the wave plate is rotated by around 42° with respect to the initial polarization direction of the laser. As the direct laser output is horizontally polarized, this wave plate rotation corresponds to a resulting polarization of the laser parallel to the tip. Since this situation allows

for an enhanced coupling to the SPM tip, it leads to an increased switching rate due to the field enhancement in the tip-sample junction. The difference to the expected value of 45° for the wave plate rotation at which the maximum switching rate would be expected is most likely due to a slight bending of the tip.

When setting the polarization to be parallel to the tip and monitoring the switching rate of a molecule on 3 ML NaCl while sweeping the phase between AFM oscillation and laser pulses, one observes a typical trace as shown in figure 6.9b. The x-axis is given by the delay between laser trigger pulse and AFM trigger pulse. Since the resonance frequency of the cantilever is around 28.5 kHz (see figure 6.4a), which equates to a period of 35 μs per cycle, a delay sweep of two pulses from 0 to 17 μs corresponds to probing almost the full oscillation cycle. The first observation made from this data is, that the switching rate becomes minimal for a delay of around 5 μs, while it is maximal for a delay of 13 μs, which corresponds to the laser pulses occurring at the zero crossing of the oscillation and at the turning point respectively. For further illustration the laser timing with respect to the cantilever oscillation is indicated by the insets in figure 6.9b. Since the tunneling after photoexcitation is a stochastic process, it can take place at any point in time during the laser pulse. While it could be possible that electron tunneling from or to the excited molecule occurs after the laser pulse is already over and thus cause an error in the determination of the tip-molecule distance from the laser delay, the lifetimes indicated in figure 6.7b ($\approx$ 100 ps) are orders of magnitude shorter than the laser pulse duration ($\approx$ 150 ns) and the oscillation period of the cantilever ($\approx$ 35 μs). Thus, electron tunneling after the laser pulse can be neglected. The second observation is the disparity between the two switching directions, namely towards the tip (blue curve) and away from the tip (green curve). Since every switching event is recorded individually, the direction of the movement can be easily identified from the current traces. While these two curves overlap when the molecule is excited when the tip is far away, a clear difference arises when the laser is introduced to the junction while the tip is close to the molecule. This might be an effect of the increased tunneling rate between molecule and tip, which will be discussed in detail further below.

When comparing the data shown in figures 6.9a and b, which are taken for two different molecules, where one is adsorbed on 2 ML NaCl (figure 6.9a) and the other on 3 ML NaCl (figure 6.9b), the recorded switching rate for these molecules is of the same order of magnitude, while the incident laser power is three magnitudes larger for the molecule on 3 ML NaCl. One possible explanation for this behavior is that the molecule on 2 ML NaCl exhibits an increased nonradiative decay rate due to the reduced barrier width between molecule and substrate. This would lead to more relaxation processes via the transiently charged state and consequently an increased switching rate of the molecule. However, to confirm this hypothesis, a more conclusive dataset is necessary, where the tip height and laser power are properly adjusted to be able to quantitatively compare molecules situated on different NaCl layers.

In order to understand how the tunneling rate between tip and molecule can affect the data shown in figure 6.9b, the lateral tip position has to be considered as well

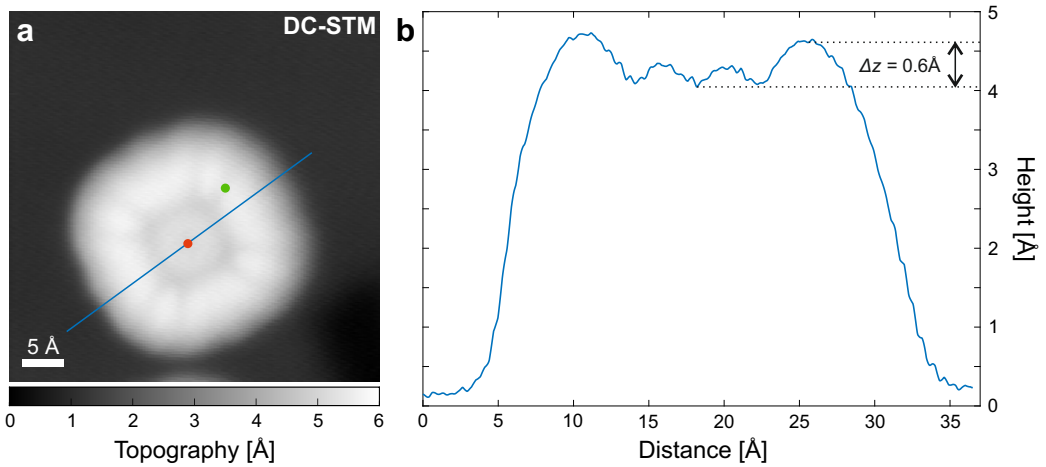

Figure 6.10: Tip height determination during switching experiments. a, DC-STM image of the LUMO of MgPc. The red dot in the center of the orbital indicates the position, at which the tip height is set for the switching experiments. The green dot represents the position at which the spectra were taken. Setpoint: 1.1 V, 2 pA. **b**, Line profile along the line indicated in **a**. The apparent height difference between the center of the molecule and the outer lobe is approximately 0.6 Å.

as the specific tip-molecule distance while observing the switching behavior. To this end, a DC-STM image of the LUMO is shown in figure 6.10a, where the two relevant positions are indicated. In order to obtain the previously shown data, the tip is first positioned in the center of the orbital (red dot in figure 6.10a) with a set point of 1.1 V, 2 pA, which is the voltage at which the LUMO can be accessed. There, the STM feedback is switched off which fixes the tip height to a well defined position. Since the tunneling current predominantly stems from the bottom turnaround point of the cantilever oscillation, the tunneling rate to the LUMO at this cantilever position can be assumed to be given by

$$\Gamma_1 = \frac{I}{e} = \frac{2 \cdot 10^{-12}\mathrm{A}}{1.6022 \cdot 10^{-19}\,\mathrm{C}} \approx 1.25 \cdot 10^7 \,\frac{\text{electrons}}{\mathrm{s}} \rightarrow \tau_1 = \frac{1}{\Gamma_1} = 8 \cdot 10^{-8}\,\mathrm{s},$$

where Γ_1 is the tunneling rate from tip to molecule and τ_1 describes the average tunneling time from tip to molecule. After setting the tip height to this position, the bias is reduced in order to only facilitate a non-resonant detection current, which allows monitoring the switching behavior. Then, the tip is moved to the position indicated by a green dot in figure 6.10a and approached to the molecule by $\Delta z = 2.6$ Å, where then the switching of the molecule is recorded.

Since this position is located in the nodal plane of the right rotated geometry of the molecule, a difference between the switching rate into and out of the tunneling junction might be explained as follows: If the molecule is in the right rotated conformation, the s-wave of the front atom of the tip has less overlap with the LUMO due to nodal plane of the molecule being located directly under the tip, which leads

to a reduced tunneling probability from molecule to tip. In the situation where the molecule is in the left rotated geometry, the tip is positioned directly over a lobe of the LUMO, leading to an increased tunneling rate between tip and molecule. Due to these different rates, the directional dependence of the switching rate shown in fig 6.9b indicates an influence of the molecular orbital on the switching rate.

This implies, that the increased switching rate observed for photoexcitation at small tip-molecule distances is due to relaxation via a transiently charged state facilitated by electron exchange with the tip. In order to corroborate this, the tunneling rate to the LUMO, while the switching traces are recorded, can be compared to the decay rates via the other relaxation channels. Figure 6.10b depicts a line scan across the LUMO which shows, that the apparent height of the lobe of the orbital is approximately 0.6 Å larger than at the center of the molecule, where the tip height for the measurement is fixed. Taking this difference into account as well as the approach of $\Delta z = 2.6\,\text{Å}$ before recording the switching traces, one can estimate the molecule-tip tunneling rate Γ_2 and average tunneling time τ_2 as follows:

$$\Gamma_2 = \Gamma_1 \cdot 10^{0.6+2.6} = 1.25 \cdot 10^7 \,\frac{\text{electrons}}{\text{s}} \cdot 10^{3.2} \approx 1.98 \cdot 10^{10} \,\frac{\text{electrons}}{\text{s}}$$

$$\rightarrow \tau_2 = \frac{1}{\Gamma_2} \approx 51 \cdot 10^{-12}\,\text{s} = 51\,\text{ps}.$$

Here it was used, that every reduction of tip-sample distance of 1 Å leads to an approximate tenfold increase of tunneling rate (see also chapter 2.1). This rough estimation shows, that the tunneling time in the data shown in figure 6.9b is on the same order of magnitude as the relaxation times shown in refs. [173, 175, 176] which are noted in figure 6.7b (i.e. on the timescale of tens of picoseconds), indicating that charge exchange via the tip might indeed be the cause of the enhanced switching rate when the laser is hitting the junction at the bottom turning point of the cantilever oscillation.

To further corroborate this analysis, the data shown in figure 6.9b can be investigated from a different viewpoint. As discussed earlier, the change in the delay time of the laser can be interpreted as a variation of the tip-molecule distance, at which the laser is coupled to the junction. Since both the frequency and the phase of the AFM oscillation are known, the delay time of the laser can be converted into an effective change in height. The result of this is shown in figure 6.11, separated for each switching direction respectively. Figure 6.11a shows the switching rate towards the tip as a function of the distance relative to the zero-crossing ($\Delta z = 0\,\text{Å}$ in figure 6.11) of the cantilever oscillation, which features a rapid increase of the switching rate at small tip-molecule distances (i.e. large Δz). The data was fitted using a combination of two different fitting functions, namely $f_{\text{fit}}(\Delta z) = a\,(\Delta z)^b + c \cdot \exp(-d \cdot \Delta z)$ (green curve in figure 6.11a). For large tip-molecule distance ($\Delta z \leq 7\,\text{Å}$), the data is well reproduced by a power law of the form $f_{\text{p}}(\Delta z) = a\,(\Delta z)^b$ (red curve in figure 6.11a). In this case, $b \approx -3$, which conforms well with values obtained for the distance dependence of

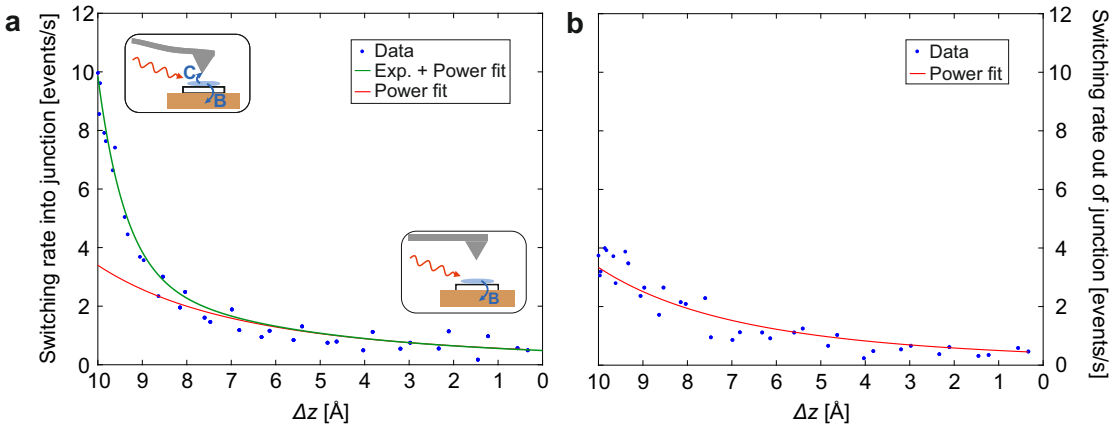

Figure 6.11: Directional switching rate as a function of tip-molecule distance. **a**, Rate for switching the molecule towards the tip. For large tip-molecule distances ($\Delta z \leq 7\,\text{Å}$), the switching rate follows a power-law dependence, while it increases exponentially for small distances ($\Delta z \geq 8.5\,\text{Å}$). The insets show the cantilever position for the two extreme cases of zero-crossing and turning point of the AFM oscillation. **b**, Rate for switching the molecule away from the tip. The same fitting curve as for the power dependency obtained in **a** is shown. This switching direction does not exhibit an exponential behavior for small tip-molecule distances. Experimental parameters: See figure 6.9b.

the electromagnetic field enhancement in theoretical models [66]. This stronger enhancement leads to an increased number of photoexcitations of the molecule, which translates into a larger switching rate due to relaxations via charge exchange with the metallic substrate. An exponential function of the form $f_e(\Delta z) = c \cdot \exp(-d \cdot \Delta z)$ was added to fit the data for small tip-molecule distances ($\Delta z \geq 8.5\,\text{Å}$). While the fit matches the data quite well, the value for $d = 1.66\,\text{Å}^{-1}$ is slightly smaller than what one would expect from a simple tunneling model (see section 2.1). This might be due to a reduced effective barrier height for LUMO tunneling in the presented low bias scenario, but a definitive interpretation of this discrepancy requires further theoretical and experimental analysis of this system. Irrespective of the exact decay constant, the exponential increase for small tip-molecule distance is indicative of the onset of a relaxation of the molecule via charge exchange between tip and molecule. The fact that this behavior is absent for the other switching direction depicted in figure 6.11b further underlines this fact. As described earlier, the overlap between LUMO and tip wave function is reduced in this situation, which results in a significantly diminished tunneling rate between tip and molecule. Thus, no additional relaxation pathway is present in this situation, resulting in the absence of the increased switching rate for large Δz. Furthermore, the data seems to solely exhibit a power dependence similar to the one observed in figure 6.11a, what hints towards the increase in switching rate being only due to field enhancement in the junction.

As a final step, maps of the switching rate separately for each direction were

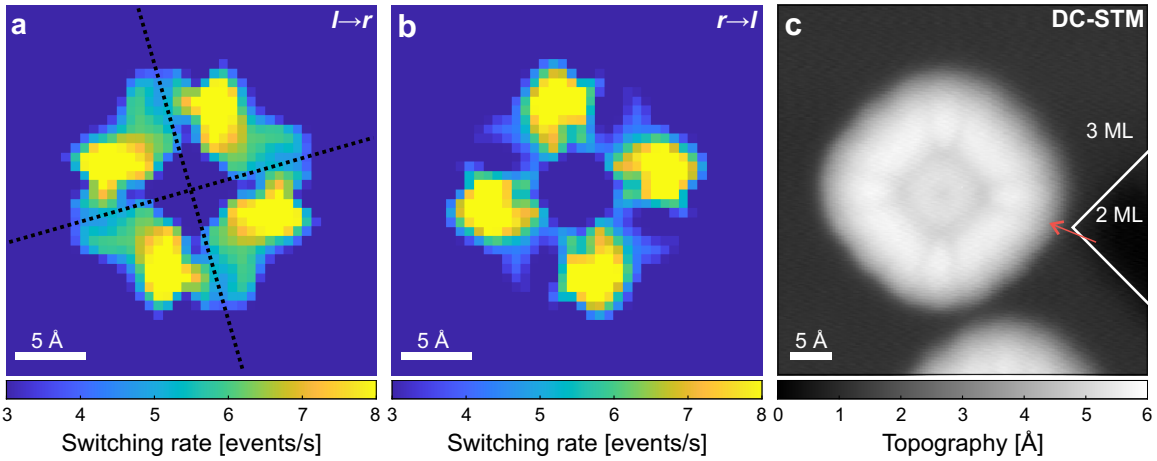

Figure 6.12: Maps of the photoinduced switching of a single molecule. **a**, Spatially resolved switching rate from left-rotated to right-rotated geometry. The overall map resembles the LUMO of the molecule when it is situated in the left-rotated geometry, what is manifested in the visibility of the characteristic nodal planes of the orbital (indicated by dashed lines). **b** Map of the switching rate from right-rotated to left-rotated geometry. While this map also features contrast on the submolecular scale, the resemblance to a molecular orbital is less pronounced as for the other direction shown in **a**. Experimental parameters for **a** & **b**: Tip height set in center of the orbital at a setpoint of 1.1 V, 2 pA; bias voltage during spectra: −200 mV; z-approach: 2.6 Å; switching recorded for 39.5 s for each pixel; laser delay: $\Delta t_{\mathrm{L}} = 13\,\mu$s (pulses occurring at turning points of the cantilever oscillation). **c**, DC-STM image of the same molecule as in **a** & **b**. The molecule is situated near a step edge from 3 ML to 2 ML NaCl, where the right rotated geometry is closer to the step edge (indicated by red arrow). Setpoint: 1.1 V, 2 pA.

recorded, which are shown in figure 6.12. For the switching rate from left-rotated to right-rotated configuration (figure 6.12a), a map which closely resembles the LUMO density of the molecule in the left rotated geometry was obtained (see also the maps of the simulated charging probability shown in figure 5.4b). This contrast is assumed to be originating from the relaxation of the photoexcited state of the molecule by the exchange of charges with the tip. When the tip is in a position where the s-wave of the tip front atom has a large overlap with the LUMO, charge exchange between molecule and tip can occur with high efficiency, leaving it in a transiently charged state and thus facilitate the switching to the other adsorption geometry. While this map features lobes and nodal planes where one would expect them from the LUMO of the molecule, the orbital features appear less pronounced in the switching map. This is attributed to the remaining background arising from the relaxation via charge exchange with the substrate. Since this process is independent of the tip position, it results in a background contribution to the switching rate which will overall slightly blur the obtained contrast.

While the data presented in figure 6.12a resembles the LUMO of the molecule, this is not the case for the switching rate when toggling the molecule from right-rotated to left-rotated conformation, as shown in figure 6.12b. This map also shows a dependence of the switching rate on the exact tip position, but does not show an exact mirror image of the map for the other direction. One reason for this asymmetry might be the proximity of the molecule to a step edge of the underlying NaCl layer, as shown in figure 6.12c. This DC-STM image of the LUMO shows, that the nodal plane arising from the right-rotated geometry is located close to a step edge in the underlying NaCl layers (red arrow in figure 6.12c). Since the nodal planes of the LUMO of MgPc are centered along the symmetry axis of the molecular structure, one of the arms of the molecule might be positioned too close to the step edge. Thus, the molecule might be perturbed by the step edge, for example by a slight change of the adsorption geometry compared to the left rotated conformation.

6.8 Summary & Outlook

In this chapter we have shown, that we can trigger the photoinduced motion of a single molecule switch adsorbed on a thin layer of NaCl. By employing an optical laser, we were able to cause a direct photoexcitation of the molecule, which facilitates a change of the adsorption geometry of a single magnesium phthalocyanine by transiently charging the molecule during its nonradiative relaxation process. In particular, the following was demonstrated:

- A new combination of an optical nanosecond pulsed laser and a low temperature, ultra-high vacuum scanning probe microscope has been established. Utilizing an automated alignment procedure we can ensure the proper coupling of the laser to the tip-sample junction.
- The synchronization of the optical laser pulses with the oscillation of an AFM cantilever comprises a novel experimental technique, which enables the study of photoexcitation processes even when the tip is out of tunneling contact with the sample. Employing a pulsed laser allows us to couple high power laser pulses to the SPM without introducing a large amount of heat to the low temperature system.
- We thoroughly investigated the perturbing effects of the laser on the tip-sample junction. While we found, that the laser pulses can excite the second flexural mode of the cantilever and heat the junction on a long timescale, we can avoid those by choosing proper experimental conditions.
- Using this setup, we found that it can be used to excite single magnesium phthalocyanine molecules adsorbed on an ultra-thin insulating NaCl layer, causing them to perform a switching motion between their two stable neutral adsorption geometries.
- By comparing the rates for radiative and nonradiative relaxation processes after photoexcitation we could infer that the rotational motion of the molecule is

facilitated by an intermediate transiently charged state. This is due to the nonradiative relaxation process involving the exchange of electrons with the STM electrodes.

- Utilizing the capabilities of the synchronization of laser pulses and AFM oscillation, we were able study the effects of photoexcitation at small and large tip-molecule distances. The switching rate of the molecule increased due to the field enhancement at large distances, while the behavior changed to an exponential increase of the switching rate when the tip was brought into close proximity of the molecule, which suggests charge exchange with the tip as an additional relaxation pathway.
- As a last step, we examined the dependence of the switching rate on the lateral tip position above the molecule. There we find, that the switching rate follows the contours of the LUMO of the molecule when the tip is in close proximity to the molecule during photoexcitation. This further supports our hypothesis, that the laser directly excites the molecule and causes a photoinduced motion via the formation of an intermediate charge state during the nonradiative relaxation process.

While these results show that the study of the effects of direct photoexcitation on molecular length scales is possible by combining optical lasers and SPM, there are still details of this experiment which need further investigation:

- As already suggested in the description of the experiment, a study of the relaxation processes for different thicknesses of the underlying NaCl layer might yield valuable insights. Since the molecule can also exchange charges with the substrate in a nonradiative decay of the exciton, a thicker decoupling layer might for example reduce the remaining background and provide a clearer picture.
- While charge exchange with the STM electrodes is the most likely explanation for the effects seen in this chapter, the exact details of the mechanism are not fully understood yet. For example, the nonradiative relaxation involves two processes: tunneling an electron out of the LUMO and an electron into the HOMO. The data reveals, that the switching rate is enhanced when the photoexcited electron tunnels from the LUMO to the tip. However, the mechanism for repopulating the HOMO has thus far remained elusive.

Regardless of these details, we have developed a method to facilitate direct photoexcitation of single molecules and to analyze the imminent effects thereof. We have demonstrated, that the toggling motion of MgPc is a consequence of the nonradiative relaxation of the excited state, which entails the formation of a transiently charged state. These results directly connect to recent studies, which show the remote driving of this toggling motion by exciting a plasmon in close proximity to the molecule [42]. Our results suggest that this plasmon might create an exciton, which in turn causes the molecular motion via a nonradiative relaxation of the molecule. In summary, we think that our results can assist in the understanding and interpretation of experiments performed on single molecule excited states.

While the excitation of photoinduced motion of a single molecule provides a testing ground for the study of exciton relaxations, this technique could be extended to other systems. Implementing the nanosecond laser pulses in the study of molecules on thick insulating layers would provide a versatile platform for investigating effects of photoexcitation. With the recent advances in the study of electronic transitions on thick insulating films [99] and of direct photocurrent imaging [76], the study of excitons in charge-stable molecule systems with single electron sensitivity would bear good prospects for the investigation of light-matter interactions.

7 Generation and Mapping of Single Electron Photocurrents

The results presented in this chapter have been obtained and interpreted in collaboration with Lisanne Sellies, who contributed to this project in the scope of her Master thesis [178], Laerte Patera and Jascha Repp. The results presented in this chapter provide a preliminary interpretation of the experimental observations.

In this chapter, results on single electron photocurrent generation and development of direct exciton mapping in a single molecule are presented. By combining an atomic force microscope (AFM) with a nanosecond pulsed laser system, a single copper phthalocyanine (CuPc) molecule can be photoexcited and single electrons can be removed or added to selected molecular states.

This control is achieved by depositing the molecules on a thick insulating NaCl layer grown on Cu(111), preventing any charge exchange between molecule and the metallic substrate. This way electrons can only be exchanged with the metallic AFM tip. Furthermore, the charge bistability of single molecules on thick insulating films permits limiting the generated photocurrents to single electrons. Since different charge states of the molecule result in a change of the force between tip and molecule, direct observation of single electron photocurrents is possible.

Synchronizing the pulsed laser with the AFM cantilever oscillation allows charging and discharging the molecule within a single cantilever cycle, what leads to a dissipative force and thus to a damping of the cantilever oscillation, which can be directly observed. Employing voltage pulses to expedite the discharging of the molecule after photoexcitation comprises a robust method to generate and successively detect single electron photocurrents.

This technique allows the study of photoexcited states of single molecules and facilitates direct access to the electron and hole parts of the molecular exciton. First maps of the photocurrents originating from the excited state orbitals are presented and methods for possible improvements are discussed.

7.1 Introduction

As presented in chapter 6, novel combinations of STM with optical techniques enable the study of excited states of single molecules. While STM luminescence [31, 38–53, 70] and tip-enhanced Raman spectroscopy [19, 68–72] analyze light generated in and scattered from single molecules in the STM junction, recent developments towards direct photocurrent generation by Imada *et al.* [75] and Imai-Imada *et al.* [76] present a different approach, where photoinduced electron transfer is directly observed by the STM circuitry. This is achieved via resonant photoexcitation of a single molecule, which results in a transfer of electrons to and from the electrodes of the STM, i.e. tip and sample. While this technique lays the groundwork for the study of excited molecular states with sub-Ångström precision, it requires thorough theoretical analysis to fully understand the involved processes. Due to the presence of tip and sample as electrodes there are several possible tunneling pathways contributing to the observed current, which can not be distinguished from the experiment alone [76].

In other research the investigation of single molecules on thick insulating films, specifically NaCl, was advanced considerably in recent years. While this prevents driving currents through molecular orbitals via sequential tunneling, experiments on single molecules can be performed with the use of AFM. The decoupling from the metallic substrate allows molecules to be studied in their respective charge states, which are preserved since relaxation is only possible via charge exchange with the tip. This permits the investigation of previously inaccessible phenomena at the molecular scale, for example charging of atoms via single electron transfer [179], lateral charge exchange between molecules [94, 102], bond fragmentation upon charging [110], reorganisation energies [113] and triplet quenching of single molecules [112] or the chemical structure of molecules in different charge states [93]. These techniques are also used in the study of excited states [111] and, with the recent advent of AC-STM (see also section 3.5), mapping electronic states of molecules adsorbed on these thick insulating layers has also become achievable [99, 103, 104].

Here, a combination of these two techniques is presented. By positioning molecules on a thick insulating layer, charge exchange with the metallic substrate can be suppressed. Photoexciting a molecule in this configuration forces any photoinduced electron transfer to occur between tip and molecule. The charge bistability of the molecule ensures only single electrons to be transferred from the molecule to the tip or vice versa. The limitation to AFM, however, necessitates employing a laser pulse scheme synchronized with the oscillation of the AFM cantilever. This enables an approach similar to AC-STM, where charging and discharging the molecule within a single cantilever oscillation leads to a measurable damping of the AFM. Since these photoelectrons originate from the excited state orbitals of the molecule, mapping these currents constitutes a pathway towards the direct imaging of molecular excitons.

As a first step, single copper phthalocyanine (CuPc) molecules situated on multilayer NaCl are investigated by means of AFM and AC-STM. Then, the generation of single electron photocurrents is demonstrated and the possible charging and discharg-

ing processes are discussed. First maps of the generated single electron photocurrents are displayed and the resulting contrast is interpreted. Furthermore, experiments on a molecule positioned close to a NaCl step edge and a CuPc/pentacene dimer are presented.

7.2 Methods

Sample Preparation The Cu(111) single crystal was cleaned by repeated cycles of neon ion sputtering and thermal annealing to 550 °C, where this temperature was reduced to 500 °C after the final sputtering cycle. Afterwards, approximately 25 monolayers of NaCl were evaporated from a crucible onto half of the sample, while the other half was covered by a mask to ensure clean areas of metal for tip preparation (see also section 4.2). The temperature of the sample during NaCl evaporation was kept at $\approx$ 100°C. The copper phthalocyanine molecules were deposited via flash evaporation onto the cold sample after transferring it to the STM.

Laser Setup In the experiments presented in this chapter, the same laser setup as described in chapter 6 was used. The alignment procedure is also detailed in the previous chapter. Unless stated otherwise, the laser was set to be polarized parallel to the tip and the duration of the laser pulses was set to $\approx$ 150 ns.

7.3 AFM & AC-STM Studies on CuPc on NaCl/Cu(111)

Before studying single electron photocurrents originating from CuPc, it is important to first analyze the system with regular AFM techniques. A constant Δf overview of the sample is shown in figure 7.1a, where several CuPc (see fig. 7.1b) molecules are visible. The first important process to be investigated is the charging of a single CuPc molecule, which is shown in figure 7.1c. Here, the charging hysteresis (see also section 3.4) is shown for four different tip-molecule distances, where two distinct features become apparent. The first point is that the center of the hysteresis is shifting to higher voltages when approaching the tip to the molecule, originating from the increased voltage drop in the underlying NaCl layer [113]. The second observation is that the hysteresis closes when the molecule is approached by the tip, which is both due to the increased tunneling probability between molecules and tip as well as an additional gating of the molecule by the tip motion [180]. The increased tunneling rate between tip and molecule causes charging and discharging to occur earlier during the bias voltage sweep, which results in the charging and discharging taking place at lower and at higher bias voltages respectively when approaching the tip to the molecule, what leads to a smaller hysteresis. The gating of the molecule

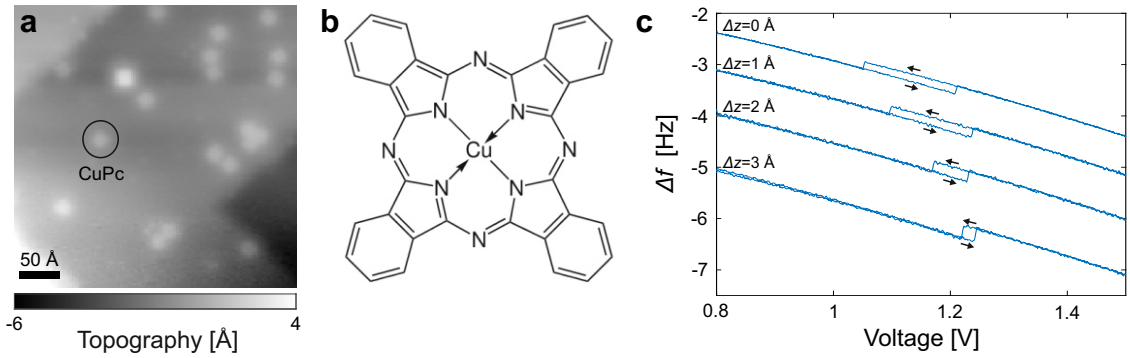

Figure 7.1: AFM studies on CuPc on NaCl/Cu(111). **a**, Constant Δf image of the NaCl surface. A single CuPc molecule is marked by a circle. Setpoint: 1 mV, 1.9 Hz. **b**, Chemical structure of CuPc. **c**, $\Delta f(V)$-spectra for four different tip molecule distances. The arrows indicate the direction of the bias sweep. The spectra are vertically offset by 0.5 Hz for visual clarity. The values for Δz describe the additional approach to the molecule after disabling the feedback at a setpoint of 1 mV, 0.8 Hz over the bare NaCl substrate.

can be attributed to a change in the voltage drop in the underlying NaCl layer, which will be discussed later in this chapter.

More important for the investigation of single electron photocurrents, however, is the analysis of the electronic states of CuPc, especially the distribution across the molecule. This can be done by using AC-STM. As described in section 3.5, this technique is based on the charging of a molecule synchronized with the cantilever oscillation via voltage pulses of alternating polarity. This leads to a non-conservative force on the cantilever, resulting in a measurable damping, an example of which is depicted in figure 7.2a. Here, the damping signal as well as the simultaneously recorded frequency shift Δf are shown as a function of the DC bias voltage, where the Δf-curve shows a progression from neutral to charged state visible in the form of a continuous transition to the Kelvin parabola of the charged state. Since the voltage pulses cause multiple transitions between neutral and charged states of the molecule per second, an average of the charge state population is detected by the AFM, leading to this continuous transition in contrast to the sudden jumps in Δf due to charging shown in figure 7.1c. The DC bias voltage, at which this transition occurs, will be used later in order to identify the relevant charging processes when analyzing the effects of photoexcitation.

Furthermore it becomes apparent from figure 7.2a that the damping signal caused by the AC voltage pulses is centered around the aforementioned transition to the charged state. Since for this DC bias voltage both charge states of the molecule are stable (see also section 3.5), charging and discharging of the molecule is facilitated only via the voltage pulses in this case. As the mechanism for photocurrent-induced damping presented later is attributed to a different origin, the AC-STM damping spectrum shown in 7.2a will be used to rationalize the involved charging transitions

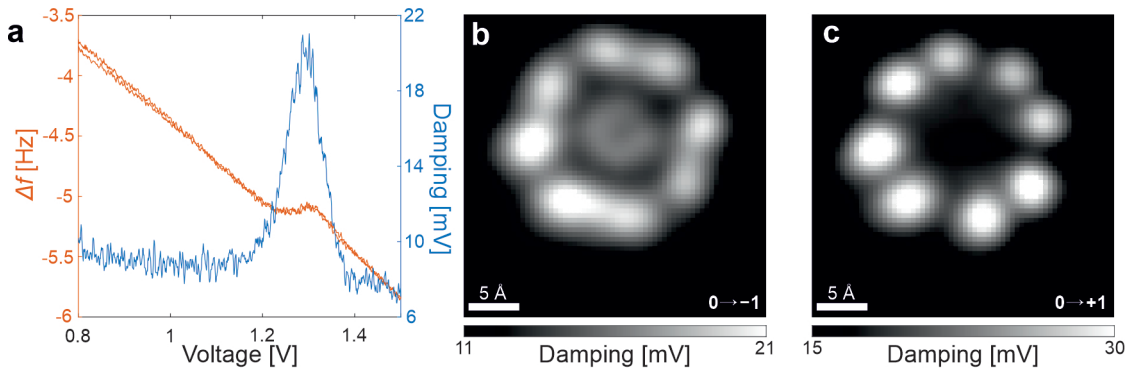

Figure 7.2: AC-STM studies on CuPc on NaCl/Cu(111) a. Δf (orange) and damping (blue) as a function of the applied DC bias voltage while AC voltage pulses are on. The charging hysteresis collapsed from two discrete steps to a continuous transition from neutral to charged state. The damping spectrum decreases after Δf shifted to the charged state parabola. Spectra were taken by approaching the molecule by 3.5 Å after disabling the feedback over the bare NaCl at a setpoint of 1 mV, 0.8 Hz; $V_{\mathrm{AC}} = 1.6\,\mathrm{V_{pp}}$. **b**, **c** AC-STM images of the $0 \rightarrow -1$ (**b**) and $0 \rightarrow +1$ (**c**) transitions. Experimental parameters: AFM amplitude: 1 Å **b**: $\Delta z = 4$ Å from a setpoint of 1 mV & 0.8 Hz over the bare NaCl, $V_{\mathrm{AC}} = 1.6\,\mathrm{V_{pp}}$, $V_{\mathrm{DC}} = 1.22$ V; **c**, $\Delta z = 2.5$ Å from a setpoint of 1 mV & 0.8 Hz over the bare NaCl, $V_{\mathrm{AC}} = 1.6\,\mathrm{V_{pp}}$, $V_{\mathrm{DC}} = -2.57$ V.

by comparing AC-STM and photoexcitation data.

Figures 7.2b and c show AC-STM images of the $0 \rightarrow -1$ (b) and $0 \rightarrow +1$ (c) charge transitions of CuPc, which closely resemble the orbital contrast of LUMO and HOMO of metal-based phthalocyanines obtained in thin film experiments [174]. As has been shown recently, the dominant contributions to photocurrent generation originate from these frontier orbitals [76], which is why the contrast of these orbitals is important for later experiments. Since in this experiment photocurrents are also expected to stem from these orbitals, these AC-STM images will be used later to associate the photocurrent maps with a respective orbital, allowing a founded evaluation of the origin of the observed photocurrents.

7.4 Generation of Single Electron Photocurrents

Now that the electronic configuration of CuPc on thick film NaCl/Cu(111) has been established, the generation of single electron photocurrents will be discussed. To this end, a nanosecond pulsed laser (NPL) with a center wavelength of 640 nm and a pulse duration of 150 ns is coupled to the SPM junction. For additional details on the experimental setup, see chapter 6.

Typical Δf spectra under laser illumination are shown in figure 7.3. Here, the laser is set to be polarized perpendicular to the tip, which reduces field enhancement

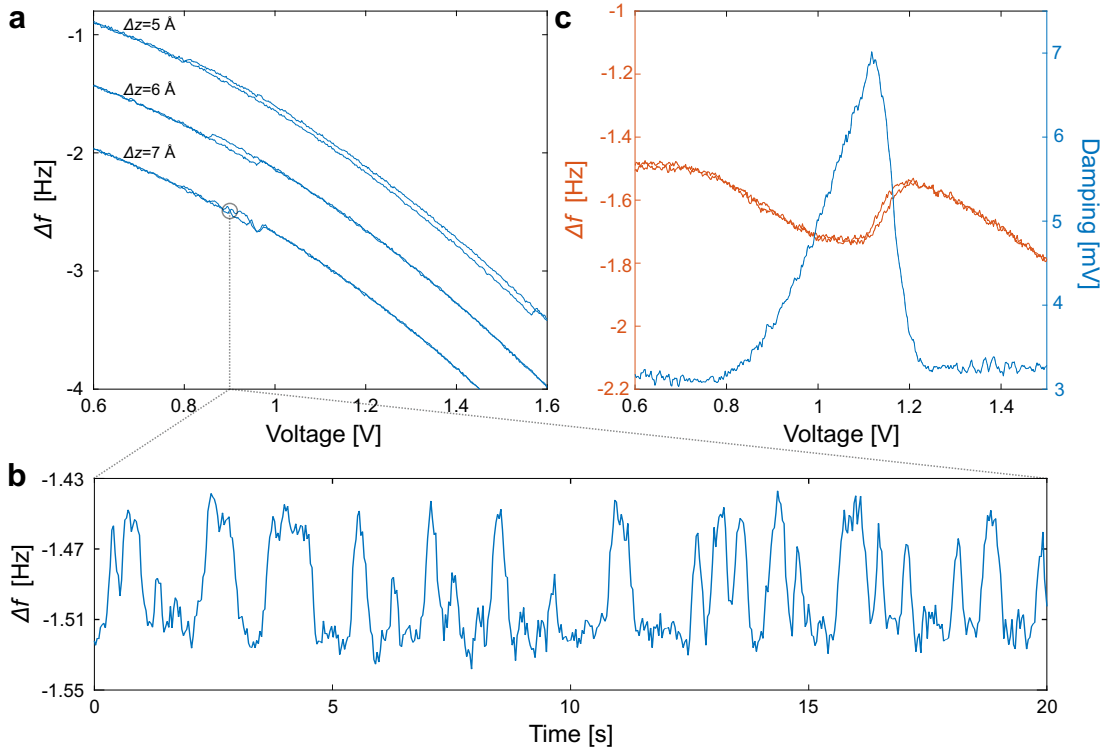

Figure 7.3: Δf- and damping spectra under laser illumination. **a**, Δf spectra obtained for a single CuPc molecule under laser illumination. The spectra are vertically offset by 0.5 Hz for visual clarity. The values for Δz describe the additional approach to the molecule after disabling the feedback at a setpoint of 1 mV, 0.5 Hz over the bare NaCl substrate. **b**, Δf switching trace, obtained for $\Delta z = 7$ Å and $V_{\mathrm{DC}} = 0.9$ V, as marked in **a**. **c**, Simultaneously recorded Δf- (orange) and damping (blue) spectra under laser illumination. The tip was approached by $\Delta z = 3.5$ Å from a setpoint of 1 mV, 0.5 Hz. Experimental parameters: AFM amplitude: 2 Å; CW laser power: 8.5 mW; Polarization: perpendicular to the tip (**a** & **b**), parallel to the tip (**c**); Laser delay: $\Delta t_{\mathrm{L}} = 7.6\,\mu$s (ZC).

in the junction and thus the excitation probability of the molecule (see also figures 6.9a and 7.9a). This is done to reduce photocurrent generation to be able to monitor individual charging processes of the molecule as a first step. Comparing the behavior observed in this case to figure 7.1c, where no laser is introduced to the junction, distinct differences appear. Firstly, the center of charging hysteresis of the molecule does not shift to higher voltages when moving the tip closer to the molecule. This behavior indicates that the molecule can already be charged at lower bias voltage, while the discharging process remains unaffected. This might be due to the excitation by the laser, as only the neutral molecule can be excited. Photoexcitation could lead to charging due to photocurrents, while the charged state can not be excited due to an increased optical gap and thus does not influence the discharging process. Secondly, the charging hysteresis seems to close more quickly when approaching the molecule

compared to figure 7.1c, which is linked to the same effect described above. Since the laser only enhances the charging of the molecule and appears to have no effect on the discharging, charging due to the laser excitation can occur at lower DC bias while discharging takes place at the same bias voltage as without laser illumination, leading to a smaller hysteresis. The third observation made from these curves is the rapid switching between neutral and charged state when the tip is brought closer to the molecule, which is shown in more detail in figure 7.3b. Keeping the bias voltage at a constant value of 0.9 V and monitoring the frequency shift, switching between two levels can be observed, which can be associated with the neutral and charged state of the molecule. Since the bias applied in this case is below the voltage, where the charging hysteresis without laser illumination is observed, this switching is likely due to charging via the generation of single electron photocurrents (jumps up in figure 7.3b) and discharging of the molecule via tunneling an electron from the molecule to the tip (jumps down in figure 7.3b). As discussed above, the laser assists only in the charging process, while the DC bias voltage is set below the charging hysteresis without laser illumination leading to discharging via regular tunneling.

While this behavior already hints towards the generation of single electron photocurrents, it is feasible to make use of the synchronization of the laser pulses to the cantilever oscillation. Similar to the case of AC-STM (see figure 7.2), charging and discharging the molecule within the same cantilever oscillation leads to a measurable damping signal. This can also be achieved for charging processes triggered by optically exciting the molecule, as shown in figure 7.3c, which shows a typical damping signal while illuminating the junction with the laser. Comparing this signal with the curve obtained for AC-STM (see figure 7.2a), the signal generated by photocurrents appears broader and more asymmetric, the reason of which will be discussed later in this chapter. Another observation is that the damping signal sharply drops to zero as soon as the molecule transitions to a predominantly charged state as indicated by the shift in Δf. The reason for this behavior is that the discharging of the molecule is facilitated by electrons tunneling from the molecule to the tip (see also figure 7.6). Once the bias voltage is too large, this tunneling process is suppressed and the molecule remains charged and no dissipation can be observed. It should also be noted that the charged molecule exhibits a significantly different optical gap [39, 181], which implies that the laser most likely can not excite the charged molecule, which might be another reason for the lack of photocurrent observed from the charged molecule.

The proposed mechanism responsible for the observed damping of the cantilever is depicted in figure 7.4a. The laser pulses are synchronized with the cantilever motion such that excitation of the molecule occurs at the zero crossing (ZC) of the oscillation. This excitation leads to a single electron photocurrent flowing between tip and molecule (see figure 7.4b). This leaves the molecule in a charged state, leading to an additional electrostatic force F_{el} acting on the cantilever. Since the bias voltage in this case is still below the regime of charge bistability, the molecule can be discharged

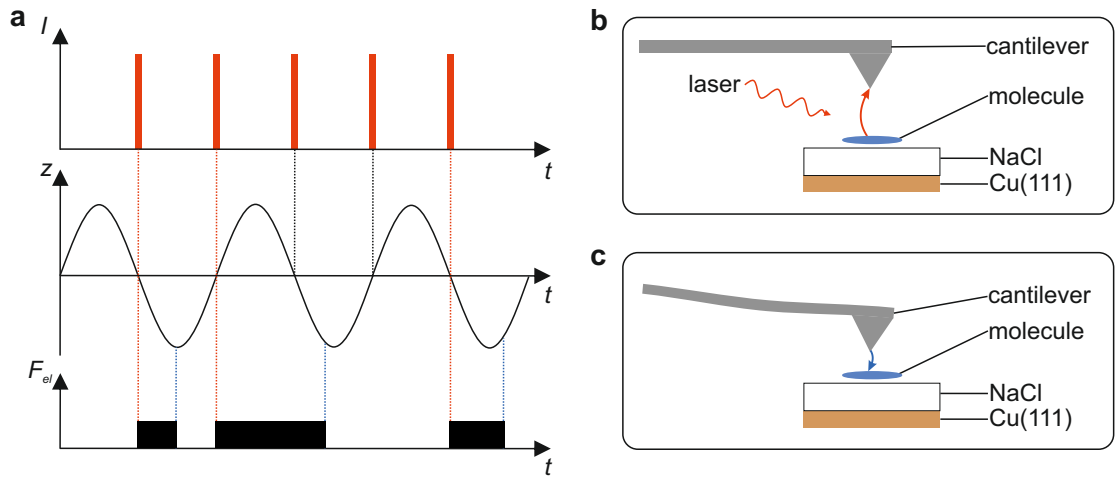

Figure 7.4: Dissipation from photocurrent generation and tunneling neutralization. **a**, Sketch of the charging and discharging events during the cantilever oscillation. The laser pulses situated at the zero crossings (ZC) of the cantilever oscillation generate a photocurrent, charging the molecule, as depicted in **b**. The discharging of the molecule occurs when the cantilever is close to the molecule via tunneling between tip and molecule (**c**).

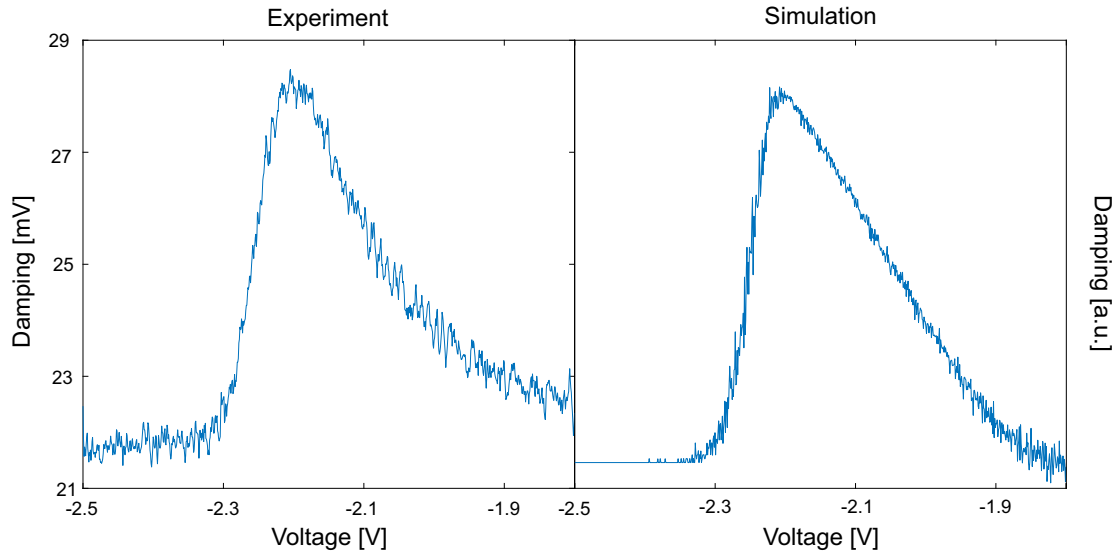

Figure 7.5: Comparison between experimentally obtained and simulated damping signal. The left dataset shows a typical damping signal for negative bias voltages. The tip was approached by 0.3 Å to the molecule after disabling the feedback at a setpoint of 1 mV, 1.3 Hz over the bare NaCl substrate. AFM amplitude: 2 Å; CW laser power: 4.78 mW, pulses set to ZC. The right dataset shows a simulation of the experimental situation.

again via an exchange of electrons with the tip. Due to the increased tunneling probability when the tip is in close proximity of the molecule, this neutralization tends (depending on the bias voltage, see also fig. 7.10 later in this chapter) to occur at the bottom turning point of the oscillation.

To further understand the involved charge transfer processes responsible for the observed damping signals, a simulation of the experimental situation was performed in collaboration with Lisanne Sellies as a part of her Master Thesis [178]. The result of this simulation is shown in figure 7.5, which is based on the WKB approximation (see also section 2.1), including the additional tunneling pathways during photoexcitation, i.e. single electron photocurrents. In figure 7.5 it becomes apparent, that the simulations reproduce the experimentally obtained damping spectra very well. Due to this good agreement, it is assumed that the experimentally observed signals stem from the charging processes present in the simulations, which will be used in the interpretation of data shown later in this chapter. Furthermore, these simulations allow determining the instants in time, at which the molecule is charged and discharged, which exhibits the behavior shown in figure 7.4.

Further, the tunneling processes responsible for the damping caused by photoexcitation can be deduced, which are shown in figure 7.6 (see also section 3.4). The mechanism for photocurrent generation is depicted in a single particle picture in figure 7.6a. Here, photocurrents are generated in a two step process, starting off with the direct photoexcitation of the molecule (step 1). For the case of a positive bias voltage, this excitation is followed by the tunneling of an electron from the tip to the now only singly occupied HOMO of the molecule (step 2). This leaves the molecule in a negatively charged state, which can be neutralized by tunneling an electron from the LUMO back into the tip (step 3). While the single particle picture is well suited to judge, which orbitals are involved in which tunneling process, it does not fully encompass the energy landscape of the full system. Due to the relaxations of the molecule and the underlying substrate upon charging, a many-body picture including these relaxation energies is more suitable, which is shown in figure 7.6b. Here, the same steps of the process described above are shown, where two additional features become apparent. Firstly, the relaxation energies for the neutral (E_{rel0}) and the negatively charged molecule ($E_{\mathrm{rel-}}$) are included. Here, the bias is adjusted such that the neutralization of the molecule can occur via an electron tunneling from molecule to tip, but also such that the energy of the negatively charged state is only slightly higher than the energy of the vibrationally excited neutral state. This implies, that the transition probability in this case is comparatively low, which leads to the situation described in figure 7.4, where discharging of the molecule occurs only when the tip is close to the molecule. The second observation is that for this bias voltage, the positively charged state of the molecule can not be accessed, since it is higher in energy than the optically excited state. This implies, that the generated photocurrent can only leave the molecule in a negatively charged state for a positive bias, leading to the aforementioned order of tunneling processes, namely that the HOMO of the molecule is refilled and the molecule is neutralized by an electron tunneling out of

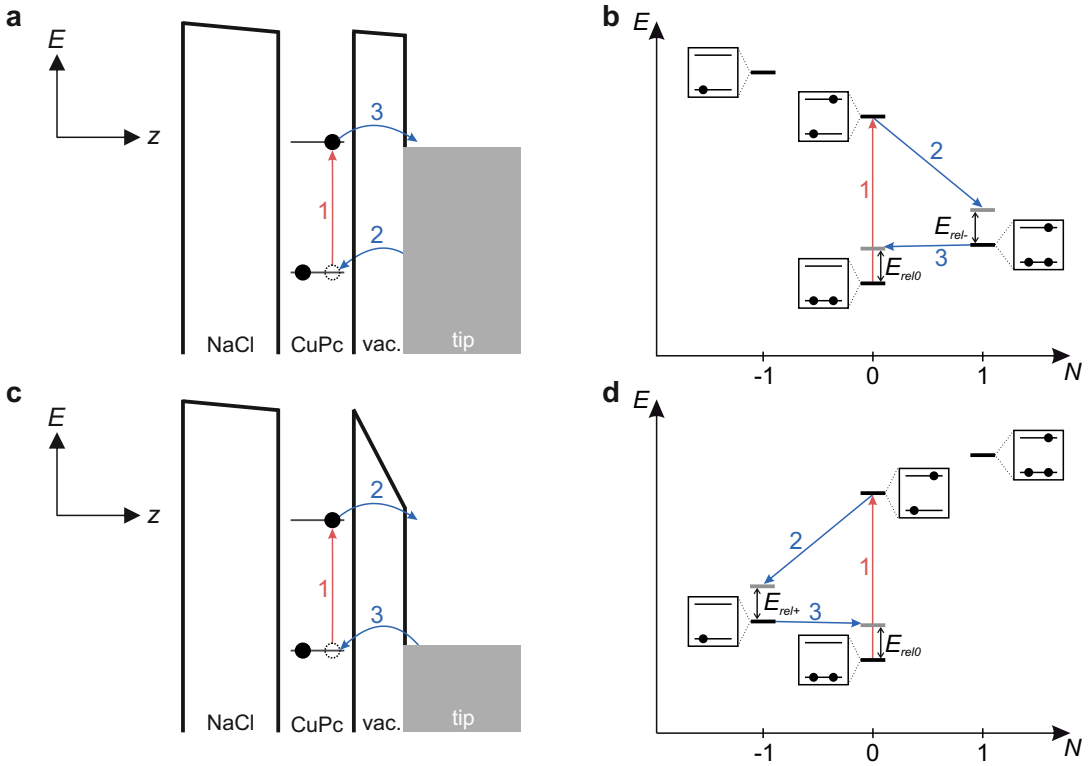

Figure 7.6: Tunneling processes for different bias voltages in single electron photocurrent generation. **a**, **b**, Tunneling processes in the single particle (**a**) and in the many-body picture (**b**) for a positive bias voltage. Here, the photocurrent consists of an electron refilling the hole in the HOMO of the molecule, while neutralization of the molecule is mediated by electron tunneling from the LUMO. **c**, **d**, Tunneling processes in the single particle (**c**) and in the many-body picture (**d**) for a negative bias voltage. In this case, the photocurrent is manifested by an electron tunneling from the LUMO to the tip, while neutralization takes place via refilling of the HOMO.

the LUMO.

A similar situation presents itself when applying a negative bias voltage, as shown in figures 7.6c and d. Here, the photoexcited electron from the LUMO is extracted first and the charged molecule is successively neutralized by refilling the HOMO. Again, this is the only possible relaxation path, since the negatively charged state is higher in energy, and can thus not be accessed after photoexcitation.

7.5 Single Electron Photocurrent Mapping

In the previous section it was presented that a CuPc molecule situated on thick NaCl on Cu(111) can be photoexcited directly by coupling a pulsed laser system to the SPM junction. Following the direct photoexcitation of the molecule, single electrons

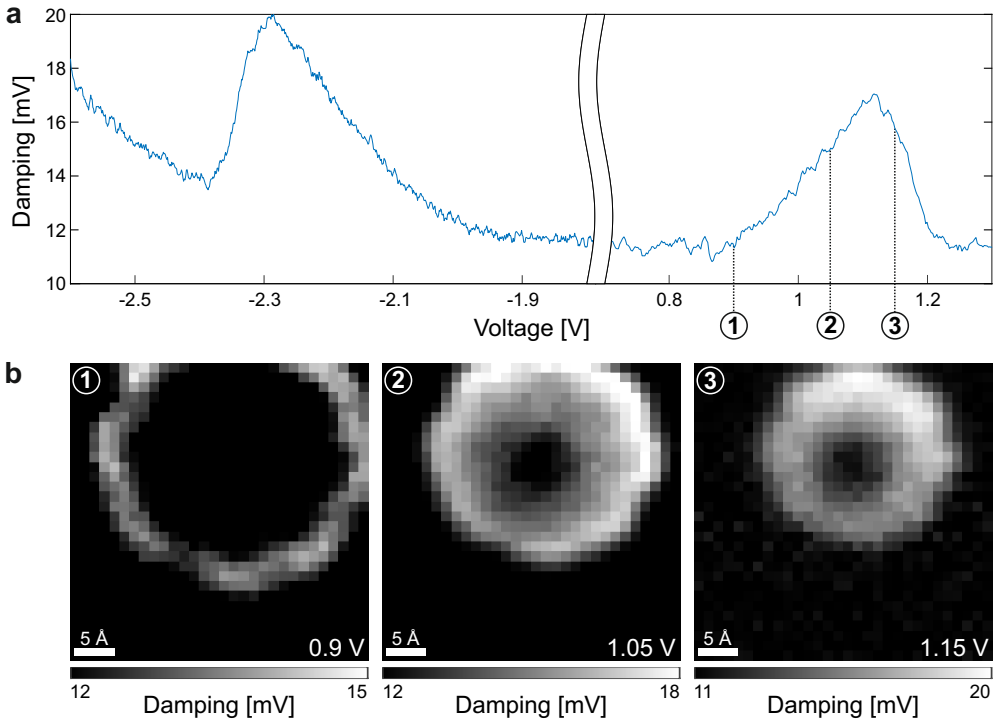

Figure 7.7: Mapping photocurrents at different bias voltages. **a**, Damping spectra for a single CuPc at negative and positive bias voltages. Experimental parameters: Setpoint: 1 mV, 1.75 Hz; AFM amplitude: 2 Å; CW laser power: 4.78 mW, pulses set to ZC; $\Delta z = 0.9$ Å. **b**, Constant height damping images obtained at the voltages indicated in **a**. The same experimental parameters were used as stated in **a**.

can be added to or removed from the excited molecule in the form of photocurrents. By applying a suitable bias voltage, the molecule can be neutralized in the same cantilever cycle leading to a damping of the cantilever oscillation.

Since these photocurrents yield insights into the electronic structure of the excited state of the molecule, mapping these currents might provide valuable information on the behavior of optically excited states. The spectra depicted in figure 7.7a show typical signals for photocurrents is obtained for both negative and positive bias voltages. It should be noted, that the overall increase of the damping for large negative bias voltages was also present in the absence of a laser and is not an effect of direct photoexcitation.

Recording constant height maps of the observed damping signal at the bias voltages indicated in figure 7.7a yields the images shown in figure 7.7b. While only images obtained at positive bias voltages are discussed here, a similar behavior is observed for negative bias voltages as well [178]. For small, positive bias voltages (image 1 in figure 7.7b) a large, ring-like contrast is observed at the periphery of the molecule. This is attributed to the fast discharging of the molecule for this bias voltage. Recalling the process discussed in figure 7.4, the neutralization of the molecule is governed by an

electron tunneling from the charged molecule to the tip. For these low bias voltages, the molecule immediately discharges after charging via photocurrents, which causes no dissipation to be observed when the tip is close to the molecule. Moving the tip laterally away from the molecule, however, will reduce the tunneling rate between the charged molecule and the tip, which leaves the molecule in its charged state long enough for a damping signal to be observed. This hypothesis is underlined when examining the contrast for higher bias voltages, for example image 2 in figure 7.7b. While the bright outline is still visible, additional signal starts to appear in the center of the molecule. This is likely due to the reduced discharging rate of the molecule for this bias voltage, leaving it charged long enough for dissipation to be observed. Finally, for large bias voltages (image 3 in figure 7.7b), the constant height image exhibits a circular shape with a significant depression in the center, the origins of which will be discussed later (see figure 7.9b).

While the photocurrent maps shown in figure 7.7b can be explained by the model described earlier in this chapter, the observed contrast does not agree with the photocurrent maps obtained in other research [76]. As the single electron photocurrents observed in this experiment are facilitated by tunneling from the excited state LUMO (in the case of negative bias, see figure 7.6c) or an electron tunneling into the excited state HOMO (in the case of positive bias, see figure 7.7a), the photocurrent maps are expected to resemble the contrast of these orbitals in the respective experimental setting. The discrepancy with the results shown in ref. [76] is attributed to the varying cantilever height at the moment of discharging, which is also supported by the simulations shown in 7.8. These simulations reveal that, if the tip is positioned directly over the molecule, the discharging of the molecule can occur at different heights for one given bias voltage. In the case of negative bias voltages, for example, the neutralization of the molecule is facilitated by an electron tunneling from the tip to the HOMO. Since this is a probabilistic event, the exact time and thus the precise cantilever position at which this occurs may vary for each cycle. As this directly affects duration for which the molecule is charged, this also influences the measured dissipation. This effect is exacerbated by the voltage drop between molecule and tip (indicated in blue in figure 7.8). As the cantilever motion is changing the instantaneous fraction of the applied bias voltage between tip and molecule [113], the discharging probability is further influenced by the cantilever motion.

Another important observation is that charging and discharging occurs by tunneling from and to different orbitals, which is in contrast to AC-STM, which shuttles electrons between tip and one selected molecular orbital. In the case shown in 7.8, a photoexcited electron is extracted from the LUMO, whereas the successive discharging is facilitated by refilling the HOMO (see also 7.6c). This means, that the damping observed in figure 7.7 depends on the tunneling rate between tip and both LUMO and HOMO at different tip-molecule distances, which further complicates the interpretation of the observed contrast.

While the latter problem will be approached later in this chapter, the former can be addressed by changing the bias voltage used in this experiment. By setting the

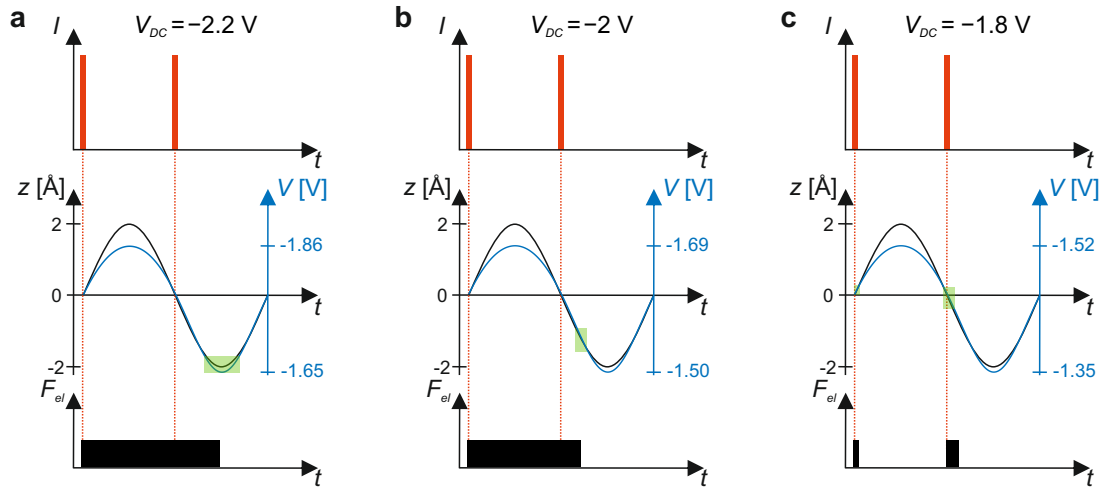

Figure 7.8: Simulation of the discharging position. **a**, Charging and discharging process during a single cantilever oscillation for a bias voltage of $V_{\mathrm{DC}} = -2.2\,\mathrm{V}$. The center graph shows the oscillation as well as the part of the bias voltage dropping between tip and molecule. The tip position at which discharging occurs is marked in green. The same graphs are shown for a bias voltage of $V_{\mathrm{DC}} = -2\,\mathrm{V}$ (**b**) and $V_{\mathrm{DC}} = -1.8\,\mathrm{V}$ (**c**).

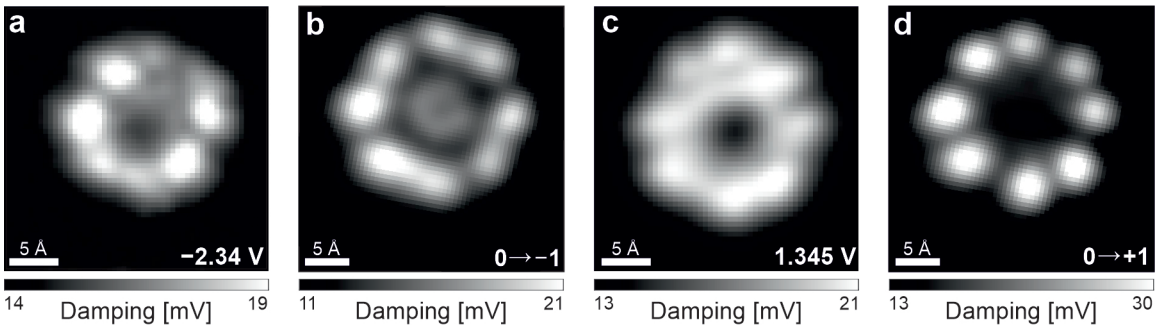

Figure 7.9: Comparison of photocurrent maps to AC-STM images. **a**, Photocurrent map obtained at negative bias voltages. **b**, AC-STM image of the $0 \rightarrow -1$ transition of CuPc. The image was rotated to match the orientation of the molecule shown in **a**. **c**, Photocurrent map obtained at positive bias voltages. **b**, AC-STM image of the $0 \rightarrow +1$ transition of CuPc. The image was rotated to match the orientation of the molecule shown in **c**. Experimental parameters: **a** & **c**: CW laser power: 2.43 mW, pulses at ZC; setpoint: 1 mV, 1.75 Hz; $\Delta z = 0.9\,\text{Å}$ (**a**) and $\Delta z = 1.5\,\text{Å}$ (**c**). For **b** & **d**: see figure 7.2.

bias voltage to be as close to the charging hysteresis as possible, the discharging can be ensured to occur only at the bottom turning point of the cantilever motion (see fig. 7.8a). Constant height photocurrent maps for these experimental settings are shown in figures 7.9a and c. Comparing these to the maps shown in 7.7b, features on the sub-molecular scale can are now observed. In the case of negative bias voltages (figure 7.9a), the contrast is expected to originate from the excited state LUMO as discussed earlier, an AC-STM image of which is shown in figure 7.9b. While there is an overall resemblance between these two images, the photocurrent image exhibits four bright features which are not present in the AC-STM image, the origins of which have thus far remained elusive. Additionally, the image shown in figure 7.9a does not exhibit the characteristic nodal planes present in figure 7.9b. For the photocurrent map observed at positive bias voltages (fig. 7.9c), the situation appears similar to the case at negative bias voltage. While the observed contrast resembles the expected orbital, in this case the HOMO as shown in the AC-STM image in figure 7.9d, a clear nodal plane structure could not be observed. However, the eight lobes located at the periphery of the molecule strongly hint towards a contribution of the HOMO to the observed signal.

These first photocurrent maps indicate, that it is indeed possible to access and image the excited state orbitals of a single CuPc on a thick insulating film. The difference in contrast to the expected orbitals can be attributed to the nature of the discharging process as described above. Since the exact point of discharging during the cantilever oscillation and thus the observed dissipation is dependent on the tunneling rate between HOMO (negative bias voltage) or LUMO (positive bias voltage), respectively, the overall contrast might still be influenced by these orbitals. This would lead to a contribution of both LUMO and HOMO to the contrast, which would result in a blurred image and thus explain the differences between the observed and expected contrast.

Nevertheless, the photocurrent maps shown in figures 7.9 and 7.7b also confirm that indeed direct photoexcitation of the molecule is responsible for the observed damping signal. Every photocurrent map, irrespective of bias voltage, features a depression in the center above the molecule. This behavior has also been observed in STM-induced luminescence experiments performed on phthalocyanine molecules [41, 53, 182] and is attributed to the coupling of the molecular dipole to the electric field emanating from the tip. As depicted in figure 7.10a, the molecular dipole of phthalocyanine molecules lies inside the molecular plane. This implies, that it can only couple to electric field components perpendicular to the tip which could cause a subsequent photoexcitation. If the tip is positioned above the center of the molecule, the electric field caused by the laser does not exhibit components perpendicular to the tip and can not couple to the molecular dipole and excite the molecule, as indicated in figure 7.10a. This further underlines the observed signals to be originating from single electron photocurrent generation.

Another observation further corroborating this interpretation is the polarization dependence of the damping signal as shown in figure 7.10b. Here, the damping signal

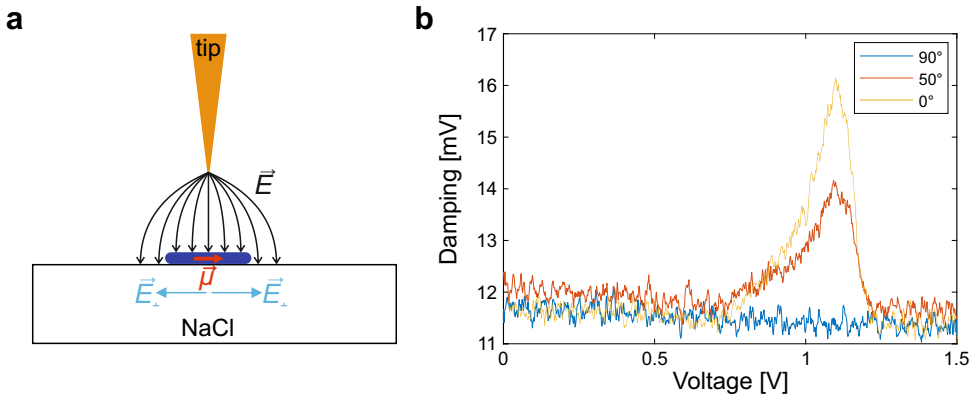

Figure 7.10: Dipole coupling and polarization dependence of the photocurrent signal. a, Sketch of the molecular dipole coupling to the electric field generated by the laser pulse. Due to the in-plane orientation of the molecular dipole it can only be excited by the electric field component perpendicular to the tip. **b**, Polarization dependence of the damping signal. The given angles describe the rotation angle of the polarization with respect to the tip.

vanishes completely when the laser polarization is changed to be perpendicular to the tip. Similar to the situation described in chapter 6, the field enhancement is largest when the laser is polarized parallel to the tip [168], resulting in a sufficient photoexcitation probability and subsequent photocurrent generation. This is also an indication, that the observed signal is indeed due to photocurrents generated by the direct excitation of the molecule.

7.6 Combination of Photocurrent Mapping and AC-STM

As stated in the previous section, generating single electron photocurrents from individual CuPc molecules on thick NaCl/Cu(111) is indeed possible. The obtained contrast in the photocurrent maps, however, does not correspond to the expectations following from the simulations and other experiments [76]. As discussed above, the contrast appears to be influenced by the neutralization process, leading to an admixture of contrast originating from other orbitals of the molecule to the excited state orbital contrast. This is attributed to the probabilistic nature of the tunneling neutralization of the molecule.

In this section, a method is proposed to circumvent these issues. By employing voltage pulses in a scheme similar to AC-STM, it should be possible to deliberately control the exact discharging time and thus reduce the influence of the orbital involved in the neutralization of the molecule. The proposed scheme is depicted in figure 7.11a, which shows the combination of laser and AC voltage pulses. While the laser pulses

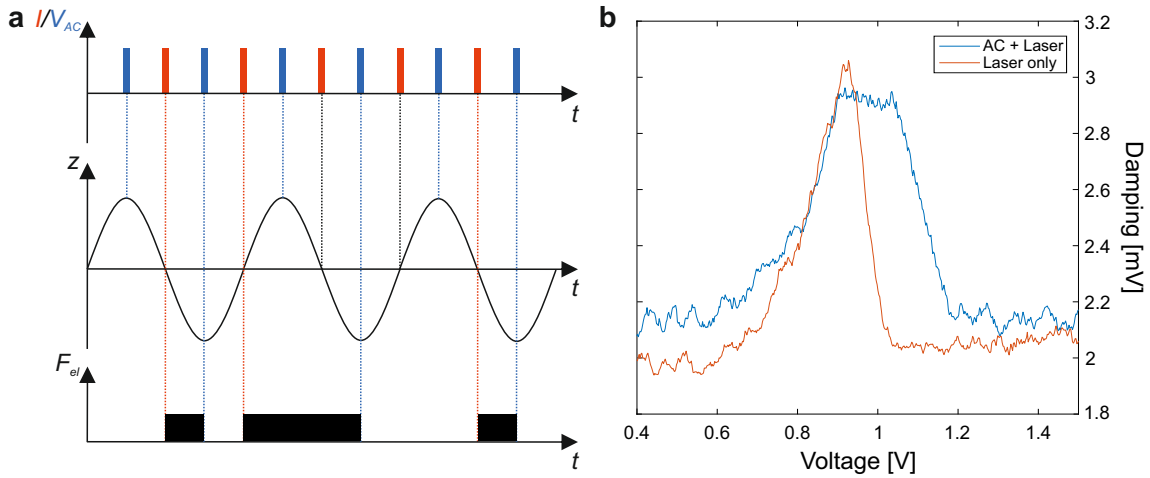

Figure 7.11: Combination of voltage and laser pulses. a, Combined laser and voltage pulse scheme. The laser pulses are adjusted to occur at the ZC of the cantilever oscillation, while the voltage pulses are set to the TA points. This allows for a well-defined neutralization of the molecule. **b**, Damping spectra with and without implementation of AC voltage pulses. The red curve shows dissipation originating from photocurrent and random discharging, whereas the blue curve shows the signal obtained for both laser and AC voltage pulses being coupled to the junction. Experimental parameters: AFM amplitude: 2 Å; CW laser power: 8.5 mW; $V_{\mathrm{AC}} = 1\,\mathrm{V_{pp}}$.

fulfill the same role as above, namely the generation of photocurrents, the voltage pulses are used to discharge the molecule at the bottom turning point of the cantilever oscillation. Using these pulses allows experiments to be performed at higher DC bias voltages, similar to the case of AC-STM. The voltage pulses are used to discharge the molecule in the bistable hysteresis window, which prevents neutralizing the molecules via probabilistic tunneling neutralization. This causes discharging to not only occur at a specific tip height, but also can reduce the influence of the molecular orbital through which neutralization takes place.

Two damping spectra are shown in figure 7.11b, where both cases, namely damping due to photocurrent with and without the implementation of voltage pulses to facilitate the discharging of the molecule, are shown. While the spectrum without voltage pulses is similar to the ones depicted previously and exhibits the same sharp drop when approaching the charging hysteresis, implementing voltage pulses to discharge the molecule causes a broadening of the damping signal to higher DC bias voltages. This observation is in line with the aforementioned hypothesis, that the voltage pulses permit dissipation also to be detected in the bistable window of the hysteresis.

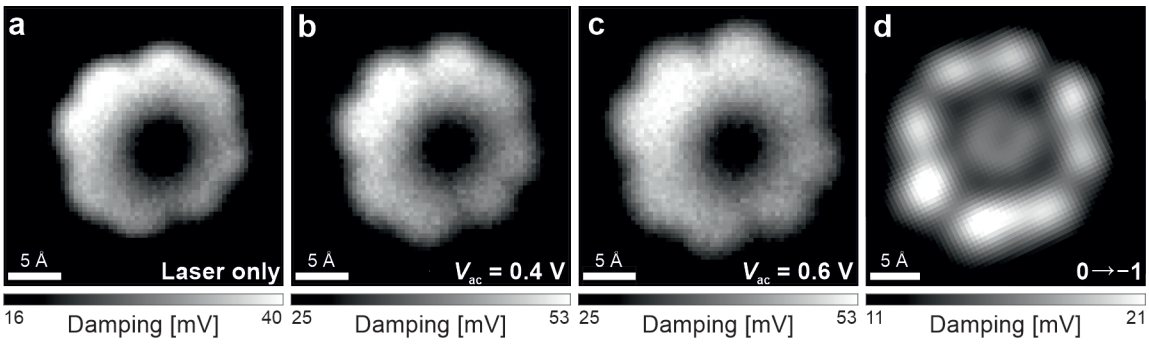

Figure 7.12: Photocurrent maps for different AC pulse voltage. a-c, Constant height damping images for increasing AC pulse voltage. Comparing the maps for 400 mV (**b**) and 600 mV (**c**) to the map obtained without voltage pulses (**a**), photocurrent induced damping can be observed over a larger area above the molecule. **d**, AC-STM image of the $0 \rightarrow -1$ transition of CuPc. The image was rotated to match the orientation of the molecule shown in **a-c**. Experimental parameters: **a-c**: AFM amplitude: 2 Å; Setpoint: 1 mV, 1.2 Hz; $\Delta z = 2$ Å; $V_{\mathrm{DC}} = -2.29$ V; CW laser power: 4.78 mW, pulses set to ZC; **d**: see figure 7.2.

The influence of using voltage pulses to discharge the molecule on the photocurrent maps is shown in figure 7.12. Figure 7.12a shows a photocurrent map for negative bias obtained without voltage pulses, exhibiting the same characteristic features as shown above, namely the absence of signal in the molecular center and an outline resembling the LUMO of the molecule (see figure 7.12d). Using voltage pulses to discharge the molecule results in an increase of the size of the observed features (figures 7.12b and c). This is attributed to a reduced influence of the tip position when discharging the molecule as an effect of the voltage pulses. Since these assist in the neutralization of the molecule, the dependence of the overlap with the orbital, through which discharging is facilitated, appears to be reduced. Despite these improvements, the overall photocurrent maps do not exhibit any contrast within the orbital. This would expected, as the photocurrent-induced charging should predominantly dependent on the tunneling rate between the excited state orbital and the tip, which would be the LUMO in the case shown in figure 7.12. One possible explanation for this behavior would be the saturation of the aforementioned tunneling rate. It has been shown in a recent experiment by Kaiser *et al.* [173] on thin insulating films, that the saturation of the tunneling current through a molecular orbital can lead to a flattening of the observed contrast, similar to the one shown in figure 7.12c. Here, this might be due to the formation of a long-lived excited state, which would lead to photocurrent generation at various tip heights and thus reduce the dependence on the tunneling rate between the excited state orbital and the tip and blur the contrast accordingly.

7.7 Photocurrent Maps of a Molecule with Lifted LUMO Degeneracy

As was discussed in the previous section, voltage pulses can be used to reduce the influence of the discharging process on the photocurrent maps. Sub-molecular features indicating an imaging of the excited state orbital, however, were not yet observed. To this end, experiments on a molecule were conducted, which exhibited a lifted degeneracy for the two LUMO orbitals. While it is known that this degeneracy can be lifted by charging [51, 99], the results presented here show the degeneracy being lifted by environmental effects.

A constant Δf image is shown in figure 7.13a, which depicts the molecule investigated here indicated by a red circle. An AC-STM image of the $0 \rightarrow -1$ transition,

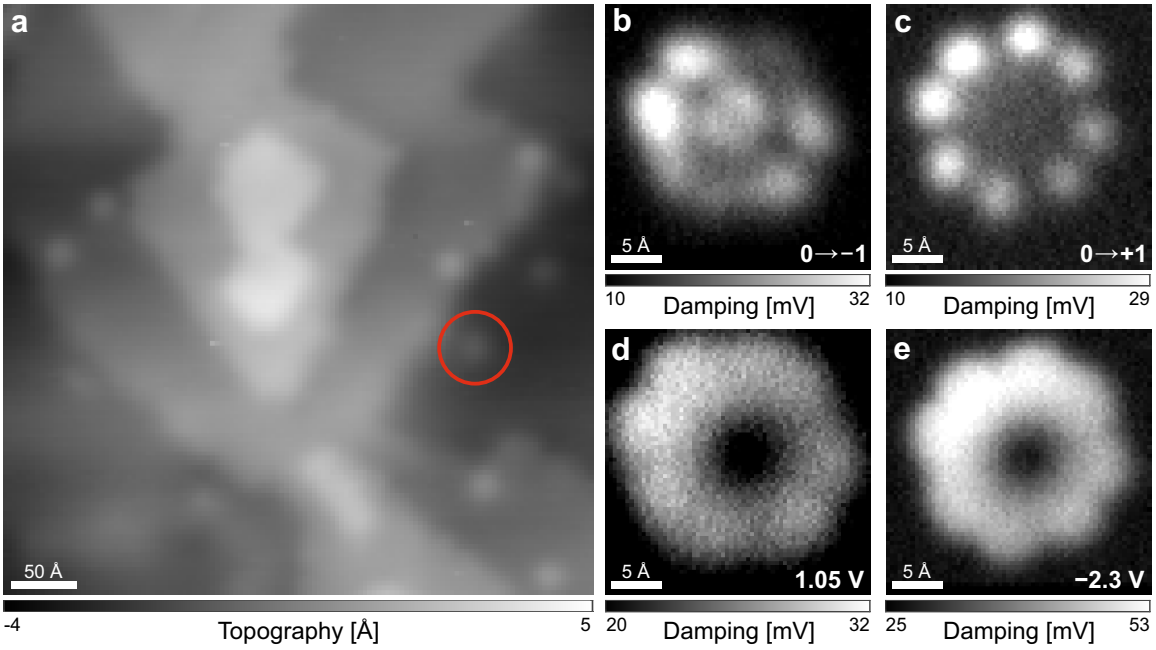

Figure 7.13: Photocurrent maps of a molecule located close to a NaCl step edge. **a**, Constant Δf overview. The CuPc molecule shown in **b-e** is marked by a red circle. Setpoint: 1 mV, 1.3 Hz. **b**, **c** AC-STM images of the $0 \rightarrow -1$ (**b**) and the $0 \rightarrow +1$ (**c**) charging transitions. The $0 \rightarrow -1$ transition exhibits reduced symmetry due to the interaction with the nearby step edge. **d**, **e** Photocurrent maps of the molecule shown in **b**& **c** for positive (**d**) and negative (**e**) bias voltage. Experimental parameters: **b**: AFM amplitude: 1 Å; Setpoint: 1 mV, 1.5 Hz; $\Delta z = 2.6$ Å; $V_{\mathrm{DC}} = 1.02$ V; $V_{\mathrm{AC}} = 1.4\,V_{\mathrm{pp}}$. **c** AFM amplitude: 1 Å; Setpoint: 1 mV, 1.5 Hz; $\Delta z = 1.8$ Å; $V_{\mathrm{DC}} = -2.475$ V; $V_{\mathrm{AC}} = 1.4\,V_{\mathrm{pp}}$. **d** AFM amplitude: 2 Å; CW laser power: 4.78 mW, pulses set to ZC; Setpoint: 1 mV, 1.2 Hz; $\Delta z = 3.5$ Å; $V_{\mathrm{AC}} = 1.4\,V_{\mathrm{pp}}$. **e** AFM amplitude: 3 Å; CW laser power: 4.78 mW, pulses set to ZC; Setpoint: 1 mV, 1.2 Hz; $\Delta z = 1.8$ Å; $V_{\mathrm{AC}} = 1\,V_{\mathrm{pp}}$

as shown in figure 7.13b, reveals, that the degeneracy of the LUMOs is lifted. On the one hand, this becomes apparent by comparing the observed contrast to images obtained for the $-1 \rightarrow 0$ transition, where the degeneracy is lifted by the Jahn-Teller effect [99], which agrees very well with the image obtained here. On the other hand, taking the contrast for the $0 \rightarrow +1$ transition into account, it is revealed that the reduced symmetry observed in figure 7.13b is not due to a change in adsorption geometry, as the AC-STM image shown in figure 7.13c exhibits the same contrast as an unperturbed molecule as shown in figure 7.2c. Since these two orbitals now exhibit entirely different symmetry, it would be expected that this is also translated to the contrast observed via photocurrent-induced charging of the molecule.

Photocurrent maps for positive and negative are shown in figures 7.13d and e. Here, neutralization of the molecule was again assisted by voltage pulses in order to reduce the influence of the coupling between the tip and the orbital through which discharging is facilitated. While these maps again show features following the outline of the orbital with a flattened contrast, the photocurrent map obtained for positive bias voltages (figure 7.13d) appears to exhibit a reduced symmetry, which hints towards a stronger involvement of the LUMO than the HOMO. Following the previously discussed interpretation of the process, photocurrent-induced charging is taking place via the HOMO, while the neutralization is facilitated by electron transfer from the LUMO to the tip. This indicates, that despite the implementation of voltage pulses to discharge the molecule, the contrast still depends on the coupling between tip and orbital for the set of parameters used here.

7.8 Photocurrent Maps of a CuPc/Pentacene Dimer

In order to further test the capabilities of photocurrent generation, pentacene molecules were added to the sample. Since these molecules are known to exhibit a larger optical gap [183, 184], the laser used for the excitation should not be able to excite the molecule. At the same time, pentacene has been reported to exhibit singlet fission [185–187], a process where the optically excited singlet state dissociates into two triplet states, which has garnered significant interest in recent years and would be an interesting process to investigate with this technique. In this section, pentacene as well as a CuPc/pentacene dimer will be examined.

KPFS and AC-STM data on a single pentacene molecule is shown in figure 7.14. The spectra shown in figure 7.14a reveal two clear charging hysteresis around $-2.59\,\mathrm{V}$ and $1.8\,\mathrm{V}$. Comparing these values to the ones obtained for an isolated CuPc molecule ($-2.3\,\mathrm{V}$ and $1.25\,\mathrm{V}$, see figures 7.1c and 7.5) it becomes apparent, that the charging and discharging of pentacene takes place at higher absolute values of the bias voltage. Figures 7.14b and c show AC-STM images of the $0 \rightarrow +1$ and $0 \rightarrow -1$ transitions respectively, which match exactly with the ones reported in ref. [99].

As expected, no signal was observed while the laser was illuminating the junction for an individual pentacene molecule, which is due to the mismatch of the optical gap

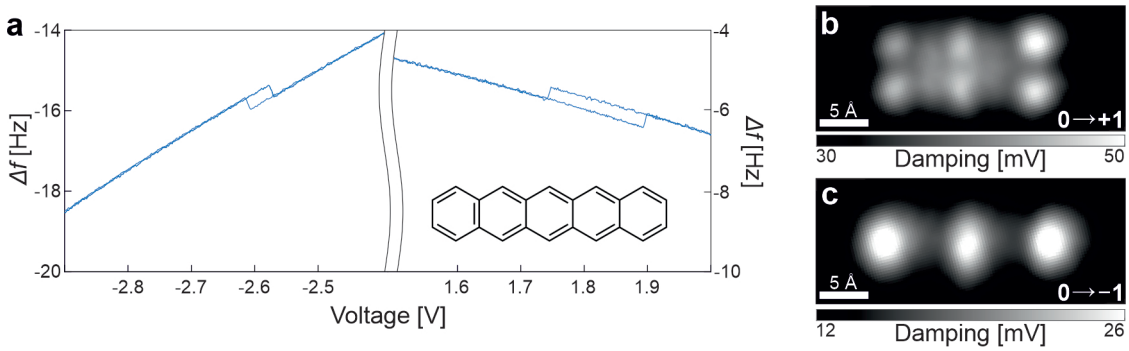

Figure 7.14: Pentacene on thick NaCl on Cu(111). **a**, $\Delta f(V)$ spectra on pentacene on thick NaCl on Cu(111). Both positive and negative charging transitions are shown. Inset: Chemical structure of pentacene. **b**, **c** AC-STM images of the $0 \rightarrow +1$ (**b**) and $0 \rightarrow -1$ transitions of pentacene. Experimental parameters: **a**: Setpoint: 1 mV, 2.2 Hz; $\Delta z = 2$ Å (pos. bias), $\Delta z = 1$ Å (neg. bias); **b**, **c**: AFM amplitude: 1 Å; Setpoint: 1 mV, 2.2 Hz; $\Delta z = 1.8$ Å (**b**), $\Delta z = 3.3$ Å (**c**); $V_{\mathrm{DC}} = -2.69$ V (**b**), $V_{\mathrm{DC}} = 1.87$ V (**c**); $V_{\mathrm{AC}} = 1.6\,V_{\mathrm{pp}}$.

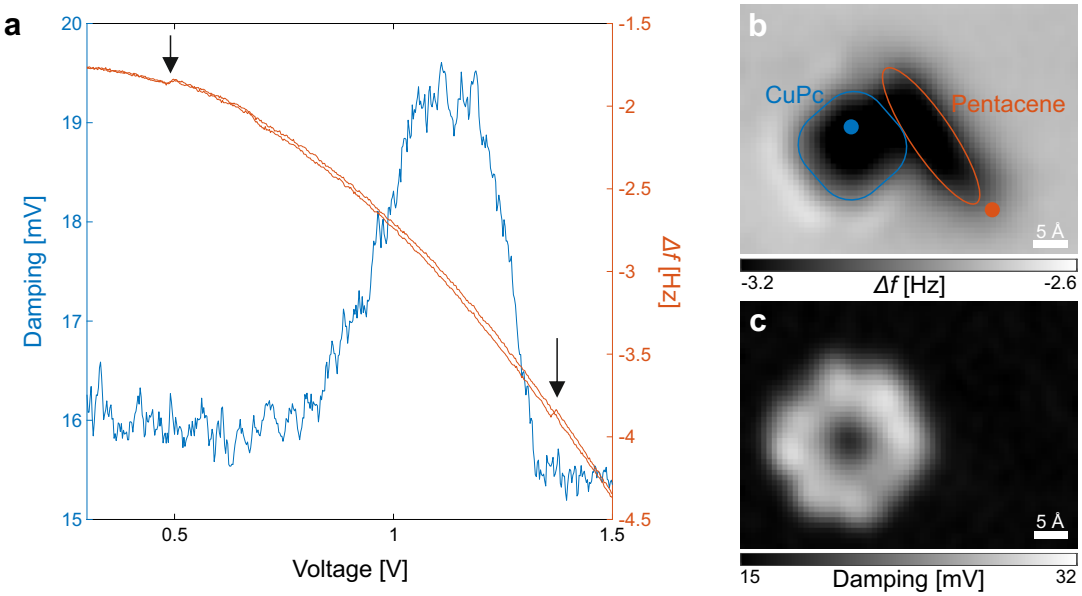

Figure 7.15: Photoinduced charging and photocurrent map of a CuPc/pentacene dimer. **a** Damping spectrum taken over CuPc (blue curve) and Δf spectrum taken over the pentacene molecule. No dissipation was observed while the tip was positioned above the pentacene molecule. The positions, where the spectra were obtained are marked in **b**. **b**, **c**, Constant height Δf image (**b**) and simultaneously recorded photocurrent map (**c**). The positions of the molecules in the dimer are indicated in **b**. Experimental parameters: AFM amplitude: 2 Å; CW laser power: 3.19 mW, laser pulses set to ZC; setpoint: 1 mV, 1.6 Hz; $\Delta z = 1.5$ Å; **b**, **c**: $V_{\mathrm{DC}} = 1.12$ V.

of the molecule ($\approx 2.3\,\mathrm{eV}$ [183, 184]) with the excitation energy of the laser ($\approx 1.9\,\mathrm{eV}$, see chapter 6). Another interesting phenomenon to explore in this situation, however, would be resonant energy transfer (see e.g. ref. [49]) between the two different molecules. Damping and Δf spectra for a CuPc/pentacene dimer are shown in figure 7.15a, which were taken at different positions above the dimer. While there is a strong damping signal when the tip is positioned over the CuPc molecule (as indicated by the dots in figure 7.15b), no dissipation was observed when the tip was positioned above the pentacene molecule. Instead, discrete charging steps are observed in Δf (arrows in figure 7.15a), which are both attributed to CuPc charging because of the low voltage at which those steps are observed. No charging of the pentacene molecule was recorded over the bias range of $-3\,\mathrm{V}$ to $2.2\,\mathrm{V}$, which might be due to the charged CuPc in close proximity to the pentacene. Since the CuPc is charged already for lower bias voltage, the additional electron might increase the energy required to charge the adjacent pentacene molecule due to Coulomb interaction.

This behavior is also revealed in the simultaneously recorded Δf image and photocurrent map, shown in figures 7.15b and c. While both molecules are clearly visible in the Δf image, there is no photocurrent observed for the pentacene, while the contrast originating from the CuPc remains unchanged when compared to the maps shown previously. The lack of photocurrent for the pentacene molecule is attributed to two factors: On the one hand, the laser can not directly excite the pentacene molecule, leading to a lack of photocurrent generation. On the other hand, no resonant energy transfer can take place from CuPc to the pentacene. This becomes apparent when comparing the voltages necessary for charging the CuPc (see figure 7.1c) and pentacene (see figure 7.14a) respectively. Here it is revealed, that the energy required to charge pentacene is larger for negative as well as positive bias voltages than for CuPc. This implies, that both charged states for pentacene are higher in energy than the charge states for CuPc, which means that energy transfer from CuPc to pentacene is energetically unfavorable.

While it was not possible to show resonant energy transfer in this case due to the energetic alignment of the respective charge states for CuPc and pentacene, this experiment further underlines the origin of the observed photocurrent signals. The lack of any signal for the pentacene molecule reveals the necessity for direct photoexcitation as a prerequisite for photocurrent generation. Furthermore, it is also revealed that the study of molecular dimers is possible with this technique, where the selection of a different molecule with a more suitable energetic alignment of the charged states might yield a platform to study the effects of exciton transfer between different molecular species.

7.9 Summary & Outlook

In this chapter we have demonstrated the generation and mapping of single electron photocurrents from an individual CuPc molecule. By depositing these molecules on a

thick NaCl layer grown on Cu(111), the charged states of the molecule are stabilized and can be controlled via the bias voltage applied to the junction. Synchronizing a pulsed laser excitation of the molecule to the cantilever oscillation, we were able to generate single electron photocurrents and neutralize the molecule in the same cantilever oscillation cycle, leading to a measurable damping of the AFM cantilever. First maps of these single electron photocurrents bear similarities with the the excited state orbitals of the molecule and constitute a first step towards the direct mapping of molecular excited state orbitals at the atomic scale. In particular, the following was demonstrated:

- As a first step, the CuPc molecules were studied with KPFS and AC-STM. This reveals the required energies for charging and the electronic states of the molecule, to which the later obtained photocurrent signals and maps were compared.
- By employing laser pulses synchronized with the AFM cantilever oscillation (see also chapter 6), we were able to generate single electron photocurrents from individual CuPc molecules. Due to the thick insulating layer decoupling the molecule from the conductive substrate, removing a single electron from or adding an electron to the molecule leaves it in a defined charge state. This behavior was first detected in jumps in the frequency shift, indicating changes in the charge state of the molecule. By increasing the laser power coupled to the junction we were able to charge and discharge the molecule in the same cycle of the cantilever oscillation, leading to a measurable damping of the AFM cantilever.
- We employed a simulation in order to explore the origins of the observed damping signal. Here, we found that the molecule is charged by a single electron photocurrent at the zero crossing and discharged via a random tunneling at the bottom turnaround point of the cantilever oscillation, depending on the applied bias voltage. Based on these observations and the energy landscape, we deduced a three step process responsible for the damping signal, which includes the direct photoexcitation of the molecule, the tunneling of an electron from the excited state orbital and the neutralization of the molecule via charge exchange through a different orbital.
- Mapping these photocurrents reveals a strong dependence of the contrast on the applied DC bias voltage. This is attributed to the influence of the discharging process, which is more efficient when the bias voltage is significantly lower than the charging hysteresis of the molecule. This behavior is also confirmed by the simulations, indicating a strong dependence on the molecular orbital through which discharging is facilitated.
- Photocurrent maps obtained close to the charging hysteresis reveal two significant features. Firstly, the contrast revealed by these maps follows the outline of the molecular orbitals, suggesting that the origin of these photocurrents is linked to the excited state orbitals of the molecule. Secondly, the photocurrent

maps exhibit an absence of the signal in the center of the molecule, which is linked to the coupling of the molecular dipole to the electric field of the laser [41, 53, 182]. This observation further proves the involvement of direct photoexcitation as the cause of the observed signals, which is further underlined by the polarization dependence of the damping signal.

- In order to reduce the influence of the orbital through which discharging is facilitated, we employed voltage pulses to control the exact point during the cantilever oscillation at which the molecule is neutralized. While this appeared to have the intended effect as evident by a change in the contrast observed in the photocurrent maps, we were not able to resolve orbital features such as nodal planes, which might be due to a saturation of the generated photocurrent.
- Investigating a molecule situated close to a step edge revealed, that the degeneracy of the LUMOs was lifted due to environmental effects. Mapping the photocurrents for this molecule revealed that, despite the implementation of voltage pulses, the discharging process still influenced the contrast.
- As a last step, we investigated a CuPc/pentacene dimer, which only showed photocurrent generation above the CuPc molecule, while no effects of photoexcitation could be found for pentacene. This further underlines the observed phenomena to be based on direct photoexcitation and demonstrates the possibility of studying molecular heterostructures.

While the results presented in this chapter reveal that single electron photocurrent generation via direct photoexcitation at the molecular scale is possible, there are some points which require further analysis. For example, the flattening of the contrast for the photocurrent maps when combining laser-induced charging with neutralization via implementation of voltage pulses at the bottom turning point of the cantilever oscillation remains unclear. While recent research by Kaiser *et al.* observe a similar flattening of a molecular orbital when the tunneling rate between tip and molecule is saturated, the situation in the case presented here might be different. Since we can control the tip-molecule distance when photoexcitation takes place, we are able to reduce the tunneling rate from the photoexcited state to the tip. However, we found that even for large AFM amplitudes (and thus tip-molecule distances during photoexcitation), the orbital contrast remained flat. As stated earlier, we attributed the flattening to a long-lived state of CuPc, through which the molecule would be able to be charged at times when no laser is present, possibly leading to this flattening of the contrast.

A second observation, which has thus far remained unclear, is that the influence of the orbital through which discharging takes place is still observable even when employing voltage pulses to facilitate the neutralization of the molecule (see fig. 7.13). Since discharging takes place at the bottom turning point of the oscillation, the tip-molecule distance is significantly reduced, while the voltage pulses simultaneously enhance the tunneling probability even further. The influence of the neutralization process on the contrast, however, could probably be reduced by adjusting the reset

pulse voltage to increase the discharging rate.

Besides these issues, the technique presented in this chapter provides a robust method to study single electron photocurrents from individual molecules and might lead to the direct examination and mapping of excited state orbitals. Currently, the experimental setup is only capable of working at a wavelength of 640 nm provided by the NPL. We envision an improvement to the optical setup by employing a tunable laser system, which would allow this technique to be applied to a wide variety of molecules and thus also permit the study of a broad range of processes, for example photosynthesis [1] or photocatalysis [188].

8 Construction of a Mid-Infrared Scanning Tunneling Microscope

This chapter presents the design and construction of a mid-infrared scanning tunneling microscope, in which several people were involved. The design of the apparatus was predominantly developed in collaboration with Christoph Rohrer and Jascha Repp. Raffael Spachtholz, Pauline Drexler, Victoria Ruckerbauer, Helena Hausfelder and Niklas Vogt contributed to the construction of the apparatus in the context of their respective Bachelor Theses [189–193]. Raffael Spachtholz continued to contribute to this project in the scope of his PhD thesis. The efforts made in this project stem from a cooperation with the group of Prof. Rupert Huber, who are advancing the laser setup, which will be used in the future operation of this apparatus.

This chapter presents the progress made on the next generation of lightwave-driven scanning tunneling microscopy, which was achieved in the context of this PhD thesis. Due to the astonishing capabilities of lightwave-driven STM [16, 20, 80, 81], progress on the instrumentation might pave the way to a direct access to various physical processes with unprecedented spatial and temporal resolution.

This shall be achieved with the newly developed equipment presented in this chapter. The design considerations will be described, which elevate this novel instrumentation from the previously reported apparatus as presented in ref. [20]. Furthermore, the construction of the scan unit will be illustrated and the results of first test measurements will be discussed.

While there are many different aspects to be explored in the design and assembly of a novel STM apparatus, the presentation in this chapter will focus on the construction of the STM scan head as well as modifications to equipment used in the preparation of samples.

8.1 Introduction

The recent advent of lightwave-driven scanning tunneling microscopy [16, 64, 74, 82] has opened the door to the direct access to observing nanoscale processes in real time with sub-Angstrom spatial resolution. With this technique not only the vertical oscillation of single molecules can be probed, as shown by Cocker *et al.* [20], but also that local, ultrafast forces can be exerted with sub-molecular precision [80], which was also discussed in chapter 5 of this thesis.

Since its inception, lightwave-driven scanning tunneling microscopy has been expanded to study various systems and atomic scale processes, such as scanning tunneling luminescence spectroscopy [194], launching of acoustic phonons [79] and the relaxation dynamics of plasmons in gold nanorods [60]. Furthermore, the technique was also used to study the THz-induced electric fields in an STM junction [81, 85] and ultrafast coherence at the atomic scale [78, 195], and to perform spectroscopy on graphene nanoribbons [83]. While these results are astonishing, the technique of lightwave-driven STM can be expanded to access even more intricate physical processes. An increase in the temporal resolution, for example, would allow observing even faster dynamics at their intrinsic length scales. These include, for example, intramolecular vibrational modes [196, 197], which take a dominant role in chemical processes and reactions. Utilizing shorter lightwave pulses might also yield control over these processes and allow deliberate, local triggering of these reactions. But not only intramolecular dynamics might be attainable with an increased temporal resolution, but also electron dynamics [198] and the physics of phase transitions [199, 200] occur at timescales just above of what is achievable with the current lightwave STM technologies. This spurs the ambition for an advancement of this technique towards faster time scales. We aim to achieve this by moving away from THz radiation and incorporating mid-infrared (MIR) laser pulses into the system. Due to their shorter wavelength, these pulses can be shortened considerably, down to the sub 50 fs range [201], where recent advances have been made to decrease the pulse duration even further [60, 202–204]. In the context of lightwave-driven STM, where the temporal resolution is determined by the field apex of the pulse (see ref. [20]), this would result in a resolution of ~ 100 attoseconds.

In order to accompany these changes to the laser system, we decided to fully redesign the STM to which the laser pulses are supplied. The necessary changes to the apparatus do not only include a complete overhaul of the scan head, but also all of the supporting UHV equipment, like the manipulator and tools for sample preparation, had to be adapted accordingly. In this chapter it will first be outlined, why these changes were necessary by explaining the status quo of the lightwave STM, which was the apparatus used for the experiments shown in refs. [20, 80, 81]. Following this discussion, the novel, fully home-built scanner design will be presented and its construction process will be illustrated. Furthermore, several select changes to the UHV equipment will be described. In the end, first test measurements on a Au(111) surface will be depicted.

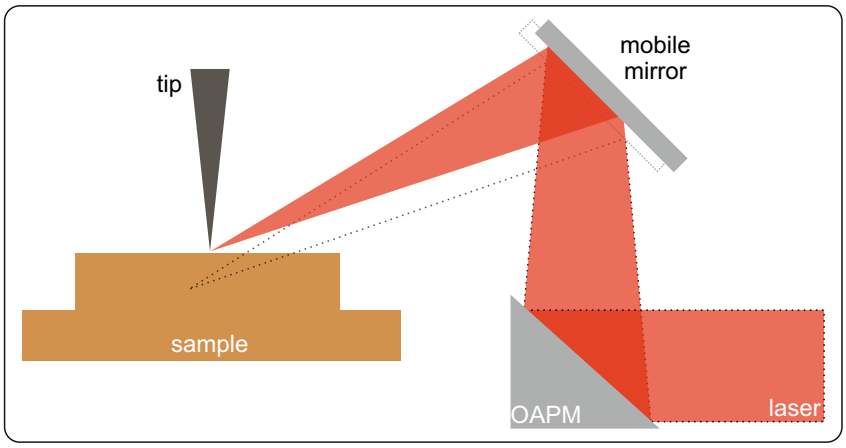

Figure 8.1: Sketch of the THz-STM laser coupling. The THz laser beam is focused on the tip-sample junction via an off-axis parabolic mirror (OAPM). The beam is deflected via a mobile mirror in order to properly align the beam. A poor alignment is indicated in the dashed beam path.

8.2 Status Quo: The THz-STM

In order to properly assess the advancements and improvements made for the newly developed MIR-STM, the general working principle of the existing THz-STM will be discussed (see also refs. [20, 80, 81]). In this regard, the arising complications and shortcomings of this design will be elaborated.

The design of the THz-STM is based on a Besocke scanner [121], where the tip is moved by three piezo tubes while the sample remains stationary and is the apparatus which was used in the experiments shown in chapter 5. Since the design of the cryostat as well as the vacuum chamber is a slightly modified version of the setup shown in chapter 4.1, these standard parts are not elaborated further here. One crucial modification, however, is the coupling of the THz laser to the tip-sample junction. Here, a proper alignment of the beam to the tip-sample junction is necessary in order to perform THz-STM experiments.

A sketch of the laser alignment is shown in figure 8.1. Here, a collimated THz laser beam is coupled into the STM chamber and directed onto an off-axis parabolic mirror (OAPM), which is mounted to the STM scan head. The beam is deflected to a mobile mirror, which is used to align the beam onto the tip-sample junction. This mirror can be moved via attached piezo driving motors. Since the optics are rigidly mounted to the scan unit, oscillations of the head with respect to the incoming laser beam will not change the focus of the beam, since this would only result in a parallel shift of the beam with respect to the OAPM. This is crucial, since the scan head is suspended with springs from the bottom of the cryostat, which results in movement of the head with respect to the laser occurring frequently.

In order to achieve proper coupling of the laser pulses to the junction, the focus

of the beam has to be as small as possible and hit the very apex of the STM tip [205, 206]. This is done via the movable, flat mirror that can be both shifted and tilted, which enables the alignment of the laser to every point on the sample. Here, however, already one issue of this construction becomes apparent: If the tip has to be repositioned after the initial laser alignment, the laser has to be realigned as well. Since the tip has to be moved quite regularly during standard STM operation due to tip crashes or in search of suitable molecules, the laser has to be realigned quite frequently. For the THz radiation used in this case, the focus diameter is on the scale of a few millimeters, and the tip can thus be moved on the scale of several micron without leaving the focus area. However, this problem is exacerbated when using mid-infrared instead of THz radiation. Due to the shorter center wavelength of the pulses, the focus diameter shrinks considerably, and thus, realignment would be necessary in this setup even after miniscule changes of the tip position. Because of this, a scan head design where the tip position is fixed with respect to the laser focus would be preferable. If the sample is moved with respect to the tip the laser remains focused on the tip while changing the scanning area.

One further improvement can be made regarding the laser pathway. As shown in figure 8.1, the laser is focused on the tip-sample junction and scattered afterwards. This scattered light, however, also yields valuable information about physical processes happening on the surface. The analysis of scattered light is already performed in different techniques, for example in tip-enhanced Raman spectroscopy (TERS) [19, 207, 208] or scanning near-field optical microscopy (SNOM) [209–212]. This is not possible in the THz-STM, since scattered light as well as light generated from the junction can not be collected and guided out of the STM chamber. This functionality shall also be incorporated in the MIR-STM to allow a broader range of experimental applications.

8.3 The MIR-STM Scan Head

The work presented in this section was performed in collaboration with Raffael Spachtholz and Pauline Drexler, who contributed in this project in the scope of their respective Bachelor's Theses [189, 190].

The scan head is the core part of every STM and the most crucial piece of the entire apparatus. Since every other piece of equipment will be designed and developed to complement the scan head, it is crucial to first understand the workings of this central part. After presenting the initial design of the scan unit, the assembly and final construction of the MIR-STM scan head will be documented.

8.3.1 Design of the Scan Head

Rendered images of the MIR-STM scan head design are shown in figure 8.2. In order to overcome the shortcomings described in the previous section, the design of the

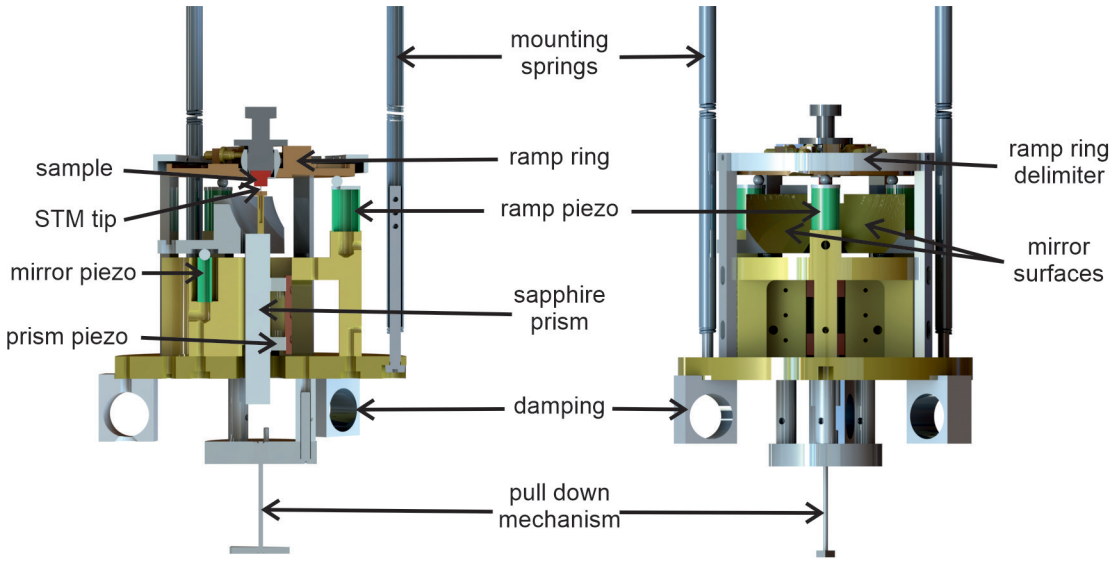

Figure 8.2: Rendered CAD drawing of the MIR-STM scan head. A cut-through (left) as well as the front view (right) of the MIR-STM scan head is shown. The individual, crucial parts are labeled and described further in the main text.

scan head is comprised of different types of piezo motors, which will be discussed individually. One major difference to the design of the THz-STM, where the tip is moved by a Besocke-type scanner [121], the roles are reversed here. Since the sample is attached to the ramp ring, which will be subsequently positioned by using dedicated ramp piezos, this already addresses one of the shortcomings of the previous design. The independent movement of the sample, without adjusting the position of the tip, allows for the laser to remain aligned with respect to the tip when changing the scanning position.

In this design, the tip can also be moved independently in the direction perpendicular to the sample surface. This is necessary in order move the tip into the focus of the laser beam. Here, the position of the laser focus in the direction perpendicular to the sample surface is determined by the focal length of te parabolic mirror attached to the scan head and can not be adjusted easily. This necessitates the mobility of the tip in this direction. This is achieved by mounting the tip to a sapphire prism, which can be moved using a set of shear piezos, similar to a so-called Pan design [213]. While this only allows proper focusing of the laser on the tip in one direction, the other directions can be addressed via the novel mirror design. The parabolic mirror is positioned on another set of three piezo tubes, which are embedded in the scan head and comprise another Besocke-type motor. This enables not only the movement of the mirror in the plane parallel to the sample surface, but also the rotation of the mirror and, combined with the positioning of the tip, permits the adjustment of the laser focus in all three dimensions.

Compared to the previous design, the parabolic mirror is positioned significantly closer to the tip sample junction, which is due to two reasons. Firstly, the close

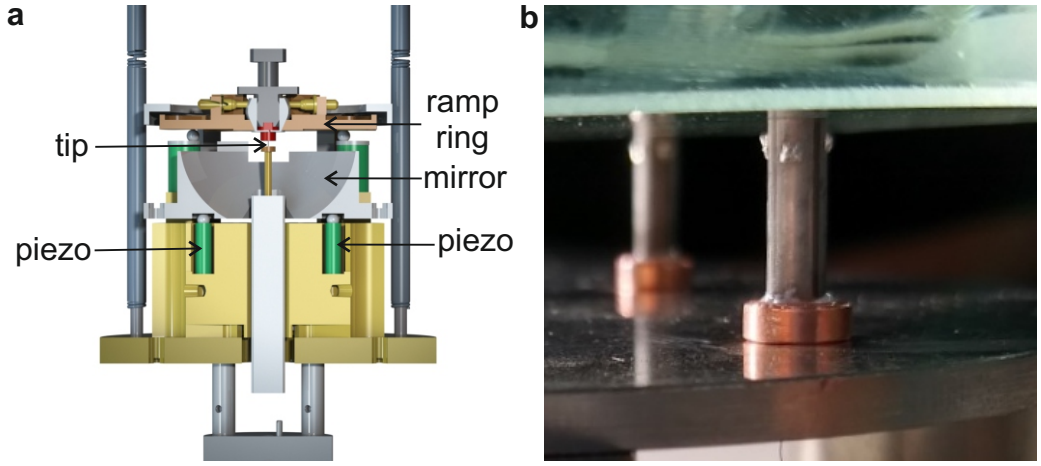

Figure 8.3: Construction of the mirror mover. **a**, Rendered image of a cut through the scan head. It shows the piezo tubes supporting the mirror, which are almost fully embedded in the solid body of the scanner. **b**, Gluing the piezo tubes to small copper disks allowed for easier assembly. A glass plate is positioned on top of the piezos to add weight in order to ensure proper adhesion to the glue. Image adapted from ref. [189].

proximity to the junction increases the numerical aperture and consequently reduces the size of the focus, resulting in a higher laser power density in the tip sample junction. Secondly, this parabolic mirror is also used to guide light out of the STM, which was not possible with the previous design. The half-circle layout of the custom-built mirror enables optical access to the tip via two beam paths, one for coupling the laser to the STM and one for guiding out any light scattered from or generated in the tip-sample junction.

In the following, the construction and assembly of the scan unit and several necessary adjustments to this initial design will be presented.

8.3.2 Assembly of the Mirror Mover

As a first step in the construction of the scan head, the mirror mover was assembled. It is comprised of a set of three thin piezo tubes, which are used similarly to a Besocke scanner. This motor can be used to move the mirror laterally and rotate it to the desired position in order to properly align the laser to the tip-sample junction.

One challenging aspect of this design is, that the piezo tubes are almost fully embedded into the solid copper body of the scanner, which is shown in figure 8.3a. This results in a very limited access to the piezo tubes, which complicates soldering any wires to the contacts of the piezos. Another, more severe problem arose from this as well. Since the piezo tubes used for the mirror mover are relatively small with an outer diameter of 3.2 mm and a length of 10 mm, it was impossible to position the tubes upright in the dedicated spaces. In order to prevent the tubes from toppling

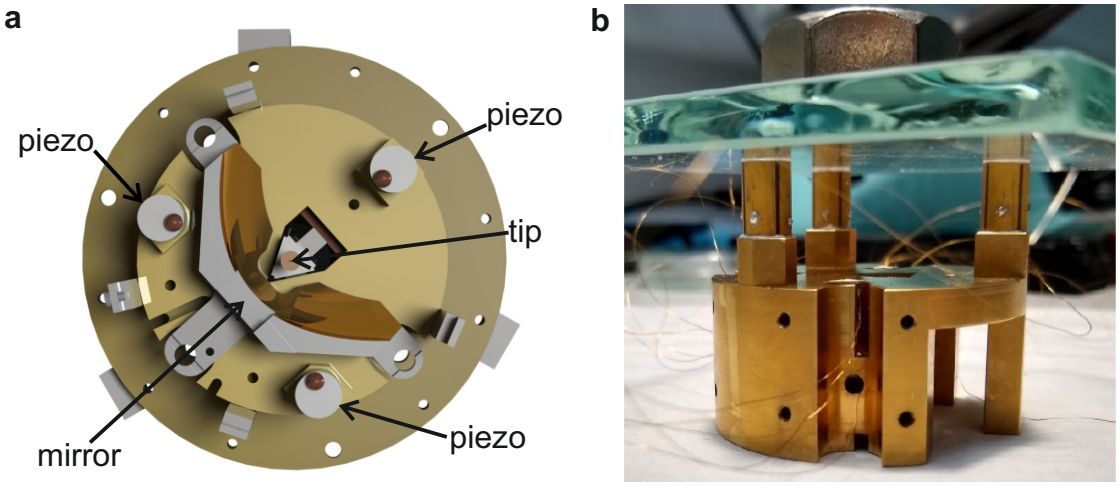

Figure 8.4: Construction of the sample Besocke scanner. a, Rendered image of a top view the scan head without ramp ring. The piezo tubes are mounted at the edge of the scan head, supporting the ramp ring carrying the sample. **b**, Gluing the piezo tubes to the scan head body. A glass plate is positioned on top of the piezos to add weight in order to ensure proper adhesion to the glue. Image adapted from [189]

over and to ensure a proper positioning, they were first glued to small copper disks with the diameter of the designated cutouts in the body (see figure 8.3). This way, it was possible to facilitate a proper centering of the tubes after positioning them in the scan head body.

The position of the piezo tubes is crucial for two reasons: Firstly, if one of the electrodes or a conductive part of the wire leading to the electrode touches the metal of the body, it will short the electrode. Secondly, the rotation of the piezos is also important for the proper operation of the mirror mover. Since the high voltage to move the piezo elements will be supplied in unison to specific electrodes of the tubes, a mismatch in the orientation of the piezo tubes will lead to the mirror moving in multiple directions simultaneously, which will prevent precise operation.

After positioning the piezo tubes was taken care of, they were glued into the scan head body. After that, sapphire spheres were attached to the top part of the piezo tubes. This way the mirror will only lie on three points at the piezo apexes, which ensures proper mechanical contact between piezos and the mirror.

8.3.3 Assembly of the Sample Besocke Scanner

After the mirror mover was assembled, the Besocke design to move the sample was implemented. To this end, the piezo tubes were first wired and then glued to the designated positions on the body of the scan head. As shown in figure 8.4a, these piezos are supposed to support the ramp ring, which will carry the sample.

This ramp ring is designed to have three symmetric slopes at the bottom side.

This allows the sample to be moved up and down and thus enables the approach of the sample towards the static tip. During operation of the apparatus, these piezos will also be used to move the sample while scanning the surface.

Compared to the mirror piezos, there are some differences in the setup of this Besocke design. On the one hand, the piezos used here have a larger diameter. Because of this, the spheres on top of the piezo are too small to be glued directly to the apex of the tube. To this end, an aluminum disk with a small hole is glued on top of the piezo to which the sphere is attached. Due to reasons explained later (see section 8.4.1), phosphor bronze spheres are used in this case instead of sapphire ones.

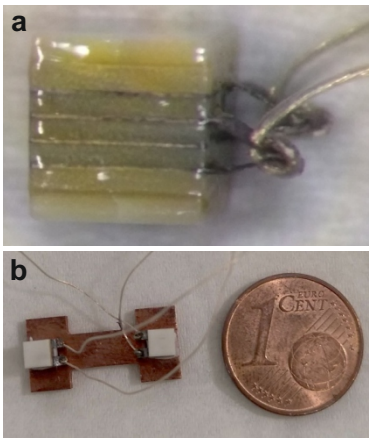

Figure 8.5: Stack piezos. **a**, Stack piezo with wire glued between the electrodes. **b**, Stack piezos attached to a copper plate. Images adapted from [189, 190].

8.3.4 Assembly of the Tip Motor

For the movement of the tip in the direction perpendicular to the sample surface we employed a motor in a design similar to the one proposed by Pan *et al.* [213], where the STM tip is attached to a prism which is moved by shear piezos. To this end, shear piezo stacks were wired by gluing a Kapton-insulated wire to each set of two electrodes on every piezo (see figure 8.5). To ensure proper conductance through the wires they were fixed to the electrodes with conductive silver epoxy glue.

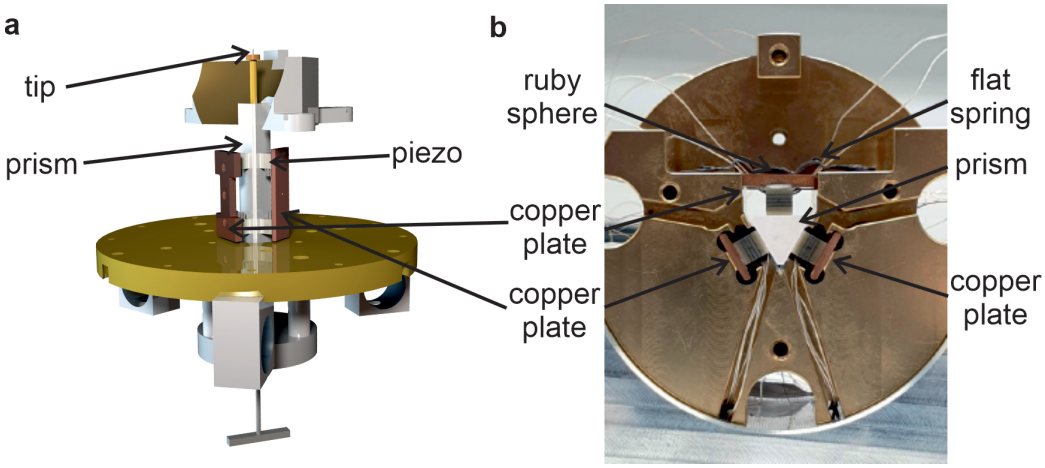

Figure 8.6: Construction of the tip motor. **a**, Rendered image of the scan head with the main body removed to show the location of the piezos moving the prism. **b**, Stack piezos and sapphire prism mounted in the scan head (bottom view). Image adapted from [190].

After wiring the piezos, they are fixated onto different copper slides in pairs as shown in figures 8.5b and 8.6a. Two of these pieces will later be slid directly into the scan head body (see figure 8.6b). After the final assembly of the head these will be inaccessible, which implies that careful and precise alignment of the piezos and the wires is invaluable. To this end, these copper plates were used to ensure proper positioning of the piezos before mounting them to their final positions in the scan head. The third and final piece is clamped to the body using a ruby sphere and a flat spring. Between these three sets of piezo pairs, a sapphire prism is inserted. This can be moved in two directions by the piezos, allowing the precise movement of the tip attached to the prism.

8.3.5 Assembly of the Scan Head

After all of the piezoelectric elements for the motors were implemented in the scan head, the remaining mechanical parts were attached to the setup and the scan head was finalized. This included the mounting of the base plate as well as constructing the damping mechanism.

Connecting the base plate of the scan head was performed after finishing all of the motors, since this part limits the access to several components, especially of the tip motor. It is rigidly fixated to the rest of the body using a set of screws in order to prevent vibrations and thus increase the stability of the system.

The damping mechanism also serves the same goal and is implemented via two components. The first one is the eddy current damping mechanism mounted to the STM base plate (see figure 8.7d). Here, a set of three strong permanent magnets is firmly attached to the scan head, which results in a synchronous movement of these magnets with any movement of the whole scan head. By mounting a counterpart made from conductive copper to the base of the shield of the helium cryostat, any movement of the head with respect to the shield will induce eddy currents, which will dampen vibrations of the scan head. The second important part of the damping mechanism are the mounting springs used to attach the scan head to the cryostat (see figure 8.7a and b). By using soft springs with a low resonance frequency, coupling of high frequency noise from the environment to the scan head can be prevented.

The last important mechanical part attached to the scan head is the pull-down mechanism. This will be used to pull the scan head down to the base of the helium shield and locking it in place. Fixating the scan head is crucial for sample transfer, because the mobile scan head would move too much when inserting a sample nto the scan head.

The fully assembled scan head is shown in figure 8.7, where it is already attached to the cryostat using mounting springs. After finishing the mechanical construction of the scan head body, several smaller parts were attached to allow proper STM operation. One of these parts is the ramp ring delimiter, which prevents excessive movement of the ramp ring in the lateral directions and thus falling off of the piezos.

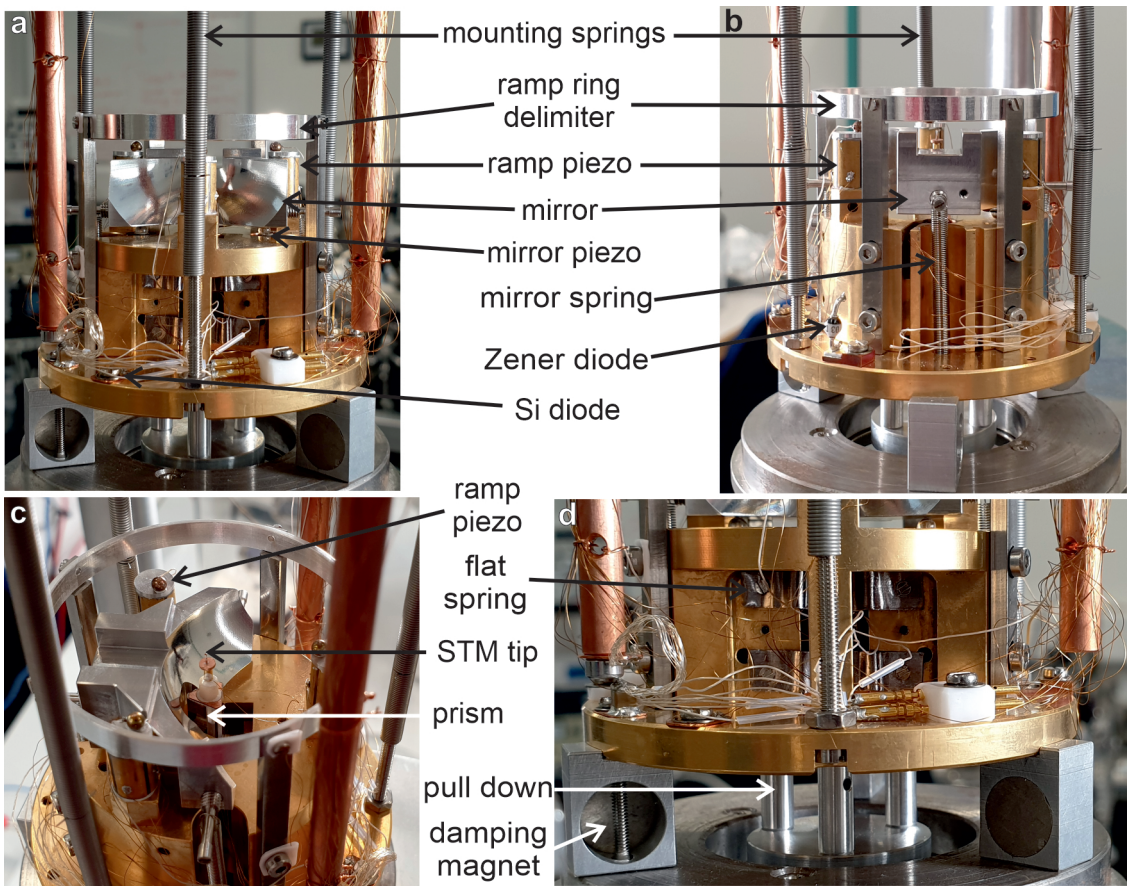

Figure 8.7: Assembly of the full MIR-STM scan head. Front view (**a**), back view (**b**) and top view **c** show the final assembly of the scan head with all party necessary for measurement. **d**, Detailed view of the lower part of the scan head, highlighting the pull down and damping mechanisms as well as the flat springs fixating the tip motor.

Furthermore, a Zener diode was implemented at the base plate of the scan head to facilitate variable temperature measurements as well as a silicon diode used to monitor the temperature (see figures 8.7a and b). The focusing mirror was also positioned on the dedicated piezo tubes and fixated to the base plate using a set of soft springs (see figure 8.7b). This ensures sufficient pressure of the mirror to the piezos, allowing proper operation of the motor. The STM tip was also implemented by gluing a small copper cannula to the top of the prism, in which a small platinum iridium wire is inserted (see figure 8.7c). This wire was cut beforehand to ensure a sharp tip apex used for later operation of the STM. The aforementioned pull down and damping mechanisms are shown in more detail in figure 8.7d. Strong neodymium magnets are positioned in aluminum holders, which will induce eddy currents in a copper counter part at the bottom of the cryo shields and dampen vibrations of the system. Here, also the two flat springs securing the tip motor are visible.

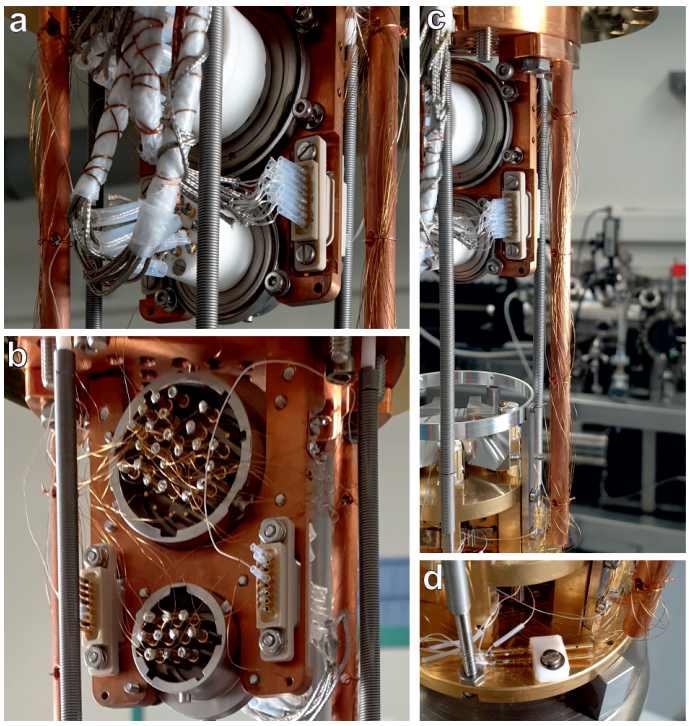

Figure 8.8: Wiring of the scan head. **a**, Back side of the transfer point with cables going through the cryostat. The twisted-pair stainless steel cables are organized using Macor plugs, D-sub connectors and Teflon foil. **b**, Front side of the transfer point with cables going to the scan head. Small pins are used to transfer each Kapton-insulated copper wire to a stainless steel cable. **c** Cooling finger used as a wire guide. **d**, Transfer point for the stack piezo wires, which reduces the number of wires going to the upper transfer point by 9.

Another challenge arising in the assembly of this design is the wiring of the scan head, which is shown in figure 8.8. Since this design features three independent piezo motors, the amount of wires needed to supply every electrode with the desired voltages is significantly higher compared to a simpler STM design. This problem is further exacerbated by two other points, namely the size of the sample holder and the laser beam path. Since a lot of space is needed to transfer a sample to the STM and to couple the laser to the junction, these areas have to be cleared of any wires, limiting the available space to guide the wires out of the cryostat. The overall wiring is realized the following way: From the top of the cryostat, twisted-pair stainless steel cables are threaded through the helium cryostat and connected to a transfer point mounted at the bottom of the helium cryostat (see figure 8.8a). This transfer point is comprised of four different plugs, where two large plugs are used to supply high voltage for the piezos and two small D-sub connectors transfer low voltage supplies and signals, for example the bias voltage or the tunneling current. Here, the stainless steel cables are connected by small pins to thin Kapton-insulated copper wires leading to the scan head. These wires are guided along a copper cooling finger (see figure 8.8c) in order to reduce heating of the scan head as well as to ensure sufficient space for sample transfer and laser coupling. Additionally, efforts to reduce the amount of wires going from the scan head to the transfer point were undertaken. Since only three different contacts are necessary for the operation of the tip motor, for example, another transfer point was implemented at the base plate of the scan head which reduces the amount of wires from 12 to 3 (see figure 8.8d).

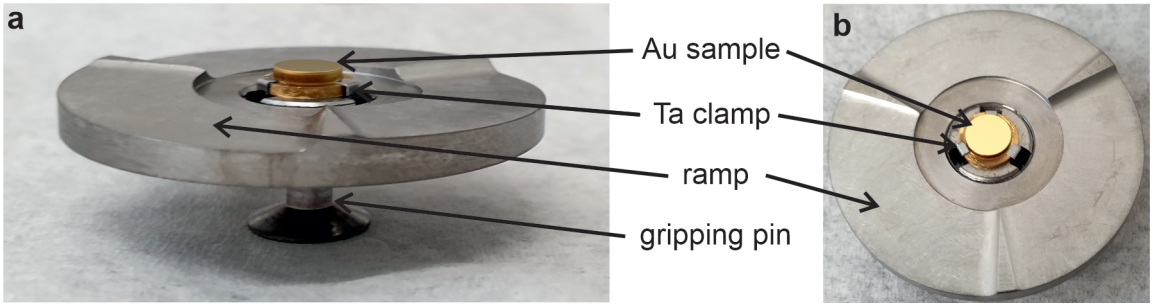

Figure 8.9: Sample holder with mounted gold sample. Side view (**a**) and top view (**b**) of a ramp ring with mounted Au(111) sample.

8.4 Sample Holder and Chamber Equipment

The work presented in this section was performed in collaboration with Victoria Ruckerbauer and Niklas Vogt, who contributed in this project in the scope of their respective Bachelor's Theses [191, 193].

Due to the novel design of the scan head, the sample holder had to be reconstructed as well. These changes not only affect the sample holder, but also the equipment used to prepare the samples, for example for annealing the sample to high temperatures. In this section, the novel sample holder design is first described. Afterwards, the necessary changes to other parts of the UHV equipment, specifically the construction of a preparation stage and changes to the manipulator, will be discussed.

8.4.1 Ramp Ring and Sample Holder Design

In contrast to previous designs, the sample is now attached to a ramp ring to avoid the aforementioned movement of the tip with respect to the laser beam. To realize this, a rigid design was employed in which the sample is embedded into a solid ramp ring made from molybdenum.

This, in turn, also has effects on the design of the scan head. For the operation of the STM it is necessary to apply a bias voltage between tip and sample, which requires electrical contacting of the sample in the scan head. To this end phosphor bronze spheres were positioned on top of the piezos of the sample Besocke scanner, which are connected with a wire and can be used to apply a bias voltage to the sample. Since the ramp ring sits on three of these spheres, there are multiple contact lines available for supplying the bias voltage. Furthermore, with a set of three contacts to the sample one could also envision using one of the contacts as a gate voltage in, for example, experiments on semiconductors. Due to the rigid design, any bias voltage applied to the ramp ring is simultaneously also applied to the sample.

The sample holder is shown in figure 8.9. A small pin is extending from the back of the ramp ring (see figure 8.9a), which is used to grab the sample holder with the manipulator and move it in the UHV chamber. With this design, it can be safely

and accurately moved to the scan head and placed on top of the piezos of the sample motor.

The sample is mechanically and electronically connected to the ramp ring using tantalum clamps to hold the sample in place (see figure 8.9b). During sample preparation, the metal crystal has to be annealed to high temperatures in order to achieve a clean and flat surface suitable for STM experiments. In previous setups, this was done using a small button heater while the sample was positioned at the manipulator, which allowed annealing the crystal specifically without heating the sample holder. On one hand, the thermal contact of the sample to the ramp ring in this design complicates this approach, since more power is required to heat the entire sample holder within a reasonable time frame. On the other hand, contacting the sample in a way that this could be done while the entire holder is grabbed by the manipulator is not feasible here. Due to these circumstances, the preparation process was overhauled and a new home-built preparation stage was developed.

8.4.2 Preparation Stage

In order to ensure clean and flat surfaces to perform high-precision experiments on, the metal sample described in the previous section has to be sputtered with noble gas ions and annealed to high temperatures. As mentioned before, annealing the sample while it is positioned at the manipulator is not feasible and a high-power heating process is needed for this novel design.

To this end, a preparation stage was developed allowing both sputtering and annealing to be performed. It includes an electron beam heater, which emits free

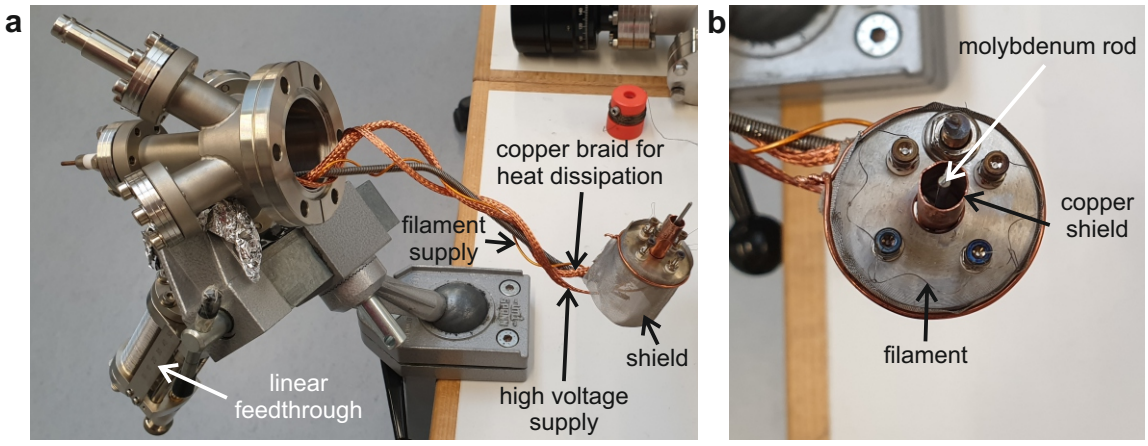

Figure 8.10: Preparation stage. **a**, Side view of the preparation stage mounted to the flange. The supply lines and the linear feedthrough for moving the stage are indicated in the image. **b**, Top view of the preparation stage. The sample holder will be placed onto the molybdenum rod and heated via accelerated electrons emitted from the filament.

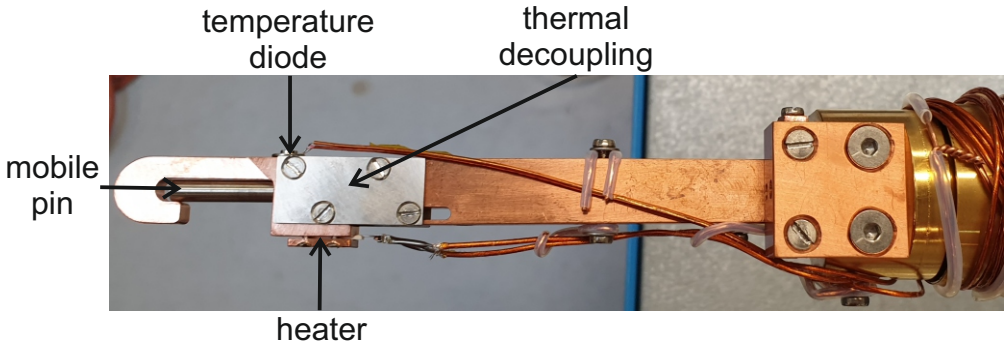

Figure 8.11: Redesigned front part of the manipulator. The manipulator head was adjusted to fit the new sample holder design. A mobile pin is used to clamp the sample holder. The location of a heating element, temperature diode and the thermal decoupling are also indicated.

electrons from a filament close to the sample, which are accelerated by a high voltage to the sample holder and heat the entire ramp ring as well as the sample. Images of the preparation stage are shown in figure 8.10. Figure 8.10a also depicts the flange at which the stage is mounted. Here, a linear feedthrough is implemented to allow movement of the whole stage within the UHV chamber. This is necessary to position the sample precisely in the beam of noble gas ions originating from the sputter gun located above the preparation stage. Furthermore, the individual supply lines are indicated, specifically the voltage supply for the filament as well as the high voltage used in the electron beam heater. The copper braid used for heat dissipation also serves as a connection to ground. Figure 8.10b shows a top view of the preparation stage. While preparing the sample, it is positioned on the molybdenum rod facing upwards. Afterwards, electrons are emitted from the filament and accelerated towards the sample holder and heating it, which allows annealing to temperatures of 1000 °C [191], which is measured by a pyrometer. For further information on the construction of the preparation stage and on test measurements, it is referred to ref. [191].

8.4.3 Manipulator Head

In order to move the sample to the preparation stage and into the STM, the front part of the manipulator had to be adjusted as well [193]. An image of this design is shown in figure 8.11, where the crucial parts are indicated. The sample can be picked up by the manipulator by inserting the gripping pin at the back of the sample holder (see figure 8.9) into the hook at the very front of the manipulator. There, the mobile pin indicated in figure 8.11 can be extended in order to fixate the sample holder in this position by pressing it into the notch.

Another important requirement, however, is the thermal coupling of the sample to the manipulator and the ability to heat the sample while it is grabbed. The reason for this is that, during operation of the apparatus at cryogenic temperatures,

the manipulator will be cooled to liquid nitrogen temperature when transferring a sample to the STM. This is done in order to minimize the thermal load coupled the helium cryostat during sample transfer and thus reduce the consumption of liquid helium. At the same time, the sample shall be kept at a higher temperature in order to avoid accumulation of impurities from residual gas particles in the vacuum chamber. To this end the front part of the manipulator was thermally decoupled from the back part, where the cryostat used for cooling to liquid nitrogen temperatures is located. Additionally, a temperature diode and a heating element were implemented in the front part. This allows the sample to be heated and the temperature to be monitored during sample transfer, while at the same time the back part of the manipulator can be cooled down to liquid nitrogen temperatures. Due to the thermal decoupling the heater is well-coupled to the sample holder and is not cooled by the cryostat, which enables cooling the manipulator while still maintaining reasonably high sample temperature during transfer. Shortly before the sample is inserted into the STM, the sample is cooled via the manipulator cryostat. This is done in order to reduce the thermal load coupled to the helium cryostat by the sample holder.

8.5 First Measurements with the MIR-STM

To test the functionality of the constructions described in this chapter, first test measurements were carried out. To this end, a Au(111) sample was prepared and analyzed while the apparatus was at room temperature. While this does not reflect a realistic measurement environment, it can still be assured that the piezoelectric motors as well as the STM electronics are working as intended.

8.5.1 Sample Preparation

The Au(111) sample was prepared via multiple cycles of sputtering and annealing. For sputtering, neon gas was dosed to a pressure of $5.1 \cdot 10^{-5}$ mbar into the preparation chamber. Operating the sputter gun at an emission current of 8 mA and a beam energy of 1 kV resulted in a sputtering current of 9 μA measured at the sample. The sample was sputtered for $\approx$ 25 minutes for each cycle.

In between sputtering cycles, the sample was annealed to $\approx 550\,^{\circ}\mathrm{C}$ using the electron beam heater. The temperature of the sample was monitored using a pyrometer, where the final temperature was determined after switching off the electron filament since this was influencing the temperature readout.

After the third sputtering cycle, the sample was annealed to $\approx 500\,^{\circ}\mathrm{C}$ and transferred to the STM after cooling down to room temperature.

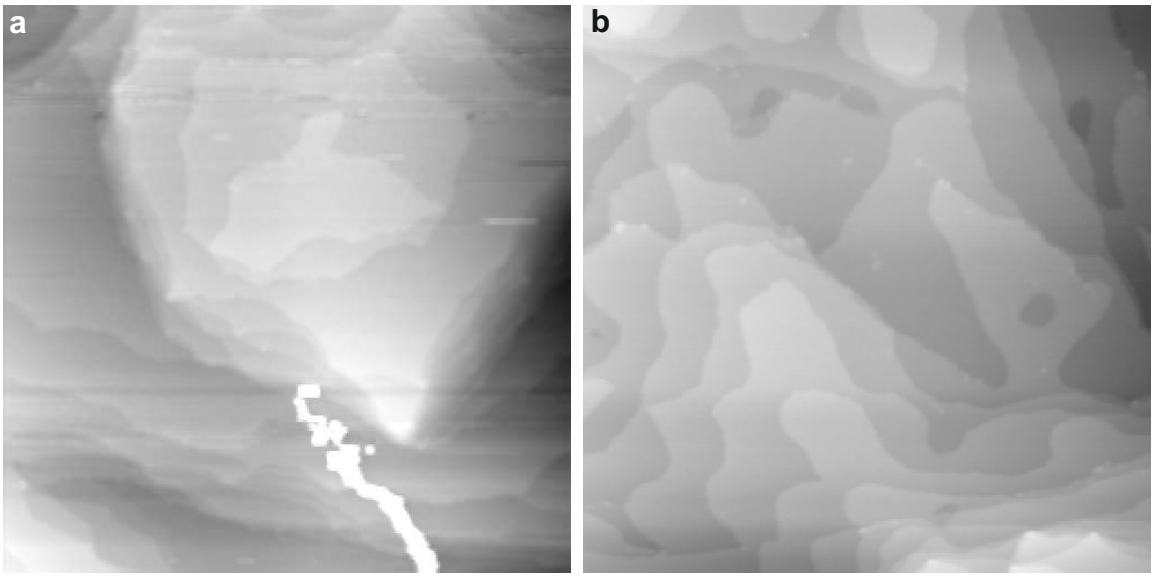

Figure 8.12: First images of a Au(111) surface obtained with the MIR-STM. a, Constant current image of an Au(111) surface obtained with the MIR-STM. Some instabilities of the tip are visible in the image. **b**, Constant current overview of the Au(111) surface after stabilizing the tip showing a clean area and monoatomic steps. Experimental parameters: **a**: Setpoint: 395 mV, 78 pA; **b**: Setpoint: 395 mV, 79 pA.

8.5.2 Au(111) Surface Imaged with the MIR-STM

After the sample was transferred to the STM, the tip was manually positioned using the tip motor. Afterwards, the sample was approached to the tip using the automatic approach scheme supplied by the STM electronics. Before any contrast could be observed, the tip had to be cleaned via controlled indentation into the metal sample.

First images obtained with the MIR-STM are shown in figure 8.12, which depict a Au(111) surface. While the first image shown in figure 8.12a still exhibits slight instabilities of the tip, which appear as small stripes in the image, monoatomic steps between different terraces of the sample could already be observed. At the bottom of the image, a bright feature occurs, which is likely due to either tip instability or contamination with foreign atoms. After further tip preparation via controlled indentation into the metal, the image shown in figure 8.12b was obtained. Here, the noise due to tip instabilities as observed in figure 8.12a is absent, and clean metal terraces could be imaged.

In the images shown in figure 8.12 scale bars and image sizes are deliberately omitted, since, at the time of acquiring these images, the piezos were not yet calibrated. This implies that the voltage applied to the piezo tubes can not yet be related to distances and thus yield no information about the exact size of the scanned area. Even without knowledge of the piezo constants, however, the observation of a clean

metal area with monoatomic steps already shows that the mechanical construction as well as the measurement electronics of the MIR-STM scan head work as intended.

This observation not only proves, that the scan head itself is operational, but also that the preparation equipment described above can also be used to prepare clean and flat metal surfaces. While this process can still be optimized, for example regarding the sputtering position and current or the annealing temperature or duration, a sample preparation suitable for single molecule experiments was already achieved.

8.6 Summary & Outlook

In this chapter we have outlined the progress made towards the construction of a next-generation lightwave-driven scanning tunneling microscope. To this end we fully redesigned the entire STM scan unit in order to ensure the usability with shorter laser pulses with a higher center frequency. The construction of the individual motors built into the system as well as further equipment used for sample handling and preparation was described. In particular, the following was shown:

- In the beginning we have described the design of the THz-STM, in particular the laser coupling to the STM junction and its shortcomings. Here, two possibilities for improvement were identified: On the one hand, the tip movement relative to the laser focus when moving to different areas on the sample requires frequent realignment of the laser. On the other hand, the light scattered from the junction is not recollected and might yield valuable information about processes occurring in the STM junction.
- Following this evaluation, we presented a novel scan head design addressing all of the shortcomings of the first THz-STM. A design with three independent piezo motors allows for a precise control of tip, sample and focusing mirror position. Furthermore, the parabolic mirror used for focusing the laser to the tip is located close to the tip-sample junction, which increases the numerical aperture and allows for smaller focus diameter. The design of this parabolic mirror also enables the collection of scattered light, which can be analyzed for a wide range of experiments.
- The construction of the individual motors as well as the assembly of the full scan head was elaborated. The implementation of two Besocke-type scanners for the sample and mirror movement as well as a Pan-type scanner for positioning the tip were outlined. Further, we described the mechanical construction of the individual parts and display the challenges in wiring the new scan unit.
- Due to the novel scan head design, the sample holder as well as the chamber equipment used to move and prepare the sample in the UHV environment had to be modified as well. Since the sample is attached to a molybdenum ramp ring, a preparation stage was constructed, which is equipped with electron beam heating to ensure proper annealing of the sample. The manipulator head was redesigned to enable transferring this new sample holder inside the

UHV chambers.

- We performed a test measurement by preparing a Au(111) sample and image its surface at room temperature. In this preliminary experiment it was demonstrated, that all elements of this novel apparatus are functional and STM measurements can be performed.

Overall we have depicted the construction of a home-built STM apparatus based on a novel design from its inception to utilizing the apparatus to image a Au(111) surface at room temperature. In the near future, we will combine this STM with the dedicated optics setup to couple ultrashort MIR pulses to the junction and perform lightwave-driven STM experiments pushing towards sub-femtosecond temporal resolution in order to explore new grounds in the field of atomic scale dynamics.

9 Summary

In the scope of this thesis various methods to study light-matter interaction at the atomic scale were explored. We gained insights into the exertion of ultrafast forces acting on single molecules, the triggering of molecular motion via photoexcitation and the generation of single electron photocurrents. Furthermore, the construction of an apparatus for time-resolved measurements down to the sub-femtosecond scale with combined atomic spatial resolution was presented.

In chapter 5 the ultrafast forces acting on a single magnesium phthalocyanine (MgPc) molecule adsorbed on an ultrathin layer of NaCl on Cu(111) were discussed. Here, MgPc can adsorb in a bistable geometry, where switching between these two configurations can be triggered via charging the molecule. We facilitated this by employing ultrafast THz pulses to inject electrons into the LUMO of the molecule an thus trigger a switching event. Mapping the switching probability across the molecule reveals that it is directly connected to the charging probability via LUMO tunneling. Pump probe experiments indicate that this switching probability can be influenced by a force transient in the form of the electric field of a THz pulse tuned below the resonance of the molecule. DFT calculations show that this out-of-plane electric field causes an in-plane frustrated rotation of the molecular frame, which modulates the switching probability with a frequency of 0.3 THz. Space- and time-resolved maps of this effect unveil, that this motion can only be excited by exerting forces on select atoms of the molecule due to the interaction of these atoms with the underlying NaCl substrate.

In chapter 6 we investigated the photoinduced toggling motion of a single molecule. To this end, a novel combination of an optical nanosecond pulsed laser with a combined STM/AFM apparatus was established. Via various test measurements we have ensured the stability of the STM/AFM under laser illumination. The key advantage of this technique is the ability to synchronize the laser pulses with the oscillation of the AFM cantilever. By changing the phase between laser pulses and cantilever oscillation, the exact tip-sample distance at which the laser pulses are coupled to the junction can be adjusted, what allows experiments over a large span of tip-molecule distances. Utilizing this approach, a single MgPc molecule adsorbed on ultrathin NaCl on Cu(111) was studied, where we have shown that the switching between its two stable neutral adsorption geometries can be triggered by photoexcitation of the molecule. By exciting the molecule for various tip-sample distances we were able to show that this toggling motion is mediated by a relaxation of the photoexcited state through charge exchange with the SPM electrodes. This interpretation is further underlined by a map of the switching rate of the molecule, which follows the contrast

of the LUMO of MgPc and thus indicates a relaxation via a transiently charged state caused by charge exchange with the tip.

In chapter 7 we explored the effects of photoexcitation on single copper phthalocyanine (CuPc) molecules deposited onto bulk-like NaCl grown on Cu(111). As a first step the effects of charging the molecule via electrons tunneling from the tip were explored and the electronic states were mapped using AC-STM. By employing laser pulses synchronized with the AFM cantilever oscillation we were able to generate single electron photocurrents from individual CuPc molecules. Since the molecule is decoupled from the conductive substrate by the thick insulating layer, exchanging single electrons between tip and molecule leaves it in a stable, well defined charge state. Changes in the charge state of the molecule could be induced with the laser, which were observed in the frequency shift as well as the damping of the cantilever. Employing simulations we found that this behavior stems from single electron photocurrents resulting from the direct excitation of the molecule followed by a neutralization via charge exchange through a different orbital. Spatially resolving these single electron photocurrents revealed that the contrast shown in these maps follows the outline of the molecular orbitals. Since in these experiments charging and discharging are facilitated via electron exchange of the tip with different orbitals, this results in a superposition of these orbitals being observed in the photocurrent maps. The contrast obtained in these maps as well as polarization dependent measurements underline direct photoexcitation of the molecule as the origin of the recorded signals. In order to reduce the aforementioned influence of the orbital facilitating the discharging of the molecule, we employed voltage pulses to enhance the tunneling rate at the turning points of the cantilever oscillation. While this appeared to have the intended effect, no contrast within the molecular orbitals could be observed, which is attributed to the saturation of the generated photocurrent. The investigation of a molecule adsorbed close to a NaCl step edge, which exhibited a lifted degeneracy of the LUMOs, revealed, that the discharging process still had a major influence on the contrast observed in the photocurrent maps. As a final step, the possibility of this technique to study molecular dimers was demonstrated. Mapping photocurrents across a CuPc/pentacene dimer revealed, that only CuPc can be excited by the laser wavelength used in this experiment and that no lateral transfer of photoexcited charges is taking place in this particular system.

In chapter 8 we outlined the development of a next-generation lightwave-driven scanning tunneling microscope. As a first step, we have discussed the necessary improvements for the operation of a lightwave-driven STM with mid-infrared laser pulses. A novel design of the STM scan unit was presented, which featured significant improvements over previous apparatuses. Specifically, in this design the STM tip is kept at a fixed position during operation, which avoids repeat realignment of the laser. This is achieved by using a Besocke motor to move the sample relative to the tip and employing a Pan motor to move the tip into the focus of the laser. Furthermore, a parabolic mirror in a half-circle design is positioned close to the sample, which not only allows collection of light scattered from the junction but also enables a small

focus size of the laser due to the large numerical aperture. This mirror is situated on another Besocke motor to enable precise alignment of the laser to the tip. The construction of the scan head in this novel design was elaborated as well as changes made to other UHV equipment necessary for the operation of the MIR-STM. These include the sample holder, which is now including the ramp ring used for movement of the sample, the preparation stage, which was developed to facilitate sputtering and annealing the sample to sufficiently high temperatures, and the manipulator head, which is used to move the sample in UHV. In order to test the functionality of this setup we prepared a Au(111) sample and transferred it to the STM, where we were able to resolve monoatomic step edges at room temperature. This proves that all the individual parts developed for the MIR-STM are working as intended and that STM measurements can be performed with this novel STM apparatus.

Bibliography

1. Blankenship, R. E. *Molecular mechanisms of photosynthesis* (John Wiley & Sons, 2021).
2. Turro, N. J., Ramamurthy, V., Scaiano, J. C., *et al. Modern molecular photochemistry of organic molecules* (University Science Books Sausalito, CA, 2010).
3. Hedley, G. J., Ruseckas, A. & Samuel, I. D. Light harvesting for organic photovoltaics. *Chemical Reviews* **117,** 796–837 (2017).
4. Goulielmakis, E. *et al.* Attosecond control and measurement: lightwave electronics. *Science* **317,** 769–775 (2007).
5. Forn-Díaz, P., Lamata, L., Rico, E., Kono, J. & Solano, E. Ultrastrong coupling regimes of light-matter interaction. *Reviews of Modern Physics* **91,** 025005 (2019).
6. Binnig, G., Rohrer, H., Gerber, C. & Weibel, E. Tunneling through a controllable vacuum gap. *Applied Physics Letters* **40,** 178–180 (1982).
7. Binnig, G., Quate, C. F. & Gerber, C. Atomic force microscope. *Physical Review Letters* **56,** 930 (1986).
8. Giessibl, F. J. Atomic resolution of the silicon (111)-(7×7) surface by atomic force microscopy. *Science* **267,** 68–71 (1995).
9. Gross, L., Mohn, F., Moll, N., Liljeroth, P. & Meyer, G. The chemical structure of a molecule resolved by atomic force microscopy. *Science* **325,** 1110–1114 (2009).
10. Binnig, G., Rohrer, H., Gerber, C. & Weibel, E. Surface studies by scanning tunneling microscopy. *Physical Review Letters* **49,** 57 (1982).
11. Eigler, D. M. & Schweizer, E. K. Positioning single atoms with a scanning tunnelling microscope. *Nature* **344,** 524 (1990).
12. Repp, J., Meyer, G., Stojković, S. M., Gourdon, A. & Joachim, C. Molecules on insulating films: scanning-tunneling microscopy imaging of individual molecular orbitals. *Physical Review Letters* **94,** 026803 (2005).
13. Perera, U. G. E. *et al.* Controlled clockwise and anticlockwise rotational switching of a molecular motor. *Nature Nanotechnology* **8,** 46–51 (2013).
14. Völcker, M., Krieger, W. & Walther, H. *A Laser-Driven Scanning Tunneling Microscope* in *AIP Conference Proceedings* **241** (1991), 51–60.

15. Stöckle, R. M., Suh, Y. D., Deckert, V. & Zenobi, R. Nanoscale chemical analysis by tip-enhanced Raman spectroscopy. *Chemical Physics Letters* **318,** 131–136 (2000).

16. Cocker, T. L. *et al.* An ultrafast terahertz scanning tunnelling microscope. *Nature Photonics* **7,** 620 (2013).

17. Betzig, E. & Chichester, R. J. Single molecules observed by near-field scanning optical microscopy. *Science* **262,** 1422–1425 (1993).

18. Zimmermann, F. M. & Ho, W. State resolved studies of photochemical dynamics at surfaces. *Surface Science Reports* **22,** 127–247 (1995).

19. Lee, J., Crampton, K. T., Tallarida, N. & Apkarian, V. Visualizing vibrational normal modes of a single molecule with atomically confined light. *Nature* **568,** 78–82 (2019).

20. Cocker, T. L., Peller, D., Yu, P., Repp, J. & Huber, R. Tracking the ultrafast motion of a single molecule by femtosecond orbital imaging. *Nature* **539,** 263–267 (2016).

21. Li, S. *et al.* Bond-Selected Photodissociation of Single Molecules Adsorbed on Metal Surfaces. *Physical Review Letters* **122,** 1–6 (2019).

22. Chen, C. J. *Introduction to Scanning Tunneling Microscopy* (Oxford University Press on Demand, 1993).

23. Schwabl, F. *Quantum mechanics* (Springer Science & Business Media, 2007).

24. Bardeen, J. Tunnelling from a many-particle point of view. *Physical Review Letters* **6,** 57 (1961).

25. Tersoff, J. & Hamann, D. Theory and application for the scanning tunneling microscope. *Physical Review Letters* **50,** 1998 (1983).

26. Tersoff, J. & Hamann, D. in *Scanning Tunneling Microscopy* 59–67 (Springer, 1985).

27. Fließbach, T. *Quantenmechanik: Lehrbuch zur Theoretischen Physik III* (Springer-Verlag, 2018).

28. Repp, J., Meyer, G., Paavilainen, S., Olsson, F. E. & Persson, M. Scanning tunneling spectroscopy of Cl vacancies in NaCl films: strong electron-phonon coupling in double-barrier tunneling junctions. *Physical Review Letters* **95,** 225503 (2005).

29. Gimzewski, J., Reihl, B., Coombs, J. & Schlittler, R. Photon emission with the scanning tunneling microscope. *Zeitschrift für Physik B Condensed Matter* **72,** 497–501 (1988).

30. Gimzewski, J., Sass, J., Schlitter, R. & Schott, J. Enhanced photon emission in scanning tunnelling microscopy. *EPL (Europhysics Letters)* **8,** 435 (1989).

31. Hoffmann, G., Libioulle, L. & Berndt, R. Tunneling-induced luminescence from adsorbed organic molecules with submolecular lateral resolution. *Physical Review B* **65,** 212107 (2002).

32. Qiu, X., Nazin, G. & Ho, W. Vibrationally resolved fluorescence excited with submolecular precision. *Science* **299,** 542–546 (2003).

33. Kuhnke, K., Grosse, C., Merino, P. & Kern, K. Atomic-scale imaging and spectroscopy of electroluminescence at molecular interfaces. *Chemical Reviews* **117,** 5174–5222 (2017).

34. Rosławska, A. *et al.* Single charge and exciton dynamics probed by molecular-scale-induced electroluminescence. *Nano Letters* **18,** 4001–4007 (2018).

35. Merino, P., Große, C., Rosławska, A., Kuhnke, K. & Kern, K. Exciton dynamics of C_{60}-based single-photon emitters explored by Hanbury Brown–Twiss scanning tunnelling microscopy. *Nature Communications* **6,** 1–6 (2015).

36. Große, C. *et al.* Submolecular electroluminescence mapping of organic semiconductors. *ACS Nano* **11,** 1230–1237 (2017).

37. Schuler, B. *et al.* Electrically driven photon emission from individual atomic defects in monolayer WS2. *Science Advances* **6,** eabb5988 (2020).

38. Imada, H. *et al.* Real-space investigation of energy transfer in heterogeneous molecular dimers. *Nature* **538,** 364–367 (2016).

39. Doppagne, B. *et al.* Electrofluorochromism at the single-molecule level. *Science* **361,** 251–255 (2018).

40. Kröger, J., Doppagne, B., Scheurer, F. & Schull, G. Fano description of single-hydrocarbon fluorescence excited by a scanning tunneling microscope. *Nano Letters* **18,** 3407–3413 (2018).

41. Yang, B. *et al.* Sub-nanometre resolution in single-molecule photoluminescence imaging. *Nature Photonics* **14,** 693–699 (2020).

42. Hung, T.-C., Kiraly, B., Strik, J. H., Khajetoorians, A. A. & Wegner, D. Plasmon-driven motion of an individual molecule. *Nano Letters* **21,** 5006–5012 (2021).

43. Zhang, Y. *et al.* Sub-nanometre control of the coherent interaction between a single molecule and a plasmonic nanocavity. *Nature Communications* **8,** 1–7 (2017).

44. Ćavar, E. *et al.* Fluorescence and phosphorescence from individual C_{60} molecules excited by local electron tunneling. *Physical Review Letters* **95,** 196102 (2005).

45. Miwa, K. *et al.* Many-body state description of single-molecule electroluminescence driven by a scanning tunneling microscope. *Nano Letters* **19,** 2803–2811 (2019).

46. Doležal, J., Canola, S., Merino, P. & Švec, M. Exciton-trion conversion dynamics in a single molecule. *ACS Nano* **15,** 7694–7699 (2021).

47. Vasilev, K. *et al.* Internal Stark effect of single-molecule fluorescence. *Nature Communications* **13,** 1–8 (2022).

48. Rosławska, A. *et al.* Mapping Lamb, Stark, and Purcell effects at a chromophore-picocavity junction with hyper-resolved fluorescence microscopy. *Physical Review X* **12,** 011012 (2022).

49. Cao, S. *et al.* Energy funnelling within multichromophore architectures monitored with subnanometre resolution. *Nature Chemistry* **13,** 766–770 (2021).

50. Doppagne, B. *et al.* Single-molecule tautomerization tracking through space- and time-resolved fluorescence spectroscopy. *Nature Nanotechnology* **15,** 207–211 (2020).

51. Doležal, J. *et al.* Mechano-optical switching of a single molecule with doublet emission. *ACS Nano* **14,** 8931–8938 (2020).

52. Kimura, K. *et al.* Selective triplet exciton formation in a single molecule. *Nature* **570,** 210–213 (2019).

53. Zhang, Y. *et al.* Visualizing coherent intermolecular dipole–dipole coupling in real space. *Nature* **531,** 623–627 (2016).

54. Doležal, J. *et al.* Charge carrier injection electroluminescence with CO-functionalized tips on single molecular emitters. *Nano Letters* **19,** 8605–8611 (2019).

55. Rossel, F., Pivetta, M. & Schneider, W.-D. Luminescence experiments on supported molecules with the scanning tunneling microscope. *Surface Science Reports* **65,** 129–144 (2010).

56. Imada, H. *et al.* Single-molecule investigation of energy dynamics in a coupled plasmon-exciton system. *Physical Review Letters* **119,** 013901 (2017).

57. Nunes Jr, G. & Freeman, M. Picosecond resolution in scanning tunneling microscopy. *Science* **262,** 1029–1032 (1993).

58. Weiss, S., Ogletree, D., Botkin, D., Salmeron, M. & Chemla, D. Ultrafast scanning probe microscopy. *Applied Physics Letters* **63,** 2567–2569 (1993).

59. Feldstein, M., Vöhringer, P., Wang, W. & Scherer, N. Femtosecond optical spectroscopy and scanning probe microscopy. *The Journal of Physical Chemistry* **100,** 4739–4748 (1996).

60. Garg, M. & Kern, K. Attosecond coherent manipulation of electrons in tunneling microscopy. *Science* **367,** 411–415 (2020).

61. Gutzler, R., Garg, M., Ast, C. R., Kuhnke, K. & Kern, K. Light–matter interaction at atomic scales. *Nature Reviews Physics* **3,** 441–453 (2021).

62. Grafström, S. Photoassisted scanning tunneling microscopy. *Journal of Applied Physics* **91,** 1717–1753 (2002).

63. Kloth, P., Thias, T., Bunjes, O., Von Der Haar, J. & Wenderoth, M. A versatile implementation of pulsed optical excitation in scanning tunneling microscopy. *Review of Scientific Instruments* **87,** 123702 (2016).

64. Yoshioka, K. *et al.* Real-space coherent manipulation of electrons in a single tunnel junction by single-cycle terahertz electric fields. *Nature Photonics* **10,** 762–765 (2016).

65. Pettinger, B., Schambach, P., Villagómez, C. J. & Scott, N. Tip-enhanced Raman spectroscopy: near-fields acting on a few molecules. *Annual Review of Physical Chemistry* **63,** 379–399 (2012).

66. Pettinger, B., Domke, K. F., Zhang, D., Picardi, G. & Schuster, R. Tip-enhanced Raman scattering: influence of the tip-surface geometry on optical resonance and enhancement. *Surface Science* **603,** 1335–1341 (2009).

67. Böckmann, H. *et al.* Near-Field Manipulation in a Scanning Tunneling Microscope Junction with Plasmonic Fabry-Pérot Tips. *Nano Letters* **19,** 3597–3602 (2019).

68. Pozzi, E. A. *et al.* Ultrahigh-vacuum tip-enhanced Raman spectroscopy. *Chemical Reviews* **117,** 4961–4982 (2017).

69. Zrimsek, A. B. *et al.* Single-molecule chemistry with surface-and tip-enhanced Raman spectroscopy. *Chemical Reviews* **117,** 7583–7613 (2017).

70. Zhang, R. *et al.* Chemical mapping of a single molecule by plasmon-enhanced Raman scattering. *Nature* **498,** 82–86 (2013).

71. Yampolsky, S. *et al.* Seeing a single molecule vibrate through time-resolved coherent anti-Stokes Raman scattering. *Nature Photonics* **8,** 650–656 (2014).

72. Jaculbia, R. B. *et al.* Single-molecule resonance Raman effect in a plasmonic nanocavity. *Nature Nanotechnology* **15,** 105–110 (2020).

73. Li, S., Chen, S., Li, J., Wu, R., Ho, W., *et al.* Joint space-time coherent vibration driven conformational transitions in a single molecule. *Physical Review Letters* **119,** 176002 (2017).

74. Liu, S., Wolf, M. & Kumagai, T. Plasmon-assisted resonant electron tunneling in a scanning tunneling microscope junction. *Physical Review Letters* **121,** 226802 (2018).

75. Imada, H. *et al.* Single-molecule laser nanospectroscopy with micro–electron volt energy resolution. *Science* **373,** 95–98 (2021).

76. Imai-Imada, M. *et al.* Orbital-resolved visualization of single-molecule photocurrent channels. *Nature* **603,** 829–834 (2022).

77. Cocker, T., Jelic, V., Hillenbrand, R. & Hegmann, F. Nanoscale terahertz scanning probe microscopy. *Nature Photonics* **15,** 558–569 (2021).

78. Garg, M. *et al.* Real-space subfemtosecond imaging of quantum electronic coherences in molecules. *Nature Photonics* **16,** 196–202 (2022).

79. Sheng, S. *et al.* Launching coherent acoustic phonon wave packets with local femtosecond coulomb forces. *Physical Review Letters* **129,** 043001 (2022).

80. Peller, D. *et al.* Sub-cycle atomic-scale forces coherently control a single-molecule switch. *Nature* **585,** 58–62 (2020).

81. Peller, D. *et al.* Quantitative sampling of atomic-scale electromagnetic waveforms. *Nature Photonics* **15,** 143–147 (2021).

82. Jelic, V. *et al.* Ultrafast terahertz control of extreme tunnel currents through single atoms on a silicon surface. *Nature Physics* **13,** 591–598 (2017).

83. Ammerman, S. *et al.* Lightwave-driven scanning tunnelling spectroscopy of atomically precise graphene nanoribbons. *Nature Communications* **12,** 1–9 (2021).

84. Yoshida, S. *et al.* Subcycle transient scanning tunneling spectroscopy with visualization of enhanced terahertz near field. *ACS Photonics* **6,** 1356–1364 (2019).

85. Müller, M., Martin Sabanés, N., Kampfrath, T. & Wolf, M. Phase-resolved detection of ultrabroadband THz pulses inside a scanning tunneling microscope junction. *ACS Photonics* **7,** 2046–2055 (2020).

86. Giessibl, F. J. & Binnig, G. Investigation of the (001) cleavage plane of potassium bromide with an atomic force microscope at 4.2 K in ultra-high vacuum. *Ultramicroscopy* **42,** 281–289 (1992).

87. Giessibl, F. J. The qPlus sensor, a powerful core for the atomic force microscope. *Review of Scientific Instruments* **90,** 011101 (2019).

88. Albrecht, T. R., Grütter, P., Horne, D. & Rugar, D. Frequency modulation detection using high-Q cantilevers for enhanced force microscope sensitivity. *Journal of Applied Physics* **69,** 668–673 (1991).

89. Giessibl, F. J. Advances in atomic force microscopy. *Rev. Mod. Phys.* **75,** 949–983 (3 2003).

90. Nonnenmacher, M., o'Boyle, M. & Wickramasinghe, H. K. Kelvin probe force microscopy. *Applied Physics Letters* **58,** 2921–2923 (1991).

91. Melitz, W., Shen, J., Kummel, A. C. & Lee, S. Kelvin probe force microscopy and its application. *Surface Science Reports* **66,** 1–27 (2011).

92. Sadewasser, S. & Glatzel, T. *Kelvin probe force microscopy* (Springer, 2012).

93. Fatayer, S. *et al.* Molecular structure elucidation with charge-state control. *Science* **365,** 142–145 (2019).

94. Steurer, W., Fatayer, S., Gross, L. & Meyer, G. Probe-based measurement of lateral single-electron transfer between individual molecules. *Nature Communications* **6,** 1–5 (2015).

95. Gross, L. *et al.* Measuring the charge state of an adatom with noncontact atomic force microscopy. *Science* **324,** 1428–1431 (2009).

96. Albrecht, F. *et al.* Probing charges on the atomic scale by means of atomic force microscopy. *Physical Review Letters* **115,** 076101 (2015).

97. Mohn, F., Gross, L., Moll, N. & Meyer, G. Imaging the charge distribution within a single molecule. *Nature Nanotechnology* **7,** 227–231 (2012).

98. Morita, S., Giessibl, F. J., Meyer, E. & Wiesendanger, R. *Noncontact Atomic Force Microscopy: Volume 3* (Springer, 2015).

99. Patera, L. L., Queck, F., Scheuerer, P. & Repp, J. Mapping orbital changes upon electron transfer with tunnelling microscopy on insulators. *Nature* **566,** 245–248 (2019).

100. Lotze, C., Corso, M., Franke, K. J., von Oppen, F. & Pascual, J. I. Driving a macroscopic oscillator with the stochastic motion of a hydrogen molecule. *Science* **338,** 779–782 (2012).

101. Cockins, L., Miyahara, Y., Bennett, S. D., Clerk, A. A. & Grutter, P. Excited-state spectroscopy on an individual quantum dot using atomic force microscopy. *Nano Letters* **12,** 709–713 (2012).

102. Scheuerer, P., Patera, L. L. & Repp, J. Manipulating and Probing the Distribution of Excess Electrons in an Electrically Isolated Self-Assembled Molecular Structure. *Nano Letters* **20,** 1839–1845 (2020).

103. Patera, L. L., Queck, F., Scheuerer, P., Moll, N. & Repp, J. Accessing a charged intermediate state involved in the excitation of single molecules. *Physical Review Letters* **123,** 016001 (2019).

104. Patera, L. L., Queck, F. & Repp, J. Imaging charge localization in a conjugated oligophenylene. *Physical Review Letters* **125,** 176803 (2020).

105. Steurer, W., Repp, J., Gross, L. & Meyer, G. Damping by sequentially tunneling electrons. *Surface Science* **678,** 112–117 (2018).

106. Repp, J., Meyer, G., Olsson, F. E. & Persson, M. Controlling the charge state of individual gold adatoms. *Science* **305,** 493–495 (2004).

107. Swart, I., Sonnleitner, T. & Repp, J. Charge state control of molecules reveals modification of the tunneling barrier with intramolecular contrast. *Nano Letters* **11,** 1580–1584 (2011).

108. Leoni, T. *et al.* Controlling the charge state of a single redox molecular switch. *Physical Review Letters* **106,** 216103 (2011).

109. Scheuerer, P. *et al.* Charge-induced structural changes in a single molecule investigated by atomic force microscopy. *Physical Review Letters* **123,** 066001 (2019).

110. Fatayer, S. *et al.* Controlled fragmentation of single molecules with atomic force microscopy by employing doubly charged states. *Physical Review Letters* **121,** 226101 (2018).

111. Fatayer, S. *et al.* Probing molecular excited states by atomic force microscopy. *Physical Review Letters* **126,** 176801 (2021).

112. Peng, J. *et al.* Atomically resolved single-molecule triplet quenching. *Science* **373,** 452–456 (2021).

113. Fatayer, S. *et al.* Reorganization energy upon charging a single molecule on an insulator measured by atomic force microscopy. *Nature Nanotechnology* **13,** 376–380 (2018).

114. Haken, H. & Wolf, H. C. *Molekülphysik und Quantenchemie: Einführung in die experimentellen und theoretischen Grundlagen* (Springer-Verlag, 2013).

115. Park, H. *et al.* Nanomechanical oscillations in a single-C_{60} transistor. *Nature* **407,** 57–60 (2000).

116. Marcus, R. A. Electron transfer reactions in chemistry: theory and experiment (Nobel lecture). *Angewandte Chemie International Edition in English* **32,** 1111–1121 (1993).

117. Siegert, B., Donarini, A. & Grifoni, M. Nonequilibrium spin crossover in copper phthalocyanine. *Physical Review B* **93,** 121406 (2016).

118. Frankerl, M. & Donarini, A. Spin-orbit interaction induces charge beatings in a lightwave-STM–single molecule junction. *Physical Review B* **103,** 085420 (2021).

119. Münnich, G. *Cross-Sectional Scanning Probe Microscopy on GaAs: Tip-Induced Band Bending, Buried Acceptors and Adsorbed Molecules* PhD thesis (University of Regensburg, 2014).

120. Pavliček, N. *Scanning Probe Methods Applied to Molecular Electronics* PhD thesis (University of Regensburg, 2013).

121. Besocke, K. An easily operable scanning tunneling microscope. *Surface Science* **181,** 145–153 (1987).

122. Giessibl, F. J. High-speed force sensor for force microscopy and profilometry utilizing a quartz tuning fork. *Applied Physics Letters* **73,** 3956–3958 (1998).

123. Giessibl, F. J. Atomic resolution on Si (111)-(7×7) by noncontact atomic force microscopy with a force sensor based on a quartz tuning fork. *Applied Physics Letters* **76,** 1470–1472 (2000).

124. Scheuerer, P. *Charging phenomena in single molecules and ordered molecular islands* PhD thesis (University of Regensburg, 2021).

125. Crommie, M. F., Lutz, C. P. & Eigler, D. M. Confinement of electrons to quantum corrals on a metal surface. *Science* **262,** 218–220 (1993).

126. Stilp, F. *et al.* Very weak bonds to artificial atoms formed by quantum corrals. *Science* **372,** 1196–1200 (2021).

127. Heinrich, A., Lutz, C., Gupta, J. & Eigler, D. Molecule cascades. *Science* **298,** 1381–1387 (2002).

128. Tierney, H. L. *et al.* Experimental demonstration of a single-molecule electric motor. *Nature Nanotechnology* **6,** 625–629 (2011).

129. Garcia-López, V. *et al.* Molecular machines open cell membranes. *Nature* **548,** 567–572 (2017).

130. Hla, S.-W., Bartels, L., Meyer, G. & Rieder, K.-H. Inducing All Steps of a Chemical Reaction with the Scanning Tunneling Microscope Tip: Towards Single Molecule Engineering. *Physical Review Letters* **85,** 2777–2780 (2000).

131. Pavliček, N. *et al.* Synthesis and characterization of triangulene. *Nature Nanotechnology* **12,** 308–311 (2017).

132. Garcia-Manyes, S. & Beedle, A. E. Steering chemical reactions with force. *Nature Reviews Chemistry* **1,** 1–16 (2017).

133. Ladenthin, J. N. *et al.* Force-induced tautomerization in a single molecule. *Nature Chemistry* **8,** 935–940 (2016).

134. Ternes, M., Lutz, C. P., Hirjibehedin, C. F., Giessibl, F. J. & Heinrich, A. J. The force needed to move an atom on a surface. *Science* **319,** 1066–1069 (2008).

135. Wu, S. & Ho, W. Two-photon-induced hot-electron transfer to a single molecule in a scanning tunneling microscope. *Physical Review B* **82,** 085444 (2010).

136. Lee, J., Perdue, S. M., Rodriguez Perez, A. & Apkarian, V. A. Vibronic motion with joint angstrom–femtosecond resolution observed through Fano progressions recorded within one molecule. *ACS Nano* **8,** 54–63 (2014).

137. Yampolsky, S. *et al.* Seeing a single molecule vibrate through time-resolved coherent anti-Stokes Raman scattering. *Nature Photonics* **8,** 650–656 (2014).

138. Li, S., Chen, S., Li, J., Wu, R. & Ho, W. Joint Space-Time Coherent Vibration Driven Conformational Transitions in a Single Molecule. *Physical Review Letters* **119,** 1–5 (2017).

139. Lee, J., Crampton, K. T., Tallarida, N. & Apkarian, V. A. Visualizing vibrational normal modes of a single molecule with atomically confined light. *Nature* **568,** 78–82 (2019).

140. Wörner, H. J., Bertrand, J. B., Kartashov, D. V., Corkum, P. B. & Villeneuve, D. M. Following a chemical reaction using high-harmonic interferometry. *Nature* **466,** 604–607 (2010).

141. Wolter, B. *et al.* Ultrafast electron diffraction imaging of bond breaking in di-ionized acetylene. *Science* **354,** 308–312 (2016).

142. Elsaesser, T. Introduction: ultrafast processes in chemistry. *Chemical Reviews* **117,** 10621–10622 (2017).

143. Prokhorenko, V. I. *et al.* Coherent control of retinal isomerization in bacteriorhodopsin. *Science* **313,** 1257–1261 (2006).

144. Böckmann, H. *et al.* Near-field spectral response of optically excited scanning tunneling microscope junctions probed by single-molecule action spectroscopy. *The Journal of Physical Chemistry Letters* **10,** 2068–2074 (2019).

145. Lin, X. & Nilius, N. Self-assembly of MgPc molecules on polar FeO thin films. *The Journal of Physical Chemistry C* **112,** 15325–15328 (2008).

146. Miwa, K., Imada, H., Kawahara, S. & Kim, Y. Effects of molecule-insulator interaction on geometric property of a single phthalocyanine molecule adsorbed on an ultrathin NaCl film. *Physical Review B* **93,** 165419 (2016).

147. Alemani, M. *et al.* Electric field-induced isomerization of azobenzene by STM. *Journal of the American Chemical Society* **128,** 14446–14447 (2006).

148. Zhang, Y. *et al.* Simultaneous and coordinated rotational switching of all molecular rotors in a network. *Nature Nanotechnology* **11,** 706–712 (2016).

149. Liljeroth, P., Repp, J. & Meyer, G. Current-induced hydrogen tautomerization and conductance switching of naphthalocyanine molecules. *Science* **317,** 1203–1206 (2007).

150. Stipe, B., Rezaei, M. & Ho, W. Coupling of vibrational excitation to the rotational motion of a single adsorbed molecule. *Physical Review Letters* **81,** 1263 (1998).

151. Qiu, X., Nazin, G. & Ho, W. Mechanisms of reversible conformational transitions in a single molecule. *Physical Review Letters* **93,** 196806 (2004).

152. Jahng, J. *et al.* Ultrafast pump-probe force microscopy with nanoscale resolution. *Applied Physics Letters* **106,** 083113 (2015).

153. Schumacher, Z., Spielhofer, A., Miyahara, Y. & Grutter, P. The limit of time resolution in frequency modulation atomic force microscopy by a pump-probe approach. *Applied Physics Letters* **110,** 053111 (2017).

154. Eichberger, M. *et al.* Snapshots of cooperative atomic motions in the optical suppression of charge density waves. *Nature* **468,** 799–802 (2010).

155. Scholes, G. D. *et al.* Using coherence to enhance function in chemical and biophysical systems. *Nature* **543,** 647–656 (2017).

156. Schliwa, M. & Woehlke, G. Molecular motors. *Nature* **422,** 759–765 (2003).

157. Erbas-Cakmak, S., Leigh, D. A., McTernan, C. T. & Nussbaumer, A. L. Artificial molecular machines. *Chemical Reviews* **115,** 10081–10206 (2015).

158. Dattler, D. *et al.* Design of collective motions from synthetic molecular switches, rotors, and motors. *Chemical Reviews* **120,** 310–433 (2019).

159. Alemani, M. *et al.* Recording the intramolecular deformation of a 4-legs molecule during its STM manipulation on a Cu (2 1 1) surface. *Chemical Physics Letters* **402,** 180–185 (2005).

160. Chiaravalloti, F. *et al.* A rack-and-pinion device at the molecular scale. *Nature Materials* **6,** 30–33 (2007).

161. Kühne, T. *et al.* STM induced manipulation of azulene-based molecules and nanostructures: the role of the dipole moment. *Nanoscale* **12,** 24471–24476 (2020).

162. Shirai, Y., Osgood, A. J., Zhao, Y., Kelly, K. F. & Tour, J. M. Directional control in thermally driven single-molecule nanocars. *Nano Letters* **5,** 2330–2334 (2005).

163. Shirai, Y. *et al.* Surface-rolling molecules. *Journal of the American Chemical Society* **128,** 4854–4864 (2006).

164. Baber, A. E., Tierney, H. L. & Sykes, E. C. H. A quantitative single-molecule study of thioether molecular rotors. *Acs Nano* **2,** 2385–2391 (2008).

165. Komeda, T., Kim, Y., Kawai, M., Persson, B. & Ueba, H. Lateral hopping of molecules induced by excitation of internal vibration mode. *Science* **295,** 2055–2058 (2002).

166. Saywell, A. *et al.* Light-induced translation of motorized molecules on a surface. *ACS Nano* **10,** 10945–10952 (2016).

167. Schaffert, J. *et al.* Imaging the dynamics of individually adsorbed molecules. *Nature Materials* **12,** 223 (2013).

168. Ossikovski, R., Nguyen, Q. & Picardi, G. Simple model for the polarization effects in tip-enhanced Raman spectroscopy. *Physical Review B* **75,** 045412 (2007).

169. Schröder, B. *et al.* Controlling photocurrent channels in scanning tunneling microscopy. *New Journal of Physics* **22,** 033047 (2020).

170. Nony, L., Bocquet, F., Para, F. & Loppacher, C. Frequency shift, damping, and tunneling current coupling with quartz tuning forks in noncontact atomic force microscopy. *Physical Review B* **94,** 115421 (2016).

171. Ooe, H. *et al.* Amplitude dependence of image quality in atomically-resolved bimodal atomic force microscopy. *Applied Physics Letters* **109,** 141603 (2016).

172. Garcia, R. & Herruzo, E. T. The emergence of multifrequency force microscopy. *Nature Nanotechnology* **7,** 217–226 (2012).

173. Kaiser, K., Lieske, L.-A., Repp, J. & Gross, L. Charge-state lifetimes of single molecules on ultrathin insulating films. *arXiv preprint arXiv:2211.01051* (2022).

174. Uhlmann, C. *Tieftemperatur-Rastertunnelmikroskopie an Phthalocyanin-Molekülen auf ultradünnen Isolatorfilmen: Ladungszustand, Jahn-Teller Effekt und ein molekularer Schalter* PhD thesis (University of Regensburg, 2013).

175. Mi, J. *et al.* Excited-state dynamics of magnesium phthalocyanine thin film. *Physics Letters A* **310,** 486–492 (2003).

176. Ran, G. *et al.* Femtosecond excited state dynamics of liquid deposited magnesium phthalocyanine thin films. *Chemical Physics Letters* **751,** 137501 (2020).

177. Zhang, L. *et al.* Electrically driven single-photon emission from an isolated single molecule. *Nature Communications* **8,** 1–7 (2017).

178. Sellies, L. *Imaging orbitals of excited molecules with photoexcitation scanning probe microscopy* Master Thesis (University of Regensburg, 2020).

179. Steurer, W. *et al.* Manipulation of the charge state of single Au atoms on insulating multilayer films. *Physical Review Letters* **114,** 036801 (2015).

180. Kocič, N. *et al.* Periodic charging of individual molecules coupled to the motion of an atomic force microscopy tip. *Nano Letters* **15,** 4406–4411 (2015).

181. Rai, V. *et al.* Boosting light emission from single hydrogen phthalocyanine molecules by charging. *Nano Letters* **20,** 7600–7605 (2020).

182. Chen, C., Chu, P., Bobisch, C., Mills, D. & Ho, W. Viewing the interior of a single molecule: vibronically resolved photon imaging at submolecular resolution. *Physical Review Letters* **105,** 217402 (2010).

183. Halasinski, T. M., Hudgins, D. M., Salama, F., Allamandola, L. J. & Bally, T. Electronic absorption spectra of neutral pentacene ($C_{22}H_{14}$) and its positive and negative ions in Ne, Ar, and Kr matrices. *The Journal of Physical Chemistry A* **104,** 7484–7491 (2000).

184. Heinecke, E., Hartmann, D., Müller, R. & Hese, A. Laser spectroscopy of free pentacene molecules (I): The rotational structure of the vibrationless $S_1 \leftarrow S_0$ transition. *The Journal of Chemical Physics* **109,** 906–911 (1998).

185. Zimmerman, P. M., Bell, F., Casanova, D. & Head-Gordon, M. Mechanism for singlet fission in pentacene and tetracene: From single exciton to two triplets. *Journal of the American Chemical Society* **133,** 19944–19952 (2011).

186. Zirzlmeier, J. *et al.* Singlet fission in pentacene dimers. *Proceedings of the National Academy of Sciences* **112,** 5325–5330 (2015).

187. Zimmerman, P. M., Zhang, Z. & Musgrave, C. B. Singlet fission in pentacene through multi-exciton quantum states. *Nature Chemistry* **2,** 648–652 (2010).

188. Romero, N. A. & Nicewicz, D. A. Organic photoredox catalysis. *Chemical Reviews* **116,** 10075–10166 (2016).

189. Spachtholz, R. *Towards mid-infrared Scanning Tunneling Microscopy: Design, build-up and troubleshooting* Bachelor Thesis (University of Regensburg, 2019).

190. Drexler, P. *Mid-infrared Scanning Tunneling Microscope: Scan head build-up and test measurements* Bachelor Thesis (University of Regensburg, 2019).

191. Ruckerbauer, V. *Design, optimization and construction of an annealing stage for a novel light-wave STM* Bachelor Thesis (University of Regensburg, 2021).

192. Hausfelder, H. *Instrument development for mid-infrared femtosecond scanning tunneling microscopy* Bachelor Thesis (University of Regensburg, 2022).

193. Vogt, N. *Design, Aufbau und Messung im Rahmen eines neuen Lichtwellen-Rastertunnelmikroskops* Bachelor Thesis (University of Regensburg, 2021).

194. Kimura, K. *et al.* Terahertz-field-driven scanning tunneling luminescence spectroscopy. *ACS Photonics* **8,** 982–987 (2021).

195. Wang, L., Xia, Y. & Ho, W. Atomic-scale quantum sensing based on the ultrafast coherence of an H_2 molecule in an STM cavity. *Science* **376,** 401–405 (2022).

196. Sindhu, P. *Fundamentals of Molecular Spectroscopy.* (New Age International, 2006).

197. Huber, K.-P. *Molecular spectra and molecular structure: IV. Constants of diatomic molecules* (Springer Science & Business Media, 2013).

198. Dabrowski, M., Dai, Y. & Petek, H. Ultrafast photoemission electron microscopy: imaging plasmons in space and time. *Chemical Reviews* **120,** 6247–6287 (2020).

199. Nicholson, C. W. *et al.* Beyond the molecular movie: Dynamics of bands and bonds during a photoinduced phase transition. *Science* **362,** 821–825 (2018).

200. Horstmann, J. G. *et al.* Coherent control of a surface structural phase transition. *Nature* **583,** 232–236 (2020).

201. Huber, R., Brodschelm, A., Tauser, F. & Leitenstorfer, A. Generation and field-resolved detection of femtosecond electromagnetic pulses tunable up to 41 THz. *Applied Physics Letters* **76,** 3191–3193 (2000).

202. Steinleitner, P. *et al.* Single-cycle infrared waveform control. *Nature Photonics,* 1–7 (2022).

203. Yoshioka, K. *et al.* Subcycle mid-infrared coherent transients at 4 MHz repetition rate applicable to light-wave-driven scanning tunneling microscopy. *Optics Letters* **44,** 5350–5353 (2019).

204. Arashida, Y. *et al.* Subcycle mid-infrared electric-field-driven scanning tunneling microscopy with a time resolution higher than 30 fs. *ACS Photonics* **9,** 3156–3164 (2022).

205. Sheng, S. *et al.* Low-temperature, ultrahigh-vacuum tip-enhanced Raman spectroscopy combined with molecular beam epitaxy for in situ two-dimensional materials' studies. *Review of Scientific Instruments* **89,** 053107 (2018).

206. Steidtner, J. & Pettinger, B. High-resolution microscope for tip-enhanced optical processes in ultrahigh vacuum. *Review of Scientific Instruments* **78,** 103104 (2007).

207. Zhang, Z., Sheng, S., Wang, R. & Sun, M. Tip-Enhanced Raman Spectroscopy. *Analytical Chemistry* **88,** 9328–9346 (2016).

208. Van Schrojenstein Lantman, E. M., Deckert-Gaudig, T., Mank, A. J., Deckert, V. & Weckhuysen, B. M. Catalytic processes monitored at the nanoscale with tip-enhanced Raman spectroscopy. *Nature Nanotechnology* **7,** 583–586 (2012).

209. Plankl, M. *et al.* Subcycle contact-free nanoscopy of ultrafast interlayer transport in atomically thin heterostructures. *Nature Photonics* **15,** 594–600 (2021).

210. Jiang, T., Kravtsov, V., Tokman, M., Belyanin, A. & Raschke, M. B. Ultrafast coherent nonlinear nanooptics and nanoimaging of graphene. *Nature Nanotechnology* **14,** 838–843 (2019).

211. Eisele, M. *et al.* Ultrafast multi-terahertz nano-spectroscopy with sub-cycle temporal resolution. *Nature Photonics* **8,** 841–845 (2014).

212. Dhillon, S. *et al.* The 2017 terahertz science and technology roadmap. *Journal of Physics D: Applied Physics* **50,** 043001 (2017).

213. Pan, S., Hudson, E. W. & Davis, J. ^{3}He refrigerator based very low temperature scanning tunneling microscope. *Review of Scientific Instruments* **70,** 1459–1463 (1999).

List of Figures

Abbreviations

AC-STM	Alternate-charging scanning tunneling microscopy
AFM	Atomic force microscopy/microscope
AM	Amplitude modulation
CPD	Contact potential difference
CuPc	Copper phthalocyanine
CW	Continuous wave
DC	Direct current
DFT	Density functional theory
DOS	Density of states
FM	Frequency modulation
HOMO	Highest occupied molecular orbital
KPFS	Kelvin Probe Force Spectroscopy
LCPD	Local contact potential difference
LDOS	Local density of states
LT	Low temperature
LUMO	Lowest unoccupied molecular orbital
MgPc	Magnesium phthalocyanine
MIR	Mid-infrared
ML	Monolayer
NPL	Nanosecond pulsed laser

OAPM	Off-axis parabolic mirror
PLL	Phase-locked loop
SNOM	Scanning near-field optical microscopy
SPM	Scanning probe microscopy/microscope
STL	Scanning tunneling luminescence
STM	Scanning tunneling microscopy/microscope
STS	Scanning tunneling spectroscopy
TERS	Tip-enhanced Raman spectroscopy
TMDC	Transition metal dichalcogenide
UHV	Ultra-high vacuum
ZC	Zero crossing

Acknowledgement

In the end, I want to thank all of the people who supported me throughout this thesis.

First and foremost I want to express my gratitude to Prof. Dr. Jascha Repp, who gave me the opportunity to be a part of his research group. I would like to specifically thank him for his patient supervision and for teaching me his unique views on the world of physics. I am also thankful for his motivating guidance and his patient advice during the past years.

Further, I want to give thanks to Prof. Dr. Andrea Donarini for co-refereeing this thesis.

I also want to thank everyone involved in the photoexcitation experiments, namely Dr. Laerte Patera for starting this project with me and Lisanne Sellies, Dr. Tzu-Chao Hung and Andreas Rank for continuing this exciting research with me. I had a great time with all of you in the lab and I am very grateful for your company and help throughout the last years.

I am also indebted to the THz-STM team, specifically Dominik Peller, Lukas Kastner, Carmen Roelke, Johannes Hayes, Alexander Neef and Prof. Dr. Rupert Huber. Thank you for introducing me to the world of ultrafast laser physics and for your tireless dedication in the lab. At this point I also want to appreciate the work of our collaborators in these projects, namely Nikolaj Moll, Franco Bonafé, Dominik Sidler, Michael Ruggenthaler and Angel Rubio.

Special thanks also to Christoph Rohrer for creating a pleasant atmosphere in the office and his technical support when building and repairing the instruments. I am for sure going to miss our time in the lab enjoying weird music.

Thanks also to my Bachelor students Alina Schüller, Pauline Drexler, Daniel Reitinger and Hugh Lohan who helped in various aspects during this PhD thesis. I also want to thank Raffael Spachtholz, Victoria Ruckerbauer and Helena Hausfelder for their contributions to the MIR-STM.

I also want to thank all of the current and former members of the Repp group, especially Philipp Scheuerer, Fabian Queck, Tobias Preis, Jinbo Peng, Sophia Sokolov, Lisanne Sellies, Raffael Spachtholz and Andreas Rank. Thanks for establishing a friendly working environment and sharing all of your knowledge (and the occasional after-work drink) with me.

Finally I want to express my deepest thanks to Lisa - thank you for supporting me through all of these years. I am intrigued which new adventures we will go on together in the future.